



**HAL**  
open science

# Advanced signal processing techniques for GPR by taking into account the interface roughness of a stratified medium

Meng Sun

► **To cite this version:**

Meng Sun. Advanced signal processing techniques for GPR by taking into account the interface roughness of a stratified medium. Engineering Sciences [physics]. UNIVERSITE DE NANTES, 2016. English. NNT: . tel-01379297

**HAL Id: tel-01379297**

**<https://hal.science/tel-01379297>**

Submitted on 11 Oct 2016

**HAL** is a multi-disciplinary open access archive for the deposit and dissemination of scientific research documents, whether they are published or not. The documents may come from teaching and research institutions in France or abroad, or from public or private research centers.

L'archive ouverte pluridisciplinaire **HAL**, est destinée au dépôt et à la diffusion de documents scientifiques de niveau recherche, publiés ou non, émanant des établissements d'enseignement et de recherche français ou étrangers, des laboratoires publics ou privés.

Public Domain

# Thèse de Doctorat

Meng SUN

*Mémoire présenté en vue de l'obtention du  
grade de Docteur de l'Université de Nantes  
Sous le sceau de l'Université Bretagne Loire*

École doctorale Sciences et Technologies de l'Information et Mathématiques (STIM ED-503)

*Discipline : Electronique  
Spécialité : Traitement du signal  
Unité de recherche : IETR UMR 6164*

Soutenue le 30 septembre 2016

## Advanced signal processing techniques for GPR by taking into account the interface roughness of a stratified medium

### JURY

Président : **M. Ali KHENCHAF**, Professeur, Université de Bretagne Occidentale, ENSTA Bretagne  
Rapporteur : **M. Salah BOURENNANE**, Professeur, Institut Fresnel, Ecole Centrale Marseille  
Rapporteur : **M. Pascal LARZABAL**, Professeur, IUT de Cachan, Université Paris Sud  
Directeur de Thèse : **M. Yide WANG**, Professeur, Polytech Nantes, Université de Nantes  
Co-encadrant : **M. Cédric LE BASTARD**, Docteur, Chargé de Recherche, CEREMA, Les Ponts de Cé  
Co-encadrant : **M. Nicolas PINEL**, Docteur, Ingénieur, Alyotech France, Saint-Herblain



# Acknowledgments

I would like to express my gratitude to all those who helped me during the writing of this thesis.

First of all, I would like to thank my supervisor Professor Yide Wang, co-supervisor Dr. Cédric Le Bastard and Dr. Nicolas Pinel, who have offered me valuable suggestions in my research work. Without their patient instruction, insightful criticism and expert guidance, the completion of this thesis would not have been possible.

I would like to thank Cyrille Fauchard for the experimental data.

I would like to thank my friends and colleagues for their help.

In addition, I would like to thank the China Scholarship Council for funding my research work.

I should like to express my gratitude to my parents for their continuous support and encouragement.

Finally, I would like to thank my girlfriend Pan Jingjing, for her love, support and accompany.



# Glossary

In this thesis, vectors and matrices are denoted by bold lower-case and bold upper-case symbols, respectively. Vectors are, by default, column vectors.

## Mathematical Notations

$a$ : Scalar

$\mathbf{a}$ : Vector

$\mathbf{A}$ : Matrix

$(\cdot)^*$ : Complex-conjugate operator

$(\cdot)^T$ : Transpose operator

$(\cdot)^H$ : Conjugate-transpose operator

$(\cdot)^+$ : Moore-Penrose inverse operator

$\mathbf{I}$ : Identity matrix

$E(\cdot)$ : Expectation operator

$\hat{\cdot}$ : Estimated parameter

$diag(\mathbf{a})$ : Diagonal matrix whose diagonal elements are those of vector  $\mathbf{a}$

$tr(\mathbf{A})$ : Trace of matrix  $\mathbf{A}$

$Det(\mathbf{A})$ : Determinant of matrix  $\mathbf{A}$

$B$ : Frequency band in Hz

$\Delta\tau$ : Time delay between two echoes

$\Delta f$ : Frequency step in Hz

## List of Abbreviation

NDT: Non-Destructive Testing

UTAS: Ultra Thin Asphalt Surfacing

GPR: Ground Penetrating Radar

PILE: Propagation Inside Layer Expansion

MoM: Method of Moment

TDE: Time Delay Estimation

DOA: Direction Of Arrival

MUSIC: MUltiple SIgnal Classification

ESPRIT: Estimation of Signal Parameters via Rotational Invariance Technique

FFT: Fast Fourier Transform

IFT: Inverse Fourier Transform

IFFT: Inverse Fast Fourier Transform

PM: Propagator Method

EVM: EigenValue Method

SSP: Spatial Smoothing Preprocessing

MSSP: Modified Spatial Smoothing Preprocessing

ISS: Improved Spatial Smoothing

RMP: Root MUSIC Polynomial

RRMSE: Relative Root Mean Square Error

SNR: Signal to Noise Ratio

UWB: Ultra Wide Band

EM: Electromagnetic

FDTD: Finite Difference Time Domain

FEA: Finite Element analysis

ETSA: Exponentially Tapered Slot Antenna

LMSE: Least Mean Squares Error

RMS: Root Mean Square

RMSE: Root Mean Square Error

PDF: Probability Density Function

MPM: Matrix Pencil Method

MLE: Maximum Likelihood Estimation

VNA: Vector Network Analyser



# Contents

<b>1</b>	<b>Introduction</b>	<b>13</b>
1.1	Non-destructive testing . . . . .	13
1.2	Probing media . . . . .	15
1.3	Issue and motivation . . . . .	16
1.4	Recent developments . . . . .	19
1.5	Conclusion . . . . .	21
<b>2</b>	<b>Time delay estimation</b>	<b>23</b>
2.1	Introduction . . . . .	23
2.2	Signal model for a non-dispersive medium . . . . .	24
2.3	Conventional methods . . . . .	26
2.3.1	Inverse Fourier Transform . . . . .	26
2.3.2	Cross-correlation method . . . . .	26
2.4	Sub-band averaging techniques . . . . .	29
2.4.1	Extension of spatial smoothing . . . . .	31
2.4.2	Noise power estimation . . . . .	32
2.5	Subspace methods . . . . .	34
2.5.1	Introduction . . . . .	34
2.5.2	MUSIC . . . . .	34
2.5.3	Root-MUSIC . . . . .	35
2.5.4	ESPRIT . . . . .	36
2.6	Performance evaluation . . . . .	39
2.6.1	Simulation parameters . . . . .	39
2.6.2	Simulation results . . . . .	40
2.7	Conclusion . . . . .	41
<b>3</b>	<b>Rough pavement scattering model</b>	<b>47</b>
3.1	Introduction . . . . .	47

3.2	PILE method . . . . .	48
3.2.1	Principle of PILE method . . . . .	49
3.2.2	Simulation parameters of PILE . . . . .	51
3.2.3	Simulation results . . . . .	53
3.3	Curve fitting . . . . .	58
3.3.1	Curve fitting results in narrow band . . . . .	58
3.3.2	Curve fitting results in middle band . . . . .	61
3.3.3	Curve fitting results in large band . . . . .	61
3.4	Conclusion . . . . .	64
<b>4</b>	<b>Parameter estimation for exponential model</b>	<b>65</b>
4.1	Signal model . . . . .	66
4.1.1	Signal model in the whole band . . . . .	66
4.1.2	Spatial smoothing preprocessing technique . . . . .	68
4.2	Subspace methods . . . . .	70
4.2.1	Modified two-dimensional MUSIC . . . . .	70
4.2.2	Modified root-MUSIC . . . . .	70
4.2.3	Matrix pencil method . . . . .	72
4.2.4	Time Delays and Roughness Parameters with ESPRIT . . . . .	75
4.3	Permittivity estimation . . . . .	78
4.4	Performance evaluation . . . . .	78
4.4.1	Simulation parameters . . . . .	78
4.4.2	Simulation results . . . . .	80
4.5	Conclusion . . . . .	89
<b>5</b>	<b>Parameter estimation for Gaussian and mixed models</b>	<b>91</b>
5.1	Signal model . . . . .	92
5.2	Multi-dimensional search methods . . . . .	93
5.2.1	Maximum likelihood estimation . . . . .	93
5.2.2	Generalized MUSIC algorithm . . . . .	94
5.2.3	Simulation examples . . . . .	96
5.3	Modified MUSIC algorithm . . . . .	97
5.3.1	Interpolation spatial smoothing technique . . . . .	97
5.3.2	Minimum eigenvalue search by modified MUSIC . . . . .	99
5.3.3	Interface roughness estimation . . . . .	102
5.4	Performance evaluation . . . . .	103

<i>CONTENTS</i>	11
5.4.1 Simulation parameters . . . . .	103
5.4.2 Simulation results . . . . .	104
5.5 Conclusion . . . . .	113
<b>6 Experiments</b>	<b>115</b>
6.1 Introduction . . . . .	115
6.1.1 Experimental device . . . . .	115
6.1.2 Studied medium . . . . .	116
6.1.3 Data set . . . . .	117
6.2 Experimental results . . . . .	118
6.2.1 Pre-processing of the Data . . . . .	118
6.2.2 Time delay estimation . . . . .	121
6.2.3 Interface roughness estimation . . . . .	121
6.3 Conclusion . . . . .	122
<b>7 Conclusion and perspectives</b>	<b>127</b>
7.1 Conclusion . . . . .	127
7.2 Perspectives . . . . .	129
<b>A Curve fitting results of case <i>a</i> and case <i>b</i> in chapter 3</b>	<b>131</b>
<b>B Proof for the Modified MUSIC in chapter 5</b>	<b>137</b>
<b>C Research and Published Papers</b>	<b>141</b>
<b>D Résumé étendu (French extended abstract)</b>	<b>143</b>



# Introduction

Civil engineering is a field of engineering dealing with the design, construction and maintenance of roads, bridges, buildings, dams, canals, etc. To test or evaluate the properties of these structures, two testing methods are available. The first method is the destructive testing method, which destroys the probed medium. It is favourable when the number of drilling is small and can be used for the thickness estimation in civil engineering. Nevertheless, to measure the long distance, the destructive testing cannot be feasible. Thus, under this condition, Non-Destructive Testing (NDT) is preferred to inspect, test or evaluate materials, components or assemblies without destroying the products.

This chapter is organised as follows: in section 1, we present some NDT methods and how Ground Penetrating Radar (GPR) works as a NDT method in the field of civil engineering. Section 2 describes the probing media: the pavement layers. Section 3 presents the issue and motivation of this thesis. Recent developments in signal processing methods on GPR for pavement survey are discussed in section 4. And finally, conclusions are drawn.

## 1.1 Non-destructive testing

NDT is a common way to evaluate the properties of a material without causing any damage. Compared to destructive testing, NDT is a highly valuable technique that

can save both time and money in product evaluation, troubleshooting or some research work. Usual NDT methods include ultrasonic, magnetic-particle, radiographic, eddy current testing, remote visual inspection and liquid penetration, which are often used in the field of civil engineering, electrical engineering, aeronautical engineering, forensic engineering, mechanical engineering, petroleum engineering, systems engineering, medicine and so on.

In the field of civil engineering, for example, ultrasonic testing (UT) is a NDT method which makes use of the principles of mechanical vibration and the propagation of ultrasonic waves inside the tested materials [1]. In most cases, UT uses very short ultrasonic pulse-waves with centre frequencies between 0.1 and 15 MHz, or in some situations up to 50 MHz, and transmits them into materials to detect internal flaws or to characterize the materials. UT is particularly used for estimating the thickness of materials or monitor pipework corrosion. Generally, UT is applied on detecting metallic materials. Although it can also be used on concrete, wood or soil, the resolution is decreased dramatically. Radiographic Testing (RT) is also used as NDT method. It is able to detect hidden flaws in materials by using short wavelength electromagnetic waves. It is able to penetrate in various materials. X-rays may also be used for sensing various materials, as they can easily penetrate through metal. Nevertheless, X-rays can be absorbed by plastics, soil and water.

In addition, GPR is one another NDT method which has numerous applications in various fields. It can be used in the Earth sciences, environmental re-mediation, archaeology and so on. This NDT method uses electromagnetic radiation in the microwave band (UHF/VHF frequencies) of the radio spectrum. GPR uses high-frequency radio waves to image the subsurface. It detects the reflected signals from subsurface structures or objects. GPR can be used in a large variety of media, including rocks, soil, ice, fresh water, pavements and structures. It can detect objects, changes in materials as well as voids and cracks.

For this PhD thesis, this work is focused on road pavement survey by using the NDT GPR method in order to make a diagnostic imaging of the pavement structure. Two kinds of GPR can be used: impulse GPR and step-frequency GPR. Impulse GPR acquires pulse response in time domain directly. It is one of the simplest method to generate an impulse waveform and low-cost. However, it has undesirable ringing, inefficient use of transmit power and limited resolution by pulse width. For a step-frequency GPR, the transmitting frequency is stepped in linear increment over a fixed bandwidth, from a start frequency to a stop frequency. The received signal is mixed and sampled at each discrete frequency step. It can control transmission frequencies,

with efficient use of power and sampling of wideband signals.

## 1.2 Probing media

The French national road network is approximately a million miles [2]. Regular maintenance of the road helps maintaining the safety in a sufficient level for users. This maintenance is carried out by controlling the existing coatings (measure the thickness, detect and monitor the cracks [3]). Furthermore, NDT of the thickness allows with verifying the quality of implementation of new pavement [2]. As French traffic is continuously increasing, the maintenance of the road network requires regularly re-assessing the design of road structures. In the receipt of a construction, the goal is to estimate the thicknesses and to verify if the thicknesses are consistent with the requirements of the specification. To make the maintenance of the road network effectively, we need to achieve high-performance measures.

In this study, a GPR (impulse GPR in Fig. 1.1 and step frequency GPR Fig. 1.2) is used to estimate the thicknesses of pavements. However, in practice, the destructive sampling by coring is still the most used way to check the thickness of pavement layers [4]. The coring associated with radar measurements allows to calibrate radar measurements (explicitly determine the speed of wave propagation in the layer) from a representative sample of a homogeneous medium. In this case, the destructive surveys and non-destructive surveys are complementary. The pavement appears as a multilayer pavement structure. The pavement is schematically made up of a surface layer, a base course layer, a sub-base layer, a compacted sub-grade and a natural sub-grade (see Fig 1.3). The layers contain a surface layer to contact vehicles tires, and a bonding layer that facilitates the transfer of superficial loads. The pavement over-layer consists of aggregates, embedded in a matrix of bitumen or bituminous binder.

The pavement surface layer typically ranges within [1; 10] cm and is directly affected by traffic and climate. The average thickness is about 2 cm for Ultra Thin Asphalt Surfacing (UTAS). This layer contributes to the sustainability of the pavement structure. The base course layer and the sub-base layer ensure the dissemination efforts and are often composed of treated gravel and/or non-treated with hydraulic binders (cement) or bituminous. The compacted sub-grade layer is a layer of material intended to improve and homogenize the bearing capacity of the sub-grade. Its thickness may be significant if the bearing capacity is weak.

In 1980's, with the development of modified bitumen with polymers and the use of additives, new types of asphalt concrete appeared, bringing better performance in terms

of quality and durability. These new asphalt concretes are used for the construction of new pavements and maintenance works. This technological innovation has reduced the thickness of the surface and interface layers.



Figure 1.1: Example of an impulse GPR (SIR-3000) [5]

### 1.3 Issue and motivation

The study of electromagnetic scattering by layered surfaces has a large number of applications, like in pavement survey. It can be used to measure the thickness, detect and evaluate damaged zones (interface debonding of pavements and of seal coats of highway structures). The centimetre-scale wavelengths are often used for the specific application of pavement survey [6, 7, 8, 9, 10, 11] and more especially for measuring the thickness of different layers, which permits rapid data collection for pavement surveys. In road pavement survey, particularly for measuring the thickness of different layers, the road layers are assumed to be horizontally stratified [3, 10, 12, 13, 14], the vertical structure of the pavement can be deduced from radar profiles by means of time delay and amplitude estimations. Echo detection provides the time-delay estimation associated with each interface, while amplitude estimation is used to retrieve the wave speed within each layer.



Figure 1.2: Example of a step frequency GPR [5]

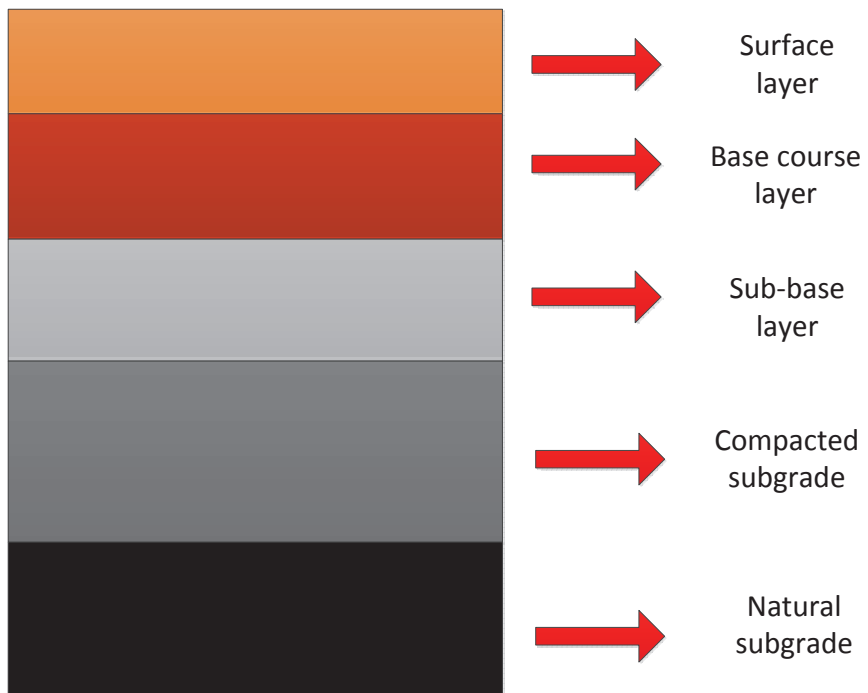


Figure 1.3: Pavement structure

Nowadays, the thickness of the new pavement layer of the road network is less than 5 cm, which is too small to be measured by conventional radar techniques. Indeed, the time resolution depends on the frequency bandwidth. For a conventional GPR (central frequency is 2 GHz), the minimum thickness which can be measured is around 5 cm. Then, there exists a need for improving the time resolution of NDT techniques. To solve this problem, there are 2 solutions. The first solution is to increase the frequency range of GPR: when the layer thickness is smaller than 5 cm, the frequency band of GPR should be larger than 7 GHz. The second solution is to use signal processing methods and in particular high resolution methods to improve the GPR time resolution.

For conventional band-limited pulse radar, high-resolution processing is required whenever layer thickness of the pavement is less than approximately 5 cm [12]. In this thesis, the work is focused on the second solution: to improve the time resolution of GPR by signal processing methods.

At usual GPR wavelengths (decimetre range in the air), the interface roughness may be neglected. Within the scope of using the ultra-wide band capability of the step-frequency radar technology (and in particular, the upper frequency range, which may be up to 8 – 10 GHz), the influence of the interface roughness has to be addressed [15]. For layer thickness measurement, it has been shown that the influence of the interlayer roughness (the roughness of embedded interfaces) prevails on the surface roughness. In the civil engineering and GPR literature, generally, signal processing does not take the roughness into account. When the interface roughness is taken into account, it is often used to analyse the errors coming from roughness [15, 16]. In addition, the roughness of only one interface is generally analysed [17, 18]. In the field of SAR, some research has been carried out to estimate the surface roughness, especially in [19, 20, 21]. In our study, we also focus on the estimation of interface roughness. We take the surface and the embedded interfaces roughness into account in the signal model. We propose some new signal processing methods to jointly estimate the time delay and a new parameter: the roughness parameter (roughness of the surface and the embedded interfaces). This new parameter measured by GPR is very important for road safety, especially for estimating pavement skid resistance. Furthermore, this new parameter is also expected to be used in analysing the inside of the pavement, especially to detect the cracks or debonding by highlighting the disaggregation of the interface materials. Thus, new signal processing methods are proposed to estimate different parameters of the stratified medium (interface roughness, as well as thickness of layers). These estimations will make it possible to detect and evaluate damaged zones (interface debonding of pavements and seal coats of bridges).

## 1.4 Recent developments

The methods that estimate the thickness of pavement layers can be divided into 2 categories:

- Conventional methods, such as conventional FFT-based methods. For the thickness estimation, the backscattered echoes should be non-overlapped. It means that  $B\Delta\tau > 1$ , where  $B$  is the used radar frequency band and  $\Delta\tau$  is the time delay between two backscattered echoes.
- High resolution methods (MUSIC, ESPRIT, etc) which allow estimating thin pavement thickness in civil engineering when the backscattered echoes are overlapped,  $B\Delta\tau \leq 1$ .

Processing time resolution of GPR is defined for a given frequency band ( $B$ ) as the minimal time shift ( $\Delta\tau$ ) between two echoes that the processing is able to distinguish [12]. Fig. 1.4 gives an example of GPR time resolution with different  $B\Delta\tau$  products. In Chapter 2, the differences between conventional methods and high resolution methods are presented.

For thickness estimation, in the past decade, some authors have already proposed to use signal processing techniques (high resolution methods) with GPR to estimate the pavement thickness and especially for small pavement thicknesses [12]. High resolution methods have been originally proposed in the Direction of Arrival (DOA) finding. Recently, they have been successfully developed to the spectral analysis and for the Time Delay Estimation (TDE). Moghaddar et al. [22] proposed a modified MUSIC algorithm to estimate the time delays and frequency response of electromagnetic scattering where the frequency-dependent amplitudes are taken into account in the signal model. It allows jointly estimating the time delays and the frequency-dependent amplitudes. Qu et al. [23] proposed to use ESPRIT with an improved spatial smoothing technique for TDE by GPR.

With the development of GPR, especially the ultra wideband GPR, the bandwidths of radar have been extended up to 8 – 10 GHz. As a consequence, the influence of interface roughness should not be neglected any more. Indeed, the influence of interface roughness causes a continuous frequency decay of the amplitude of echoes. The interface roughness has been studied in recent papers [17, 18]. In [18], they combine a full-waveform GPR model with a roughness model to retrieve surface soil moisture through signal inversion. In [17], they concentrate on the detection and identification of a buried target under a rough air-ground interface. Nevertheless, only a single rough interface is considered in these two cases. In [15, 24], authors consider more sophis-

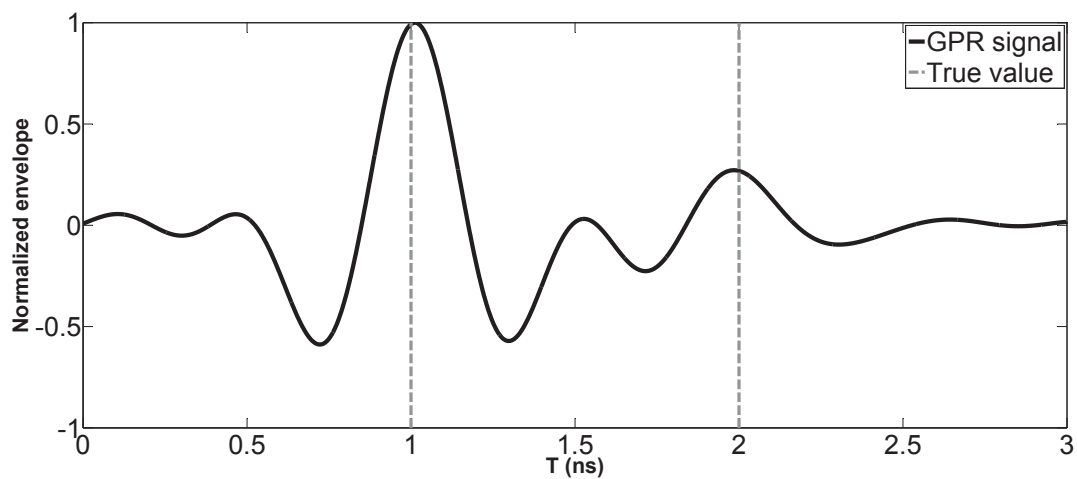
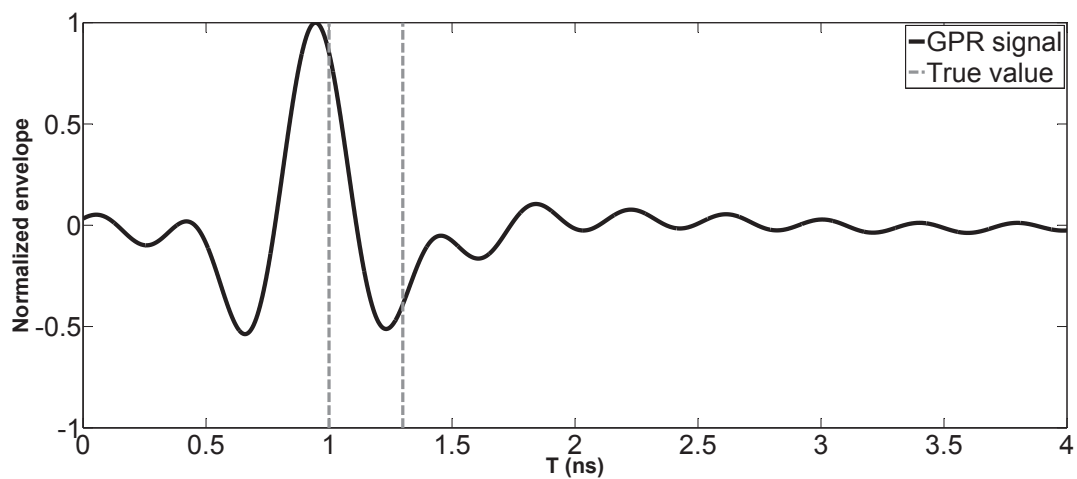
(a) Product  $B\Delta\tau > 1$ (b) Product  $B\Delta\tau \leq 1$ 

Figure 1.4: GPR signals for overlapped  $B\Delta\tau = 0.6$  and non-overlapped  $B\Delta\tau = 3$  case at  $\text{SNR}=20$  dB,  $B = 2$  GHz

licated electromagnetic modellings for the case of more than one rough interface. In [15], PILE (Propagation Inside Layer Expansion) based on Method of Moment (MoM) is used to simulate the radar backscattered signal at nadir from a rough pavement made up of two rough interfaces separating homogeneous media. In [24], a generalized PILE to study a medium composed of multiple random rough interfaces is presented. In this thesis, we propose to make a quantitative analysis by using PILE to study the influence of interface roughness on the electromagnetic scattering (first-two rough interfaces). Then, we propose to extend high resolution methods (subspace methods) for new signal models, which take the interface roughness into account.

## 1.5 Conclusion

The application of this thesis is to measure the thickness of pavements as well as interface roughness, particularly for the first two layers of the pavement. In the past decade, a large number of new signal processing methods have been proposed for layer thickness estimation. But these methods do not take into account the interface roughness. In this thesis, we propose to extend high resolution methods (subspace methods) for jointly estimating thickness and interface roughness. For UTAS whose layer thickness varies from 1 to 3 cm, the conventional GPR cannot measure the thickness of these layers. The objective of this study is to improve the time resolution of radar systems in order to measure the pavement material made up of thin layers with thickness less than 3 cm. In addition, the interface roughness is addressed. The influence of interface roughness causes a continuous decay of the amplitude of echoes. The observed frequency behaviours of the echoes introduce some shape distortion of the radar waveform. In narrow frequency bands (less than 2 GHz), these frequency behaviours can be modelled by an exponential function. In large frequency bands, these frequency behaviours approach a Gaussian or a mixed function. In this application, the proposed signal processing methods are used to estimate the time delays of backscattered echoes from each interface of the layered medium as well as the interface roughness.

Chapter 2 presents the classical signal processing methods for TDE without taking into account the interface roughness (medium composed of smooth interface). Both conventional methods (with  $B\Delta\tau > 1$ ) and high resolution methods (with  $B\Delta\tau \leq 1$ ) are presented. Moreover, some improvements of adaptive spatial smoothing techniques for high resolution methods are proposed to decorrelate the correlation between the backscattered echoes.

Chapter 3 presents the influence of interface roughness on the backscattered echoes

for various frequency bands (narrow band and wide band) by using the PILE method. Because of the interface roughness, the frequency variations of the magnitude of the first two backscattered echoes are discussed. The frequency behaviour of the echoes is modelled by curve fittings.

Chapter 4 presents the proposed high resolution methods (subspace methods), which are extended to jointly estimate the time delays of backscattered echoes and roughness parameters of pavements for a narrowband frequency GPR.

Chapter 5 presents both multi-dimension search methods (MLE and generalized MUSIC) and a one-dimension search method (the modified MUSIC) for the time delays and interface roughness estimation by using wideband frequency GPR.

Chapter 6 validates the proposed algorithms on experimental data from a step-frequency GPR.

Finally, the dissertation is concluded by a summary of main contributions and suggestions for future work.

## Time delay estimation

### 2.1 Introduction

Time delay estimation has been an issue of great research interest for many years. It has a great number of applications in many fields (radar, sonar, geophysics, medical imaging, communications and so on). This chapter provides classical signal processing methods for layer thickness estimation by GPR based on TDE. For a dispersive medium, the layer thickness is dependent on the time delays, the permittivity and the dispersive parameter (such as Q factor [25]). For a non-dispersive medium (a low-loss or lossless medium), the layer thickness only depends on the time delays and permittivity. Thus, time delays are important parameters for the quantitative interpretation of GPR data [10] in the field of civil engineering. For horizontally stratified media, like the roadways [6] or walls [26], the vertical structure (the layer thickness) of the media can be deduced from radar profiles by means of echo detection and amplitude estimation. Echo detection provides the time delays associated with each interface, whereas amplitude estimation is used to retrieve the wave speed within each layer [6]. It must be highlighted that when the echoes are overlapped, high resolution methods should be used.

TDE is usually performed by using conventional methods, such as conventional FFT-based methods (inverse FFT or cross-correlation methods). However, this kind of method has a time resolution which depends on the bandwidth of GPR. High resolution

methods are required for TDE when the echoes are overlapped. To estimate the thin pavement thickness in civil engineering, the case of small pavement thicknesses was studied in recent papers [12]. The main difficulty with data processing lies in the detection of close backscattered echoes. Some particular pavement materials are made up of thin layers (thicknesses  $< 3$  cm), they require the use of the high resolution methods for thickness estimation as conventional methods are limited to distinguish closely backscattered echoes. In practice, backscattered echoes are correlated. In order to apply high resolution methods, sub-band averaging techniques should be applied before using the high resolution methods.

This chapter is organised as follows: section 2 presents the radar data model. Conventional methods and high resolution methods are introduced in section 3 and section 4, respectively. In section 5, we present preprocessing sub-band averaging techniques with either the propagator method (PM) [27] or the eigenvalue method (EVM) [28]. The preprocessing methods are used to mitigate the influence of the correlation between the backscattered echoes. Simulation results and a discussion on the performance of the proposed algorithms are provided in section 6. Finally, conclusions are drawn in section 7.

## 2.2 Signal model for a non-dispersive medium

In the roadway survey, we focus on the first two or three top layers, which are low-loss media. For pavement materials, the conductivity typically ranges within the interval  $[10^{-3}; 10^{-2}]$  S/m, according to the data provided in [4]. Thus, the media can be considered as a low-loss media. In addition, for the flat surface case, according to the work in [29], if the medium is slightly lossy, the dispersivity of the medium can be neglected. As a consequence, the echoes are simply time-shifted and attenuated copies of the transmitted signal, as mentioned in [6, 10, 13, 30]. Thus, for a horizontally stratified lossless medium, the received signal model can be written in the time domain as [12, 23, 31, 32]:

$$r(t) = \sum_{k=1}^d s_k e(t - t_k) + n(t) \quad (2.1)$$

For applying spectral analysis techniques to TDE, the received signal is usually formulated in the frequency domain. By using Fourier transform, the received signal model

can be expressed as:

$$r(f_i) = e(f_i) \sum_{k=1}^d s_k \exp(-j2\pi f_i t_k) + n(f_i) \quad (2.2)$$

where  $d$  is the number of backscattered echoes,  $e(t)$  and  $e(f_i)$  are the radar pulse in the time and frequency domains, respectively;  $s_k$  represents the reflection coefficient of the  $k$ th scattered echo,  $n(f_i)$  is an additive white Gaussian noise, with zero mean and variance  $\sigma^2$ ; the frequency  $f_i = f_1 + (i-1)\Delta f$ , with  $i = 1, 2 \dots N$ ,  $N$  the number of used frequencies,  $f_1$  the lowest frequency of the studied frequency band and  $\Delta f$  the frequency step. Eq. (2.2) can be written in the vector form as follows:

$$\mathbf{r} = \mathbf{\Lambda} \mathbf{A} \mathbf{s} + \mathbf{n} \quad (2.3)$$

with the following notational definitions:

1.  $\mathbf{r} = [r(f_1) \ r(f_2) \ \dots \ r(f_N)]^T$  is the  $(N \times 1)$  received signal vector, called observation vector, which may represent either the Fourier transform of the measured GPR signal or the measurements by a step-frequency radar; the superscript  $T$  denotes the transpose operation;
2.  $\mathbf{\Lambda} = \text{diag}(e(f_1), e(f_2), \dots, e(f_N))$  is a  $(N \times N)$  diagonal matrix, whose diagonal elements are the Fourier transform of the radar pulse  $e(t)$ ;
3.  $\mathbf{A} = [\mathbf{a}(t_1) \ \mathbf{a}(t_2) \ \dots \ \mathbf{a}(t_d)]$  is the  $(N \times d)$  mode matrix;
4.  $\mathbf{a}(t_k) = [e^{-2j\pi f_1 t_k} \ e^{-2j\pi f_2 t_k} \ \dots \ e^{-2j\pi f_N t_k}]^T$  is the mode vector;
5.  $\mathbf{s} = [s_1 \ s_2 \ \dots \ s_d]^T$  is the  $(d \times 1)$  vector of echo amplitudes;
6.  $\mathbf{n} = [n(f_1) \ n(f_2) \ \dots \ n(f_N)]^T$  is the  $(N \times 1)$  noise vector.

According to signal model (2.3) and assuming the noise to be independent of the echoes, the covariance matrix  $\mathbf{Y}$  of  $\mathbf{r}$  can be written as:

$$\begin{aligned} \mathbf{Y} &= E(\mathbf{r}\mathbf{r}^H) = \mathbf{\Lambda} \mathbf{A} E(\mathbf{s}\mathbf{s}^H) \mathbf{A}^H \mathbf{\Lambda}^H + E(\mathbf{n}\mathbf{n}^H) \\ &= \mathbf{\Lambda} \mathbf{A} \mathbf{S} \mathbf{A}^H \mathbf{\Lambda}^H + \sigma^2 \mathbf{I} \end{aligned} \quad (2.4)$$

where  $E(\cdot)$  denotes the ensemble average,  $\mathbf{S}$  is the  $(d \times d)$  dimensional covariance matrix of vector  $\mathbf{s}$  and  $\mathbf{I}$  is the identity matrix.

## 2.3 Conventional methods

In this section, we present two conventional methods. Firstly, the Inverse Fourier Transform (IFT) is used for step frequency GPR (the IFT converts a signal from its frequency domain to a representation in the time domain) and the cross-correlation method is applied for impulsion GPR (it works directly in the time domain).

### 2.3.1 Inverse Fourier Transform

By using IFT, the received signal in Eq. (2.2) can be transformed into the time domain as:

$$r(t) = \int_{-\infty}^{+\infty} r(f) \exp(j2\pi ft) df \quad (2.5)$$

The time delays of echoes can be determined by searching the peaks of  $r(t)$ . The main advantage of this method is low computational cost, it can be efficiently implemented with IFFT algorithm. However, the IFT method cannot resolve closely spaced time delays because of its resolution capability. In addition, IFT suffers from side-lobe leakage which can cause misinterpretation of the time delays. It introduces a bias in the TDE (called short-range leakage) [14]. It should be noted that tapering windows can sufficiently reduce the side-lobe leakage and that the zero padding is able to mitigate the short-range effect, but may increase the computational complexity.

As shown in Fig. 2.1, two examples with different  $B\Delta\tau$  products are considered, with  $B$  the frequency bandwidth and  $\Delta\tau$  the differential time delay. In the first case,  $B\Delta\tau > 1$ , which means that the two echoes are non-overlapped: the time delays are well estimated by searching the peaks of the signal envelope. In the second case,  $B\Delta\tau \leq 1$ , the two echoes are overlapped: only one peak is visible and the time delays are unable to be estimated by IFT method. As expected, IFT method cannot distinguish the closely spaced time delays unless the  $B\Delta\tau$  product is greater than 1.

### 2.3.2 Cross-correlation method

The cross-correlation method is particularly suitable for processing of the impulse GPR. The used observation model corresponds to the time model, defined by Eq. (2.1), the cross-correlation measures the similarity between the received signal  $r(t)$  and the transmitted signal  $e(t)$  as follows:

$$\Gamma(\tau) = \int_{-\infty}^{+\infty} r(t)e^*(t - \tau)dt \quad (2.6)$$

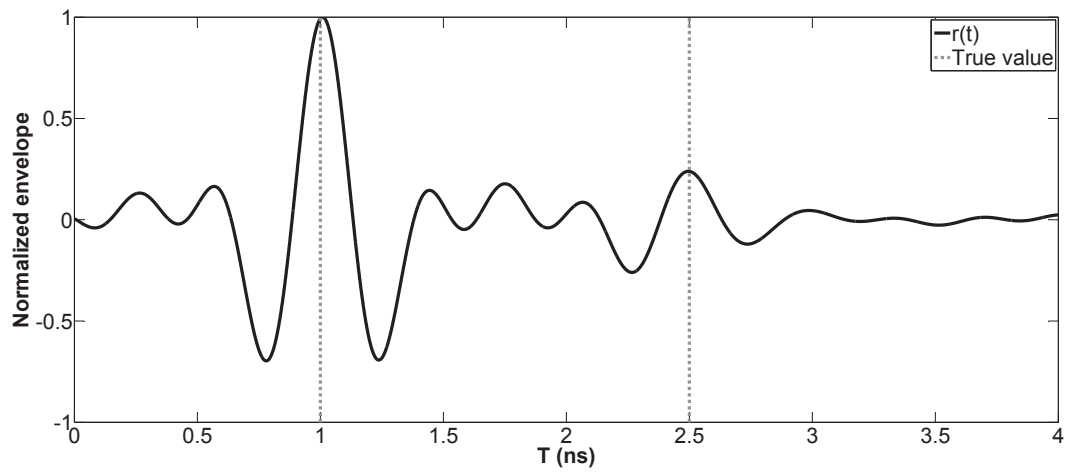
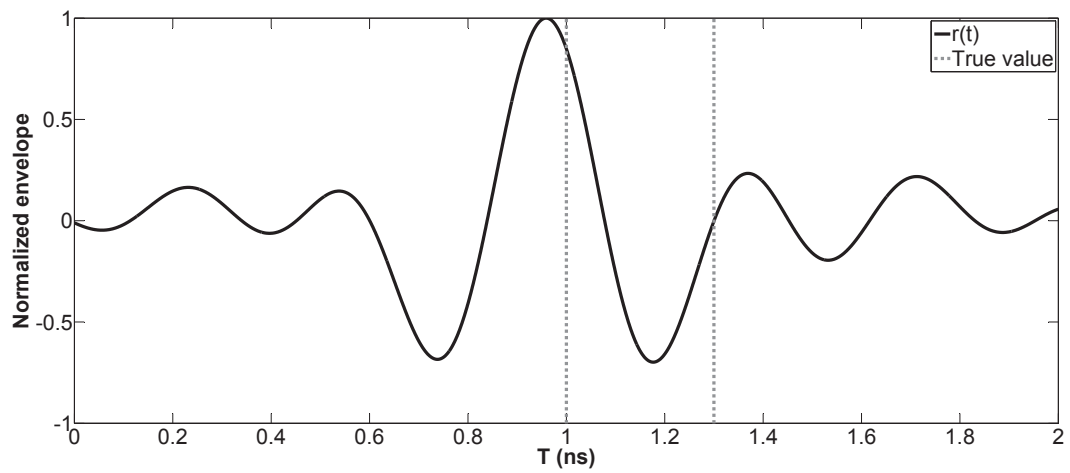
(a) Non-overlapped case  $B\Delta\tau > 1$ (b) Overlapped case  $B\Delta\tau \leq 1$ 

Figure 2.1: TDE by IFT for non-overlapped echoes ( $B\Delta\tau = 3$ ) and overlapped echoes ( $B\Delta\tau = 0.6$ ), SNR=20 dB and  $B = 2$  GHz

If the signals are of similar forms,  $\Gamma(\tau)$  is maximum for the value of the time delay. The cross-correlation result is equivalent the matched filter adapted to  $e(t)$ . The time delays can be estimated from the peak of  $\Gamma(\tau)$ . Like the IFT, the time resolution of the cross-correlation method cannot handle closely spaced time delays. Fig. 2.2

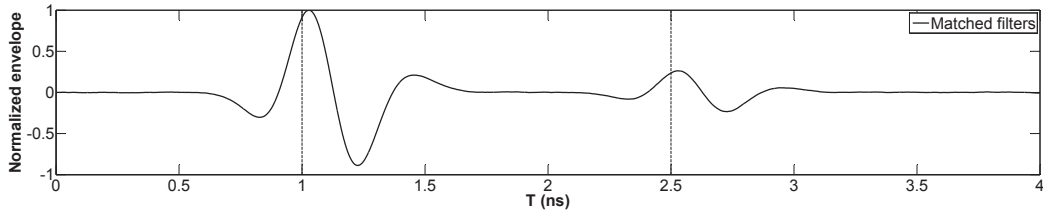
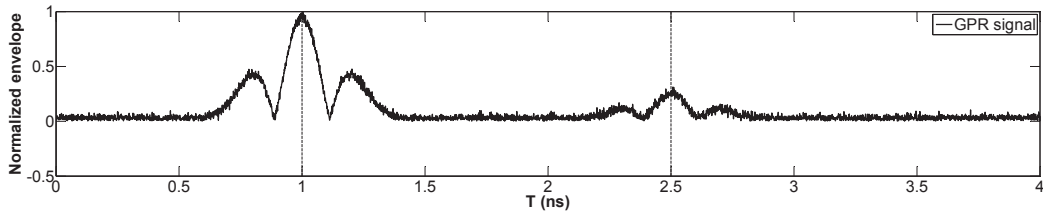
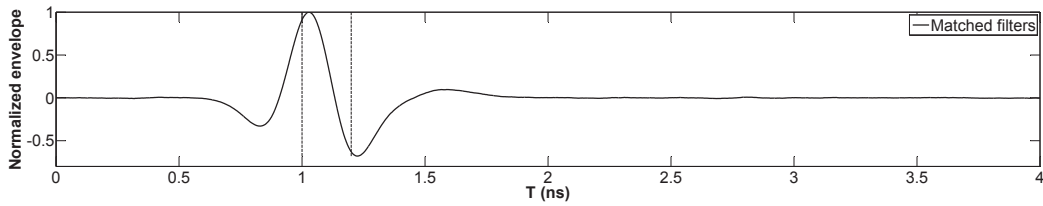
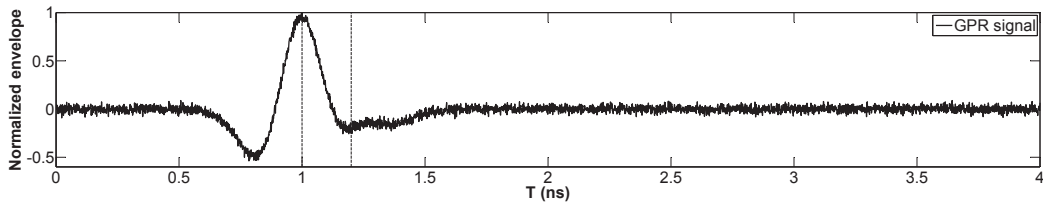
(a) Non-overlapped case  $\Delta\tau = 1.5$  ns(b) Overlapped case  $\Delta\tau = 0.2$  ns

Figure 2.2: TDE by cross-correlation method for non-overlapped and overlapped cases, SNR=20 dB and  $B = 2$  GHz

presents the results for both overlapped and non-overlapped echoes. Compared to the non-overlapped case which has two clear distinct peaks for the two time delays, the overlapped case causes two merged peaks due to the limited resolution of the method.

## 2.4 Sub-band averaging techniques

Before we present high resolution algorithms, sub-band averaging techniques are introduced. Indeed, in practice, received GPR signals are generally coherent. The correlation between echoes impacts the subspace-based high resolution methods and may be strong enough to degrade their performance. In this situation, the covariance matrix has to be processed with sub-band averaging techniques which allow to obtain a new covariance matrix with restored rank. We present the well-known spatial smoothing preprocessing (SSP) and modified spatial smoothing preprocessing (MSSP) techniques [32]. Two improved spatial smoothing techniques called here ISSA [23] and ISSB [33] are also presented in this section.

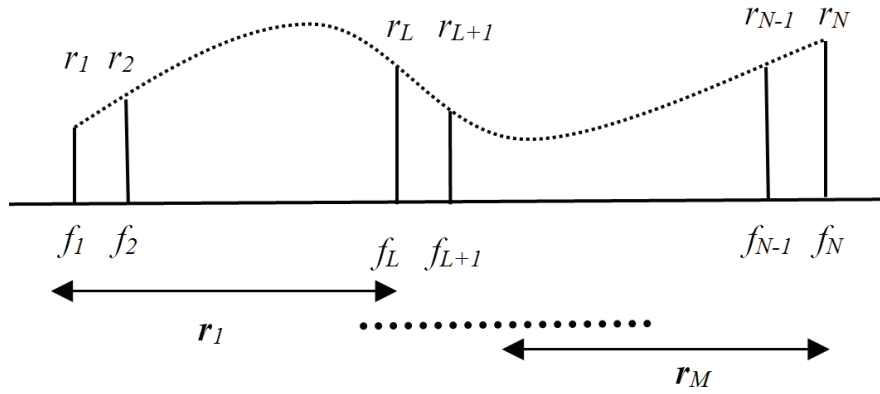


Figure 2.3: Set of the overlapping frequency sub-bands for the averaging techniques

To apply the sub-band averaging techniques, the influence of radar pulse must be eliminated from the radar signal. Thus, in the following, the data are divided by the pulse, then the new observation vector  $\mathbf{r}'$  can be written as  $\mathbf{r}' = \Lambda^{-1}\mathbf{r} = \mathbf{A}\mathbf{s} + \Lambda^{-1}\mathbf{n} = \mathbf{A}\mathbf{s} + \mathbf{b}$ , with  $\mathbf{b}$  the new noise vector after the data are divided by the pulse. The new covariance matrix  $\mathbf{R}_0$  can be written as:

$$\mathbf{R}_0 = E(\mathbf{r}'\mathbf{r}'^H) = \Lambda^{-1}\mathbf{Y}\Lambda^{-H} = \mathbf{A}\mathbf{S}\mathbf{A}^H + \sigma^2\mathbf{\Sigma} \quad (2.7)$$

with

$$\mathbf{\Sigma} = \Lambda^{-1}\Lambda^{-H} = \text{diag}\left(\frac{1}{|e(f_1)|^2}, \frac{1}{|e(f_2)|^2}, \dots, \frac{1}{|e(f_N)|^2}\right) \quad (2.8)$$

As shown in Fig. 2.3,  $N$  frequencies and  $M$  overlapping sub-bands with length  $L$  are considered. Thus, the maximum number of echoes which can be estimated is  $L - 1$ .

These parameters are related to each other by the following expression:

$$N = L + M - 1 \quad (2.9)$$

Let  $\mathbf{r}'_k$  denote the  $(L \times 1)$  data vector of the  $k$ th sub-band. It can be written as:

$$\mathbf{r}'_k = \mathbf{A}_L \mathbf{D}^{k-1} \mathbf{s} + \mathbf{b}_k \quad (2.10)$$

where  $\mathbf{b}_k$  is the  $(L \times 1)$  noise vector of the  $k$ th sub-band,  $\mathbf{A}_L$  denotes the  $(L \times d)$  mode matrix (which is independent of parameter  $k$ ), and  $\mathbf{D}$  denotes the  $(d \times d)$  diagonal matrix expressed as:

$$\mathbf{D} = \text{diag} \left( e^{-2j\pi\Delta ft_1}, \dots, e^{-2j\pi\Delta ft_d} \right) \quad (2.11)$$

The noiseless cross-covariance matrix between the  $k$ th sub-bands and the  $l$ th sub-band  $\mathbf{R}_{kl}$  is written as follows:

$$\mathbf{R}_{kl} = \mathbf{A}_L \mathbf{D}^{k-1} \mathbf{S} (\mathbf{D}^{l-1})^H \mathbf{A}_L^H \quad (2.12)$$

The SSP technique estimates the data covariance matrix  $\mathbf{R}_{SSP}$  as the average of  $M$  frequency overlapping sub-bands as follows [32]:

$$\mathbf{R}_{SSP} = \frac{1}{M} \sum_{k=1}^M \mathbf{R}_{kk} \quad (2.13)$$

The MSSP method estimates the data covariance matrix  $\mathbf{R}_{MSSP}$  as follows [32]:

$$\mathbf{R}_{MSSP} = \frac{1}{2M} \sum_{k=1}^M \{ \mathbf{R}_{kk} + \mathbf{J} \mathbf{R}_{kk}^* \mathbf{J} \} \quad (2.14)$$

where  $\mathbf{J}$  is the  $(L \times L)$  exchange matrix and the operator  $*$  denotes the complex conjugate.

The ISSA method estimates the data covariance matrix  $\mathbf{R}_{ISSA}$  as follows [23]:

$$\mathbf{R}_{ISSA} = \frac{1}{2M} \sum_{k=1}^M \sum_{l=1}^M \{ \mathbf{R}_{kk} \mathbf{R}_{ll} + \mathbf{J} \mathbf{R}_{kk}^* \mathbf{R}_{ll}^* \mathbf{J} \} \quad (2.15)$$

The ISSB method estimates the data covariance matrix  $\mathbf{R}_{ISSB}$  as follows [33]:

$$\mathbf{R}_{ISSB} = \frac{1}{2M} \sum_{k=1}^M \sum_{l=1}^M \{\mathbf{R}_{kl}\mathbf{R}_{lk} + \mathbf{J}\mathbf{R}_{kl}^*\mathbf{R}_{lk}^*\mathbf{J}\} \quad (2.16)$$

In theory, the ISSB method takes full advantage of all the cross sub-band covariance matrices  $\mathbf{R}_{kl}$ , contrary to ISSA, SSP and MSSP methods which take advantage of only covariance matrices  $\mathbf{R}_{kk}$ .

### 2.4.1 Extension of spatial smoothing

In the context of this work, theoretically, when the radar pulse and the noise are taken into account, the two improved spatial smoothing techniques ISSA and ISSB cannot be used directly. In [23], the authors use a whitening process and neglect the radar pulse influence in the noise covariance matrix as follows:  $\mathbf{R}_0 = \mathbf{A}\mathbf{S}\mathbf{A}^H + \sigma^2\mathbf{\Sigma} \approx \mathbf{A}\mathbf{S}\mathbf{A}^H + \sigma^2\mathbf{I}$ . For a “ricker pulse”, this process can bring a small bias in the estimation [23], but generally, this bias can be higher, following the shape of the radar pulse. Note that this bias may also be higher in a context of any noise. We propose to take the radar pulse into account in the processing and use the propagator method (PM) or the eigenvalue method (EVM) to remove the noise matrix  $\sigma^2\mathbf{\Sigma}$ . The noise matrix is not an identity matrix and contains the radar pulse (see Eq. (2.7)). The noise variance  $\sigma^2$  can be estimated by PM or EVM and the radar pulse can also be measured by the signal backscattered from a metallic plane. Thus, the influence of the radar pulse can be cancelled by removing the noise matrix.

When ISSB method is used in this application, the radar pulse and the noise are taken into account, so the covariance matrix  $\mathbf{R}_{ISSB}$  is composed of 3 terms: the term coming only from the signal  $\mathbf{R}_a$ , the term coming only from the noise  $\mathbf{R}_b$ , and the interaction term between the signal and the noise  $\mathbf{R}_c$  as follows:

$$\mathbf{R}_{ISSB} = \frac{1}{2M} \sum_{k=1}^M \sum_{l=1}^M \{\bar{\mathbf{R}}_{kl}\bar{\mathbf{R}}_{lk} + \mathbf{J}\bar{\mathbf{R}}_{kl}^*\bar{\mathbf{R}}_{lk}^*\mathbf{J}\} = \mathbf{R}_a + \mathbf{R}_b + \mathbf{R}_c$$

with  $\bar{\mathbf{R}}_{kl} = E(\mathbf{r}'_k \mathbf{r}'_l{}^H) = \mathbf{A}_L \mathbf{D}^{k-1} \mathbf{S} (\mathbf{D}^{l-1})^H \mathbf{A}_L^H + \boldsymbol{\Sigma}_{kl}$  ( $\boldsymbol{\Sigma}_{kl} = E(\mathbf{b}_k \mathbf{b}_l^H)$ ). The expressions of  $\mathbf{R}_a$ ,  $\mathbf{R}_b$  and  $\mathbf{R}_c$  are as follows:

$$\begin{aligned} \mathbf{R}_a &= \frac{1}{2M} \sum_{k=1}^M \sum_{l=1}^M \{ \mathbf{A}_L \mathbf{D}^{k-1} \mathbf{S} (\mathbf{D}^{l-1})^H \mathbf{A}_L^H \mathbf{A}_L \mathbf{D}^{l-1} \mathbf{S} (\mathbf{D}^{k-1})^H \mathbf{A}_L^H + \mathbf{J} \{ \mathbf{A}_L \mathbf{D}^{k-1} \mathbf{S} (\mathbf{D}^{l-1})^H \\ &\quad \mathbf{A}_L^H \mathbf{A}_L \mathbf{D}^{l-1} \mathbf{S} (\mathbf{D}^{k-1})^H \mathbf{A}_L^H \}^* \mathbf{J} \} \\ \mathbf{R}_b &= \frac{1}{2M} \sum_{k=1}^M \sum_{l=1}^M \{ \{ \boldsymbol{\Sigma}_{kl} \boldsymbol{\Sigma}_{lk} \} + \mathbf{J} \{ \boldsymbol{\Sigma}_{kl} \boldsymbol{\Sigma}_{lk} \}^* \mathbf{J} \} \\ \mathbf{R}_c &= \frac{1}{2M} \sum_{k=1}^M \sum_{l=1}^M \{ \mathbf{A}_L \mathbf{D}^{k-1} \mathbf{S} (\mathbf{D}^{l-1})^H \mathbf{A}_L^H \boldsymbol{\Sigma}_{lk} + \boldsymbol{\Sigma}_{kl} \mathbf{A}_L \mathbf{D}^{l-1} \mathbf{S} (\mathbf{D}^{k-1})^H \mathbf{A}_L^H + \mathbf{J} \{ \mathbf{A}_L \mathbf{D}^{k-1} \\ &\quad \mathbf{S} (\mathbf{D}^{l-1})^H \mathbf{A}_L^H \boldsymbol{\Sigma}_{lk} + \boldsymbol{\Sigma}_{kl} \mathbf{A}_L \mathbf{D}^{l-1} \mathbf{S} (\mathbf{D}^{k-1})^H \mathbf{A}_L^H \}^* \mathbf{J} \} \end{aligned}$$

The interaction term  $\mathbf{R}_c$  must be removed for using ISSB without approximations. This can also be solved by using PM or EVM. After using PM (or EVM) and then ISSB, the term coming only from the noise and the interaction term are removed, then the covariance matrix becomes:

$$\mathbf{R}_{ISSB-PM} = \mathbf{R}_a$$

## 2.4.2 Noise power estimation

In this subsection, we present two methods for estimating the noise variance, one is EVM and another is PM. EVM is proven to be statistically efficient [28]. PM is shown to be more efficient than EVM from the computational burden standpoint of view, but it is less statistically efficient than EVM [27].

For totally uncorrelated echoes, the EVM estimates the noise variance  $\sigma^2$  as:

$$\hat{\sigma}^2 = \frac{1}{N-d} \sum_{k=d+1}^N \lambda_k \quad (2.17)$$

where  $\lambda_i$ , ( $i = d+1, \dots, N$ ) are the  $N-d$  smallest eigenvalues (in theory,  $\lambda_{d+1} = \lambda_{d+2} = \dots = \lambda_N = \sigma^2$ ) of the covariance matrix  $\mathbf{Y}$  in (2.4),  $\hat{\sigma}^2$  is the estimated noise variance. When the echoes are coherent, the above result remains valid [28].

For PM, the covariance matrix  $\mathbf{Y}$  can be divided into:

$$\mathbf{Y} = \begin{pmatrix} \mathbf{G}_1 & \mathbf{H}_1 \\ \mathbf{G}_2 & \mathbf{H}_2 \end{pmatrix} \quad (2.18)$$

where  $\mathbf{G}_1$ ,  $\mathbf{G}_2$ ,  $\mathbf{H}_1$  and  $\mathbf{H}_2$  are  $(d \times d)$ ,  $((N-d) \times d)$ ,  $(d \times (N-d))$  and  $((N-d) \times (N-d))$  dimensional matrices, respectively. The noise variance  $\sigma^2$  can be deduced as follows [27]:

$$\sigma^2 = \frac{\text{tr}\{\mathbf{H}_2\mathbf{\Pi}\}}{\text{tr}\{\mathbf{\Pi}\}} \quad (2.19)$$

where  $\mathbf{\Pi} = \mathbf{I}_{N-d} - \mathbf{G}_2\mathbf{G}_2^+$ ,  $\text{tr}\{\cdot\}$  is the trace matrix operator,  $+$  is the Moore-Penrose inverse operator, and  $\mathbf{I}_i$  is the  $(i \times i)$  dimensional identity matrix. Matrices  $\mathbf{G}_2$  and  $\mathbf{H}_2$  are defined as

$$\begin{aligned} \mathbf{G}_2 &= \mathbf{\Lambda}_{N-d}\mathbf{A}_{N-d}\mathbf{S}\mathbf{A}_d^H\mathbf{\Lambda}_d^H \\ \mathbf{H}_2 &= \mathbf{\Lambda}_{N-d}\mathbf{A}_{N-d}\mathbf{S}\mathbf{A}_{N-d}^H\mathbf{\Lambda}_{N-d}^H + \sigma^2\mathbf{I}_{N-d} \end{aligned}$$

where  $\mathbf{\Lambda}_d\mathbf{A}_d$  and  $\mathbf{\Lambda}_{N-d}\mathbf{A}_{N-d}$  are  $(d \times d)$  and  $((N-d) \times (N-d))$  dimensional matrices, respectively. It can be shown that

$$\begin{aligned} \mathbf{\Lambda}\mathbf{A} &= \begin{pmatrix} \mathbf{\Lambda}_d\mathbf{A}_d \\ \mathbf{\Lambda}_{N-d}\mathbf{A}_{N-d} \end{pmatrix} \\ &= \begin{pmatrix} \mathbf{\Lambda}_d & \mathbf{0} \\ \mathbf{0} & \mathbf{\Lambda}_{N-d} \end{pmatrix} \begin{pmatrix} \mathbf{A}_d \\ \mathbf{A}_{N-d} \end{pmatrix} \end{aligned} \quad (2.20)$$

Under the assumption that the rank of  $\mathbf{A}_d$  is  $d$ , one should notice that the estimated noise variance has a unique solution only when  $N-d \geq d$  [27].

As the radar pulse is known and the noise variance  $\sigma^2$  is estimated, the new covariance matrix  $\mathbf{R}_{noiseless}$  can be written as:

$$\mathbf{R}_{noiseless} = \mathbf{A}\mathbf{S}\mathbf{A}^H \approx \mathbf{R}_0 - \hat{\sigma}^2\mathbf{\Sigma} \quad (2.21)$$

The preprocessing PM or EVM combined with a sub-band averaging technique is applied. Then, high resolution methods can be used to estimate the time delays of backscattered echoes. In the following section, we define  $\mathbf{R}$  as the new covariance matrix after using sub-band averaging techniques and PM (or EVM).

## 2.5 Subspace methods

### 2.5.1 Introduction

Subspace methods or high resolution methods are a class of algorithms which are based on the eigenstructure properties of the data covariance matrix. They are known because of their high-resolution ability and yield accurate estimates compared to conventional methods. These algorithms have given rise to a large number of applications in the areas of array signal processing [34, 35, 36] and spectral analysis [32, 37] and applications for TDE [12, 15, 23, 38, 39]. In this section, we present the three most prominent subspace methods: Multiple Signal Classification (MUSIC) [34], root-MUSIC [35] and Estimation of Signal Parameter via Rotational Invariance Techniques (ESPRIT) [36]. These algorithms can be applied for both impulse GPR and step-frequency GPR.

### 2.5.2 MUSIC

MUSIC algorithm was originally presented as a DOA estimator. Recently, it has been successfully developed for spectral analysis [40]. In this subsection, we present MUSIC algorithm for the TDE of radar echoes in order to measure the thicknesses of a stratified media.

The structure of the covariance matrix  $\mathbf{R}$  after sub-band averaging techniques and de-noising can be written in terms of its eigenvalues and eigenvectors as:

$$\mathbf{R} = \mathbf{U}_S \mathbf{\Lambda}_S \mathbf{U}_S^H + \mathbf{U}_N \mathbf{\Lambda}_N \mathbf{U}_N^H \quad (2.22)$$

where  $\mathbf{\Lambda}_S$  is a diagonal matrix which contains the  $d$  largest eigenvalues, and its associated eigenvectors are in  $\mathbf{U}_S$  (the matrix of signal eigenvectors).  $\mathbf{\Lambda}_N$  is a diagonal matrix which contains the  $L - d$  smallest eigenvalues, and its associated eigenvectors are in  $\mathbf{U}_N$  (the matrix of noise eigenvectors). Since the mode matrix  $\mathbf{A}_L$  is orthogonal to  $\mathbf{U}_N$ , the MUSIC pseudo-spectrum can be written as:

$$P_{MUSIC}(t) = \frac{1}{\mathbf{a}^H(t) \mathbf{U}_N \mathbf{U}_N^H \mathbf{a}(t)} \quad (2.23)$$

The time delay can be estimated by searching the peak positions of the MUSIC pseudo-spectrum  $P_{MUSIC}(t)$ . Fig. 2.4 shows the MUSIC pseudo-spectrum to estimate the time delays of backscattered echoes. The two peaks exactly correspond to the true

time delays, which means that the time delays are well estimated; on the contrary, the IFT cannot distinguish these two delays when  $B\Delta\tau \leq 1$ .

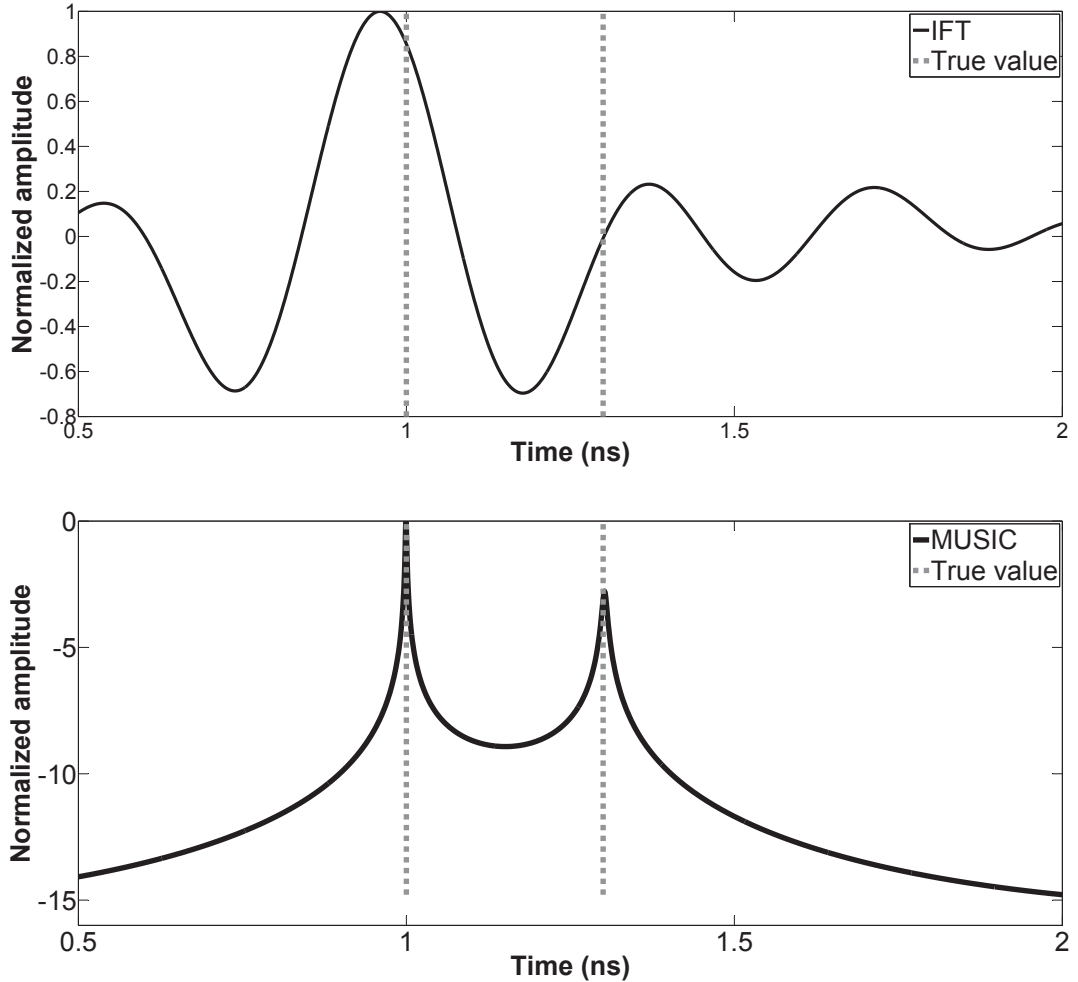


Figure 2.4: Simulation results of IFT and MUSIC for TDE (the true time delays are 1 ns and 1.3 ns, SSP is used for bandwidth  $B = 2$  GHz,  $B\Delta\tau = 0.6$  and  $\text{SNR} = 20$  dB)

### 2.5.3 Root-MUSIC

For MUSIC algorithm, it allows to search through all time to find the true time delays of echoes. It demands a very large computation time. When the frequency sampling is uniformly linear, we can use the polynomial rooting for TDE instead of searching in the time spectrum, this algorithm is called root-MUSIC.

Defining  $z = \exp(-j2\pi\Delta ft)$ , the model vector  $\mathbf{a}(t)$  becomes  $\mathbf{a}(z) = \exp(-2j\pi f_1 t) [1 \ z \ \dots \ z^{L-1}]^T$ . Thus, finding the set of  $t$  maximizing  $P_{MUSIC}(t)$  is equivalent to find-

ing the roots of the following polynomial, known as root-MUSIC polynomial (RMP):

$$P(z) = \mathbf{a}^H(z)\mathbf{U}_N\mathbf{U}_N^H\mathbf{a}(z) = \mathbf{a}^T(z^{-1})\mathbf{U}_N\mathbf{U}_N^H\mathbf{a}(z) \quad (2.24)$$

As  $\mathbf{U}_N\mathbf{U}_N^H$  is Hermitian, the roots of  $P(z)$  are conjugate symmetric. Therefore, if  $z_i$  is a root of  $P(z)$ , so is  $1/z_i^*$ . Hence, half of the roots will be inside the unit circle and the other half of the roots will be outside the unit circle. In practice, time delays will be estimated from the roots inside and closest to the unit circle. Fig. 2.5 gives an example of the roots of the RMP. Only the roots inside the unit circle are taken into account and the estimated time delays are calculated from the roots which are closest to the unit circle. From Fig. 2.5, the two roots closest to the unit circle coincide with the true values.

#### 2.5.4 ESPRIT

Among subspace methods, ESPRIT affords a direct parameter estimation with a lower computational complexity. Like MUSIC, ESPRIT has also been originally proposed for DOA estimation. In this subsection, ESPRIT is also used for TDE.

ESPRIT algorithm divides the mode matrix  $\mathbf{A}_L$  into two overlapping data sub-bands. Sub-bands comprise of  $L - 1$  samples and overlap with each other by  $L - 2$  samples. The  $((L - 1) \times d)$  dimensional mode matrices of each sub-band,  $\mathbf{A}_1$  and  $\mathbf{A}_2$ , are related to each other by the  $(d \times d)$  diagonal matrix  $\mathbf{D}$ , whose elements depend on the time-delay to be estimated as:

$$\mathbf{A}_2 = \mathbf{A}_1\mathbf{D} \quad (2.25)$$

such that

$$\mathbf{A}_L = \begin{pmatrix} \mathbf{A}_1 \\ - \\ \mathbf{A}_2 \end{pmatrix} = \begin{pmatrix} - \\ \mathbf{A}_2 \end{pmatrix} \quad (2.26)$$

As matrix  $\mathbf{D} = \text{diag}(e^{-2j\pi t_1 \Delta f}, \dots, e^{-2j\pi t_d \Delta f})$  cannot be estimated from data, according to [38], on the basis of the eigendecomposition of the data covariance matrix, it can be shown that the diagonal elements of  $\mathbf{D}$  can be retrieved from the similar matrix  $\mathbf{\Psi}$  which has the same eigenvalues as  $\mathbf{D}$ :

$$\mathbf{\Psi} = \mathbf{T}^{-1}\mathbf{D}\mathbf{T} \quad (2.27)$$

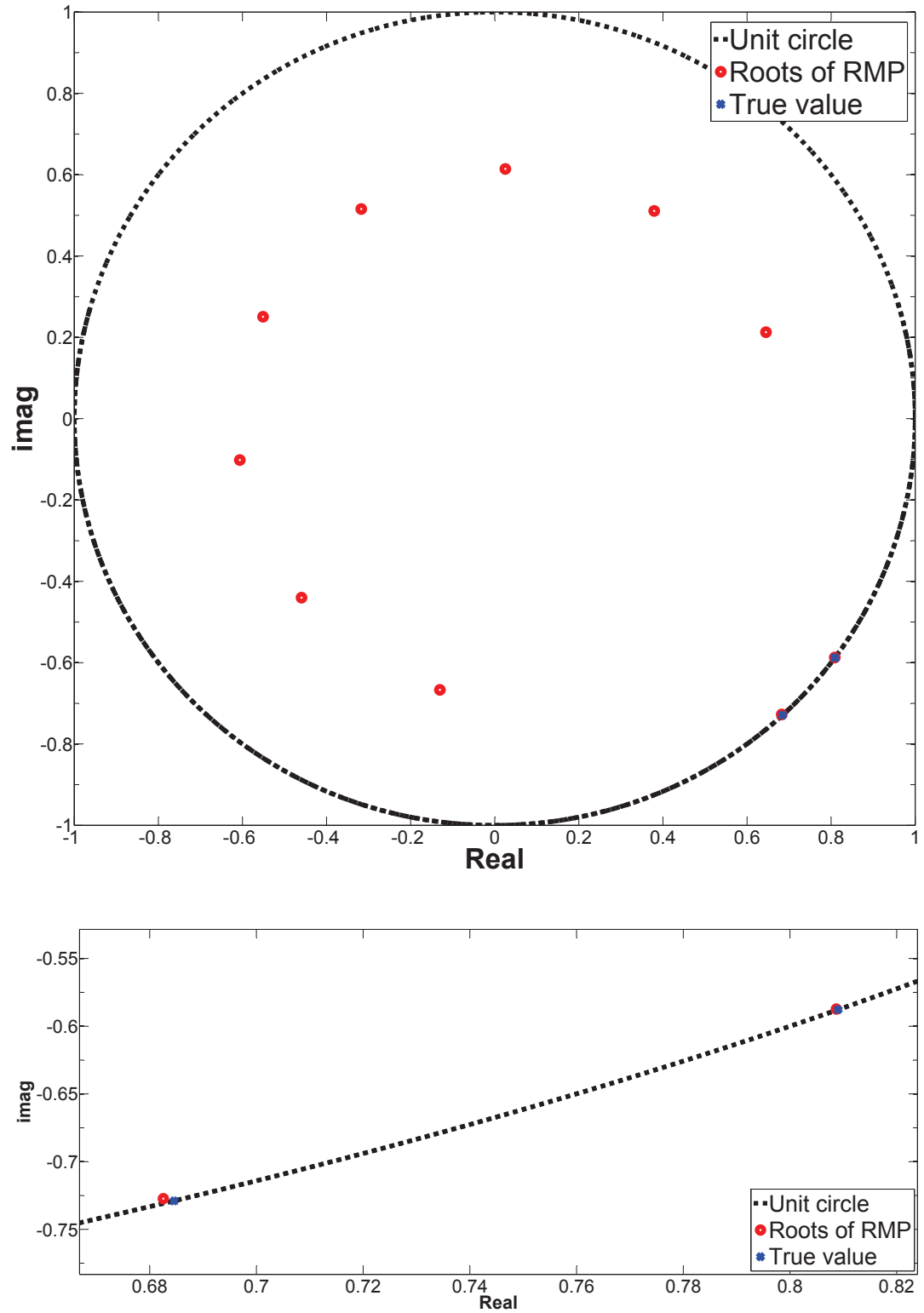


Figure 2.5: Roots of RMP (the true time delays are 1 ns and 1.3 ns, SSP is used for bandwidth  $B = 2$  GHz,  $B\Delta\tau = 0.6$  and SNR=20 dB)

where  $\mathbf{T}$  is a  $(d \times d)$  dimensional invertible matrix. From the eigendecomposition of the signal covariance matrix after sub-band averaging techniques  $\mathbf{R}_{sig} = \mathbf{A}_L \bar{\mathbf{S}} \mathbf{A}_L^H$  ( $\bar{\mathbf{S}}$  is a covariance matrix of vector  $\mathbf{s}$  after sub-band averaging techniques), we have:

$$\mathbf{R}_{sig} \mathbf{V}_{sig} = \mathbf{V}_{sig} \mathbf{K} \quad (2.28)$$

where the eigenvectors  $\mathbf{v}_k$  associated with the signal subspace are arranged in the matrix  $\mathbf{V}_{sig}$  as columns, matrix  $\mathbf{K} = \text{diag}(\lambda_1, \lambda_2, \dots, \lambda_d)$ ;  $\lambda_i$  is the  $i$ th eigenvalue of covariance matrix  $\mathbf{\Gamma}_{sig}$ . Because matrix  $\mathbf{D}$  cannot be estimated from data, ESPRIT further exploits the linear relation in Eq. (2.25) within the eigendecomposition of the data covariance matrix in Eq. (2.28). Let us write Eq. (2.28) in each sub-band data as follows:

$$\mathbf{R}_{sig,1} \mathbf{V}_{sig} = \mathbf{V}_{sig,1} \mathbf{K} \quad (2.29)$$

$$\mathbf{R}_{sig,2} \mathbf{V}_{sig} = \mathbf{V}_{sig,2} \mathbf{K} \quad (2.30)$$

where  $\mathbf{R}_{sig,j}$  ( $j = 1, 2$ ) are the  $((L-1) \times L)$  dimensional matrices, defined from the partitioning of the signal covariance matrix, which are expressed as:

$$\mathbf{R}_{sig,1} = \mathbf{A}_1 \bar{\mathbf{S}} \mathbf{A}_L^H \quad (2.31)$$

$$\mathbf{R}_{sig,2} = \mathbf{A}_2 \bar{\mathbf{S}} \mathbf{A}_L^H \quad (2.32)$$

where  $\mathbf{V}_{sig,1}$  and  $\mathbf{V}_{sig,2}$  are the two sub-matrices of  $\mathbf{V}_{sig}$  defined as:

$$\mathbf{V}_{sig} = \begin{pmatrix} \mathbf{V}_{sig,1} \\ - \end{pmatrix} = \begin{pmatrix} - \\ \mathbf{V}_{sig,2} \end{pmatrix} \quad (2.33)$$

At the first step, the latter definition and the expression of  $\mathbf{A}_2$  in Eq. (2.25) are substituted for Eq. (2.30). Some mathematical manipulations lead to the following equation:

$$\mathbf{A}_1 \mathbf{D} \mathbf{T} = \mathbf{V}_{sig,2} \quad (2.34)$$

where

$$\mathbf{T} = \bar{\mathbf{S}} \mathbf{A}_L^H \mathbf{V}_{sig} \mathbf{K}^{-1} \quad (2.35)$$

Similarly, Eqs. (2.29), (2.31) and (2.32) are used to obtain the following expression

for the matrix  $\mathbf{A}_1$ :

$$\mathbf{A}_1 = \mathbf{V}_{sig,1} \mathbf{T}^{-1} \quad (2.36)$$

At the second step, substituting Eq. (2.36) for Eq. (2.34) leads to:

$$\mathbf{V}_{sig,1} \mathbf{T}^{-1} \mathbf{D} \mathbf{T} = \mathbf{V}_{sig,2} = \mathbf{V}_{sig,1} \mathbf{\Psi} \quad (2.37)$$

where  $\mathbf{\Psi}$  is a  $(d \times d)$  dimensional matrix defined in Eq. (2.27), which shows that  $\mathbf{\Psi}$  and  $\mathbf{D}$  are similar matrices, therefore they have the same eigenvalues. A least squares solution can be used to calculate  $\mathbf{\Psi}$  from Eq. (2.37):

$$\mathbf{\Psi} = \left( (\mathbf{V}_{sig,1})^H \mathbf{V}_{sig,1} \right)^{-1} (\mathbf{V}_{sig,1})^H \mathbf{V}_{sig,2}$$

The time delays can be estimated from the eigenvalues of  $\mathbf{\Psi}$  as follows:

$$t_k = -\angle \psi_k / (2\pi \Delta f) \quad (2.38)$$

where  $\psi_k$  is the  $k$ th eigenvalue of  $\mathbf{\Psi}$ ,  $\angle$  is the angle.

## 2.6 Performance evaluation

In this section, the performance of the high resolution methods: MUSIC, root-MUSIC and EPSRIT combined with sub-band averaging techniques are tested on simulated data. In order to use ISS, we select the PM to estimate the noise variance. The performance of the studied algorithms herein is accessed by the Relative-Root-Mean-Square Error (RRMSE) on estimated time delays.

### 2.6.1 Simulation parameters

The performance of the algorithms is evaluated by a Monte-Carlo process of 100 independent runs. The simulation data represent the radar backscattered echoes at nadir from a layer made up of two interfaces separating homogeneous media. The studied structure is made up of a layer medium of UTAS with relative permittivity equal to 4.5 overlying a baseband with relative permittivity equal to 7; the layer thickness can be estimated from the TDE of the first two echoes. The frequency band is 1.0 – 3.0 GHz, with 0.1 GHz steps (21 frequency samples), the radar pulse is a ricker [23]. The

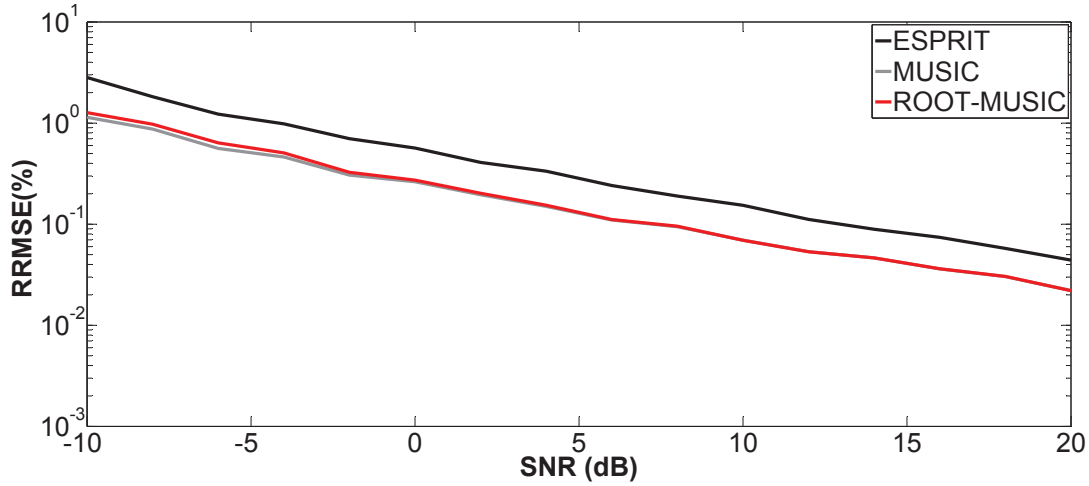


Figure 2.6: RRMSE on the estimated times of arrival  $t_1$  versus SNR, totally uncorrelated

four preprocessing ISSA, ISSB, MSSP and SSP with PM are used to reduce the cross-correlation between echoes, the number of sub-bands ( $M$ ) equals to 10. The ideal situation corresponding to the situation where the echoes are totally uncorrelated is also studied. It allows determining the best performance and limitations of the algorithms. For each run, the covariance matrix is estimated from 50 independent snapshots. The SNR is defined as the ratio between the power of the second echo and the noise variance. The performance of MUSIC, root-MUSIC and ESPRIT combined with ISSA, ISSB, MSSP and SSP is assessed from the RRMSE of the studied parameter:

$$RRMSE(z) = \frac{\sqrt{\frac{1}{U} \sum_{j=1}^U (\hat{z}_j - z)^2}}{z} \quad (2.39)$$

where  $\hat{z}_j$  denotes the estimated parameter for the  $j$ th run of the algorithm and  $z$  the true value,  $U$  is the number of Monte-Carlo processes. In the following simulations, the parameter  $z$  can represent either the first ( $t_1$ ) or the second ( $t_2$ ) time delay.

## 2.6.2 Simulation results

In the simulations, we consider two backscattered echoes corresponding to the time delays 1 ns and 1.3 ns, which correspond to a layer thickness  $H \approx 20$  mm. The two echoes are slightly overlapped with  $B\Delta\tau$  product equal to 0.6 [12]. In addition, a comparison in terms of different SNR is made between the 4 sub-band averaging techniques.

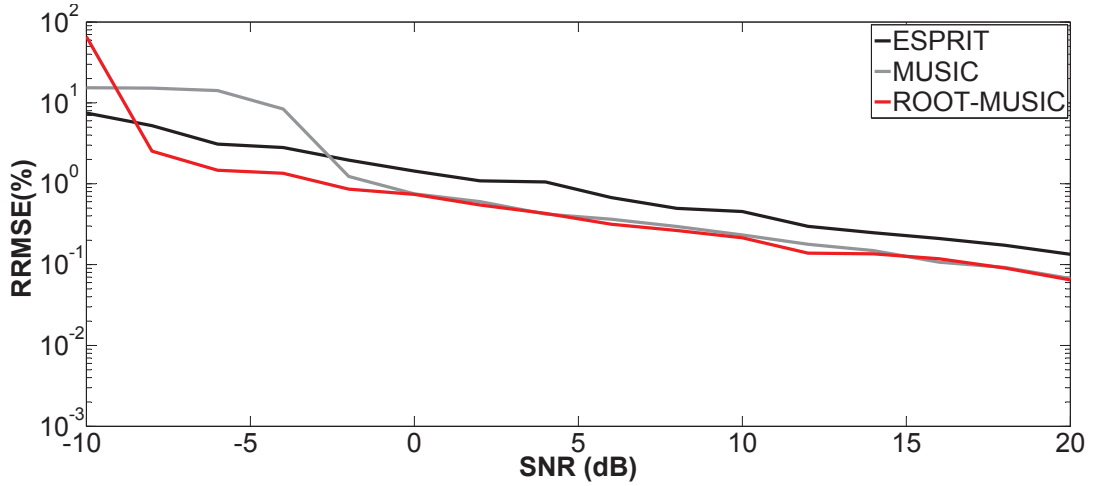


Figure 2.7: RRMSE on the estimated times of arrival  $t_2$  versus SNR, totally uncorrelated

Figs. 2.6 and 2.7 plot the RRMSE on the estimated time delay  $\hat{t}_1$  or  $\hat{t}_2$  when the echoes are totally uncorrelated. As expected, it can be seen that the RRMSE continuously decreases with increasing SNR. Root-MUSIC offers the best performance compared to ESPRIT and MUSIC, especially for the second echo. However, at high SNR values, these subspace methods tend toward similar performances (the curves of RRMSE versus SNR coincide with each other). Figs. 2.8-2.10 provide the RRMSE on the estimated time delay by MUSIC, root MUSIC and ESPRIT combined with ISSA, ISSB, MSSP and SSP when the echoes are fully correlated. From the simulation results, we can conclude that the selected subspace methods with ISS, especially the methods with ISSB give better results at low SNR. The power to decorrelate the echoes among the four sub-band averaging techniques can be written as ISSB > ISSA > MSSP > SSP. The main drawback of ISS is that the methods require a little more computational time to implement than SSP and MSSP.

## 2.7 Conclusion

In this chapter, we have presented the methods for TDE with impulse GPR and step-frequency GPR in measuring pavement layers.

For the conventional methods, the IFT and cross-correlation method are presented (the IFT for step-frequency GPR and the cross-correlation method for impulse GPR). They offer low computational costs and are able to detect time delays with non-overlapped echoes. Nevertheless, their ability is limited to detect closely spaced time delays. Be-

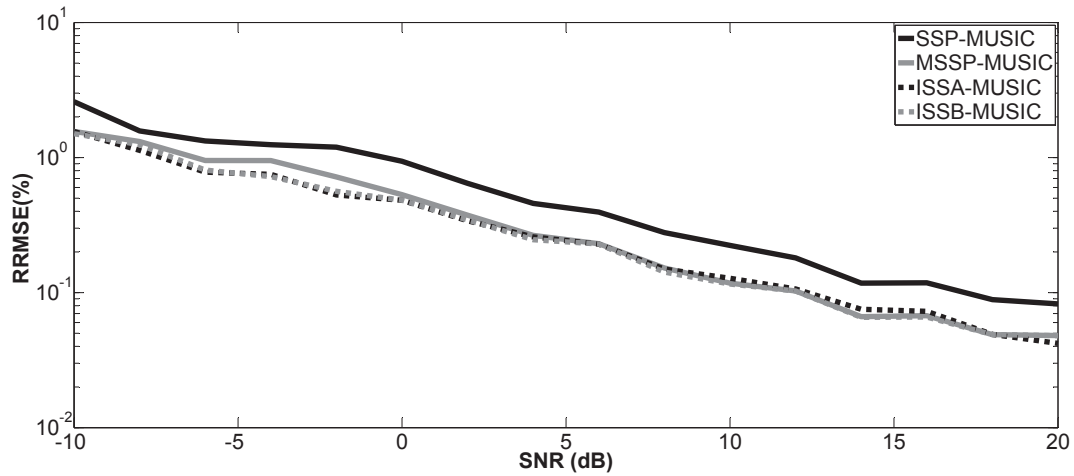
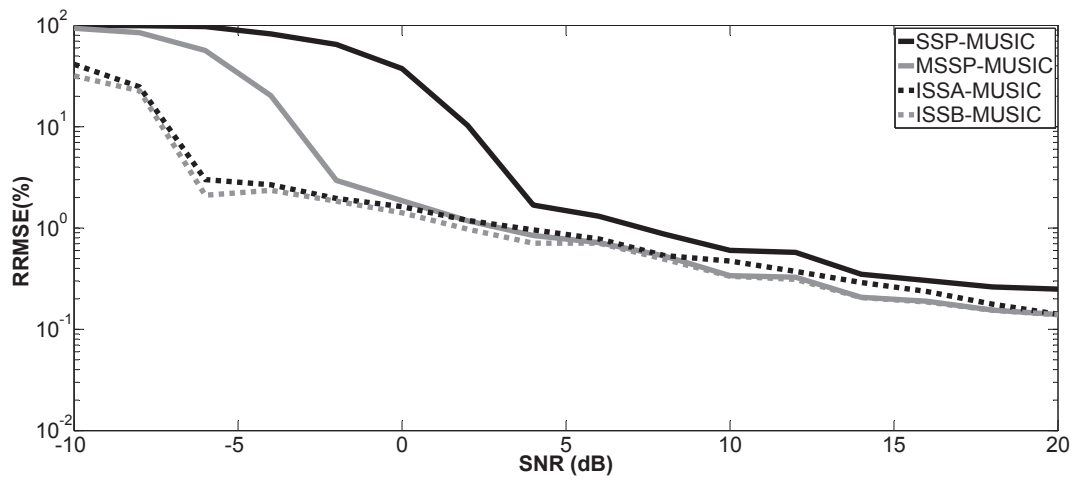
(a)  $t_1$ (b)  $t_2$ 

Figure 2.8: RRMSE on the estimated times of arrival  $t_k$  ( $k = 1, 2$ ) versus SNR by MUSIC, fully correlated

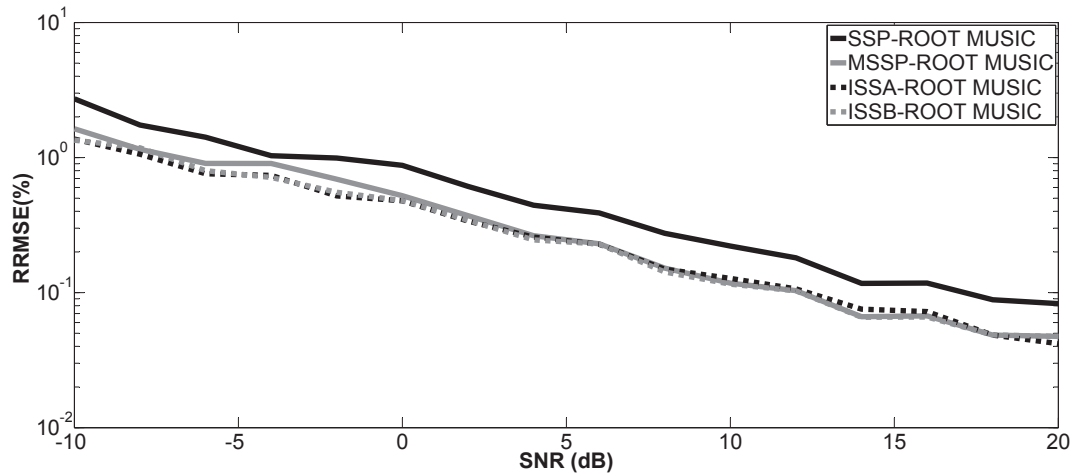
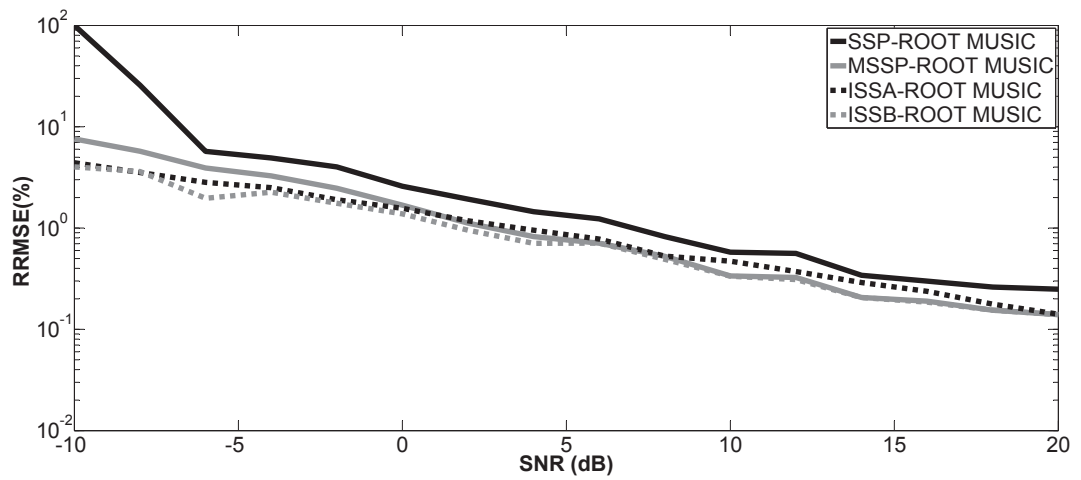
(a)  $t_1$ (b)  $t_2$ 

Figure 2.9: RRMSE on the estimated times of arrival  $t_k$  ( $k = 1, 2$ ) versus SNR by root-MUSIC, fully correlated

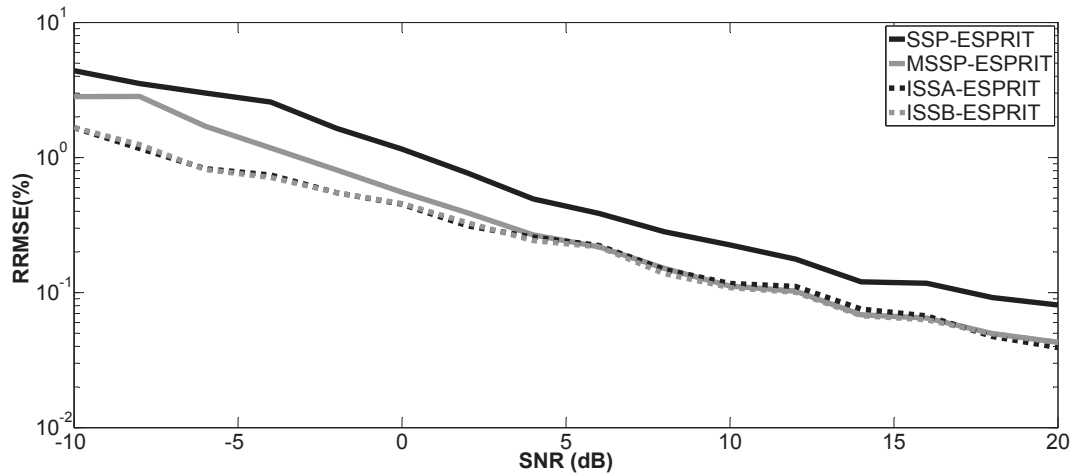
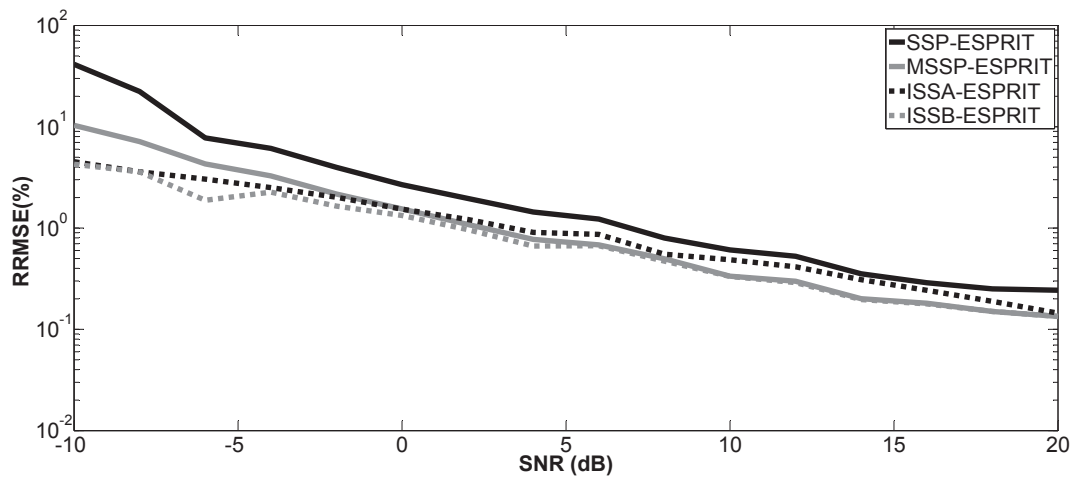
(a)  $t_1$ (b)  $t_2$ 

Figure 2.10: RRMSE on the estimated times of arrival  $t_k$  ( $k = 1, 2$ ) versus SNR by ESPRIT, fully correlated

cause, this kind of methods has a resolution which depend on the frequency bandwidth, such as  $B\Delta\tau$ .

In order to enhance the GPR performance, high resolution methods are used. they allow the estimation of thickness of thin pavement. Three well-known algorithms (MUSIC, root-MUSIC and ESRPIT) are applied for the TDE. In practice, GPR signals are coherent or highly correlated; thus, the correlation of backscattered echoes is enough to degrade the performance of high resolution methods. For this purpose, we have extended the sub-band averaging techniques ISSA and ISSB (with PM) to decorrelate the backscattered echoes. The solutions do not use any approximation and are more powerful than traditional SSP and MSSP.

The performance of the high resolution methods (MUSIC, root-MUSIC and ESPRIT) combined with sub-band averaging techniques (SSP, MSSP, ISSA and ISSB) is tested on the simulated data. We have calculated the RRMSE on the estimated time delays with changes of SNR (from  $-10$  dB to  $20$  dB). Numerical examples are provided to show the performance of the algorithms. The simulation results show that the proposed methods have better results especially at low SNR. In the following chapters, the influence of interface roughness is considered in the signal model and new signal processing methods are presented.



## Rough pavement scattering model

### 3.1 Introduction

In civil engineering, conventional methods are used to estimate the layer thickness by assuming the interfaces of the layer to be flat (like in the previous chapter). In contrast to the existing literature, in this chapter, the interface roughness is taken into account and we propose to extend the previous sensitivity analysis in [15] to larger bandwidths. The influence of interface roughness on the frequency behaviour of backscattered echoes in different frequency bands (narrow bands, middle bands and large bands) is studied.

Compared to flat interfaces, this work requires more sophisticated electromagnetic modelling of GPR. For GPR, numerical simulation is an efficient way to analyse probing problems and to study the EM (electromagnetic) wave propagation inside the considered medium. For example, GPRMax, which is based on the Finite-Difference Time-Domain (FDTD) method, is an open source software that simulates electromagnetic wave propagation and is able to handle objects with rough surfaces. It is designed for simulating GPR but can also be used to model electromagnetic wave propagation for many other applications. In addition, ray tracing and FEA (finite element analysis) are also common methods for numerical simulation, which are widely used for simulating the radar response over typical road diseases (surface cracks, base cracks and base replacements) [6, 7, 41, 42, 43]. Nevertheless, these methods have a high com-

putational complexity and/or a restricted domain of validity. An effective frequency-domain numerical method called PILE [24, 44] is used in this thesis to compute the field scattered by the stratified medium with random rough interfaces. Within the scope of signal processing, the major interest of PILE relies on its capability to split the total scattered field into each echo contribution.

The rigorous electromagnetic method PILE provides the simulated data that show the influence of interface roughness on the backscattered primary echoes of stratified media. The interface roughness provides a continuous frequency decay of the magnitude of echoes. The observed frequency variations of the radar magnitude introduce some shape distortion in the radar waveform. The latter variations can be modelled by functions which provide satisfactory results for different bandwidths.

Section 2 briefly recalls the rigorous numerical method PILE for simulating the scattering of EM waves by layered random rough interfaces. As a result, the frequency behaviour of backscattered echoes is investigated with respect to their magnitude. Magnitude variations are found to prevail on phase variations. The studied frequency band is extended to  $f \in [0.5; 10.5]$  GHz in order to deal with existing radar systems, especially UWB step-frequency radars. The sensitivity of the echo magnitude to interlayer roughness is also studied in order to better understand how the interlayer roughness impacts the backscattered echoes. Curve fittings are proposed to model the latter frequency variations by using a LMSE (least mean squares error) technique in narrow, middle and large frequency bands in section 3. The parameter responsible for the frequency variations can be estimated by curve fittings. This new parameter is called roughness parameter. It will be taken into account in the data model in following chapters. Finally, conclusions are drawn.

## 3.2 PILE method

In this section, the rigorous numerical method PILE proposed in [44] is used to calculate the field scattered from a layered pavement medium with random rough interfaces. This study takes realistic scenarios of a thin pavement structure by taking the interface roughness into account. It focuses on 2D problems with so-called 1-D surfaces. The two surfaces (which are assumed to be uncorrelated between each other) are slightly rough and are characterized by a Gaussian height probability density function and an exponential height autocorrelation function [15]. The antenna is assumed to radiate a vertically polarised plane wave in far field of probed pavement. The antenna radiation pattern is a tapered Thorsos beam whose parameter is chosen to match the

pattern of an ETSA antenna (Exponentially Tapered Slot Antenna) used for such measurements [45]. PILE method has several advantages compared with other numerical methods. Firstly, the formulation of PILE method is simple and it has a straightforward physical interpretation [44]. Then, compared with other MoM-based numerical methods, PILE method is appropriate to compute the different backscattered echoes  $s_k = E_k/E_i$ , with  $E_i$  the incident field,  $E_k$  the  $k$ th scattered field (see Fig. 3.1, with  $k = 1, 2$ ). Finally, compared with asymptotic methods, PILE method affords reliable results over a large range of interface roughness. In the following, the study is limited to the first two scattered primary echoes, namely  $s_1$  and  $s_2$  in Fig. 3.1.

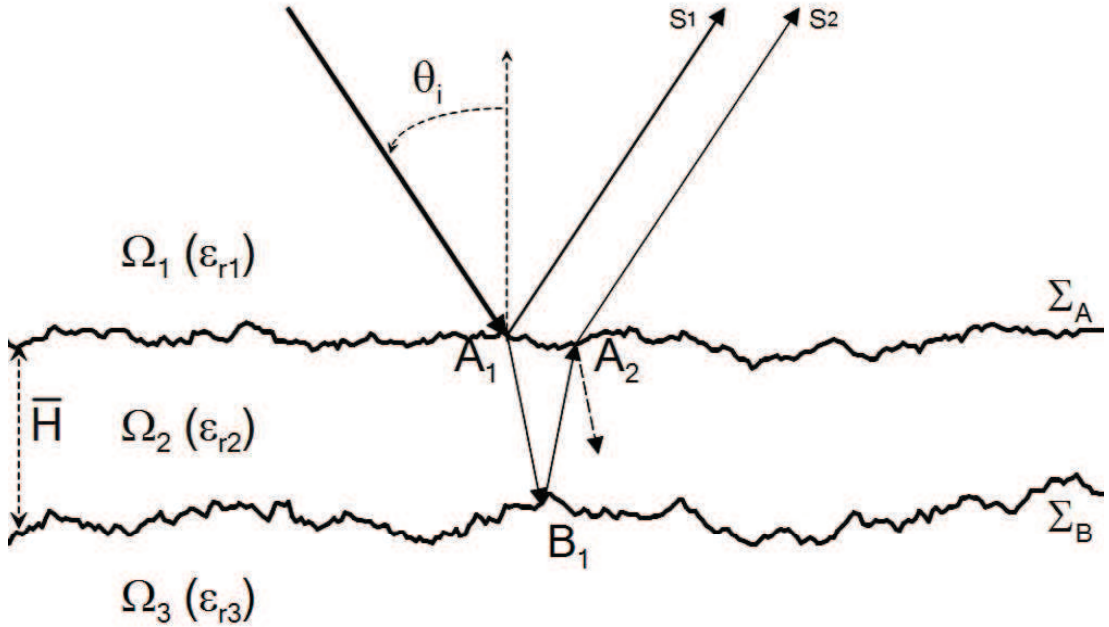


Figure 3.1: Rough pavement configuration

### 3.2.1 Principle of PILE method

In this subsection, we briefly present the principle of PILE method [44]. Based on the MoM, the total scattered field is expressed by integral equations and is transformed into the following linear system [44]:

$$\mathbf{Z}\mathbf{x} = \mathbf{b} \quad (3.1)$$

where  $\mathbf{x}$  is a  $(4N \times 1)$  vector representing the unknown total field on the surface ( $N$  is the number of samples for the MoM calculation). Then  $\mathbf{x}$  can be expressed as:

$$\mathbf{x} = \begin{pmatrix} \mathbf{x}_+ \\ \mathbf{x}_- \end{pmatrix}$$

with  $\mathbf{x}_+$  and  $\mathbf{x}_-$  are  $(2N \times 1)$  vectors containing information of field from upper and lower interfaces of the layer, respectively. Meanwhile,  $\mathbf{b}$  is a  $(4N \times 1)$  incident field vector with expression:

$$\mathbf{b} = \begin{pmatrix} \mathbf{b}_+ \\ \mathbf{b}_- \end{pmatrix}$$

with  $\mathbf{b}_+$  and  $\mathbf{b}_-$  are  $(2N \times 1)$  vectors containing the information of the incident field of upper and lower interfaces of the layer, or the information of the incident field inside medium  $\Omega_1$  and medium  $\Omega_2$ , respectively (see Fig. 3.1). Obviously, there is no incident wave inside medium  $\Omega_2$ , hence  $\mathbf{b}_- = \mathbf{0}$ .  $\mathbf{Z}$  is a  $(4N \times 4N)$  impedance matrix, with

$$\mathbf{Z} = \begin{pmatrix} \mathbf{Z}_U & \mathbf{C}_U \\ \mathbf{C}_L & \mathbf{Z}_L \end{pmatrix}$$

$\mathbf{Z}_U$  and  $\mathbf{Z}_L$  are  $(2N \times 2N)$  impedance matrices of the upper and lower interfaces, respectively.  $\mathbf{C}_U$  and  $\mathbf{C}_L$  can be interpreted as coupling matrices between the upper and lower interfaces.  $\mathbf{C}_L$  propagates information from the lower interface toward the upper interface and  $\mathbf{C}_U$  from upper surface toward the lower one.

PILE method provides an efficient way to solve Eq. 3.1 and to split up the total scattered field into each echo contribution. The detail is shown as follows:

Firstly, we assume the inverse matrix  $\mathbf{Z}^{-1}$  to be [44]

$$\mathbf{Z}^{-1} = \begin{pmatrix} \mathbf{G} & \mathbf{K} \\ \mathbf{P} & \mathbf{Q} \end{pmatrix}$$

with

1.  $\mathbf{G} = [\mathbf{Z}_U - \mathbf{C}_U \mathbf{Z}_L^{-1} \mathbf{C}_L]^{-1}$ ;
2.  $\mathbf{K} = -\mathbf{G} \mathbf{C}_U \mathbf{Z}_L^{-1}$ ;
3.  $\mathbf{P} = -\mathbf{Z}_L^{-1} \mathbf{C}_L \mathbf{G}$ ;
4.  $\mathbf{Q} = \mathbf{Z}_L^{-1} - \mathbf{Z}_L^{-1} \mathbf{C}_L \mathbf{G} \mathbf{C}_U \mathbf{Z}_L^{-1}$ .

Then, the unknown vector  $\mathbf{x} = \mathbf{Z}^{-1}\mathbf{b}$  is given by

$$\mathbf{x} = \begin{pmatrix} \mathbf{x}_+ \\ \mathbf{x}_- \end{pmatrix} = \begin{pmatrix} \mathbf{G} & \mathbf{K} \\ \mathbf{P} & \mathbf{Q} \end{pmatrix} \begin{pmatrix} \mathbf{b}_+ \\ \mathbf{0} \end{pmatrix} = \begin{pmatrix} \mathbf{G}\mathbf{b}_+ \\ \mathbf{P}\mathbf{b}_+ \end{pmatrix} \quad (3.2)$$

The scattered information inside the upper medium  $\Omega_1$  can be obtained from vector  $\mathbf{x}_+$ :

$$\begin{aligned} \mathbf{x}_+ &= \mathbf{G}\mathbf{b}_+ = (\mathbf{Z}_U - \mathbf{C}_U\mathbf{Z}_L^{-1}\mathbf{C}_L)^{-1}\mathbf{b}_+ \\ &= (\mathbf{I} - \mathbf{Z}_U^{-1}\mathbf{C}_U\mathbf{Z}_L^{-1}\mathbf{C}_L)^{-1}\mathbf{Z}_U^{-1}\mathbf{b}_+ \\ &= (\mathbf{I} - \mathbf{M})^{-1}\mathbf{Z}_U^{-1}\mathbf{b}_+ \end{aligned} \quad (3.3)$$

where  $\mathbf{M} = \mathbf{Z}_U^{-1}\mathbf{C}_U\mathbf{Z}_L^{-1}\mathbf{C}_L$ . We define the norm  $\|\mathbf{M}\|_2$  of a complex matrix by its spectral radius, i.e. the highest value of the matrix eigenvalues. By using the property  $\frac{1}{1-a} = 1 + a + a^2 + a^3 + \dots$ ,  $0 < a < 1$ , if  $0 < \|\mathbf{M}\|_2 < 1$ , we can expand vector  $\mathbf{x}_+$  as follows:

$$\mathbf{x}_+ = \left\{ \sum_{i=0}^{\infty} \mathbf{M}^i \right\} \mathbf{Z}_U^{-1}\mathbf{b}_+ = \sum_{i=0}^{\infty} \mathbf{y}_+^i$$

where  $\mathbf{y}_+^0 = \mathbf{Z}_U^{-1}\mathbf{b}_+$  and  $\mathbf{y}_+^i = \mathbf{M}\mathbf{y}_+^{i-1}$ ,  $i \geq 1$ . The expression of vector  $\mathbf{x}_+$  has a clear physical interpretation as the total unknown field corresponding to the sum of each scattered field contribution. Vector  $\mathbf{y}_+^i$ ,  $i = 1, 2, \dots$  corresponds to each scattered field contribution, and  $\mathbf{y}_+^0$  corresponds to the contribution of the direct reflection on the upper interface without refraction. Similarly, for the lower medium  $\Omega_2$ , the scattered information comes from  $\mathbf{x}_-$ ,  $\mathbf{x}_- = \mathbf{P}\mathbf{b}_+ = -\mathbf{Z}_L^{-1}\mathbf{C}_L\mathbf{x}_+$ . Scattered information from the lower medium can be expressed by that from upper field  $\mathbf{x}_+$ .

### 3.2.2 Simulation parameters of PILE

The simulation parameters have been chosen to represent the realistic thin pavement structures. Firstly, the air-coupled radar configuration at nadir has been selected for pavement survey at traffic speed. Second, the probing scope is limited to the first two layers of the pavement structure [15, 46]. The pavement structure is composed of two layers made up of an UTAS with mean thickness  $H = 20$  mm and the semi-infinite base layer, as shown in Fig. 3.1. Media  $\Omega_2$  and  $\Omega_3$  have different relative permittivities  $\epsilon_r$ , and are assumed to be homogeneous at normal incidence ( $\theta_i = 0$  degree in Fig. 3.1) for the GPR wavelengths within the frequency band [0.5; 10.5] GHz. For pavement materials, the permittivity  $\epsilon_r$  typically ranges within the intervals [4; 8], ac-

ording to [15]. The media are assumed to be lossless [29]. For the simulations, we take  $\epsilon_{r2} = 4.5$  and  $\epsilon_{r3} = 7$ , respectively.

The vertical profiles of the two rough interfaces  $\Sigma_A$  and  $\Sigma_B$  are assumed to obey a Gaussian PDF (probability density function) and an exponential autocorrelation function like in [15, 46, 47]. Then, the two roughness parameters of the surface  $\Sigma_A$  are the root means square (RMS) height  $\sigma_h$  and the correlation length  $L_c$ . They are within range [0.6; 1] mm and [5; 10] mm, respectively. For the interface  $\Sigma_B$ , larger values have been chosen for the latter parameters according to [15]. Table 3.1 illustrates the three cases which are considered in the simulations to study the sensitivity of the signal magnitude relatively to the roughness parameters. It is assumed that the antennas radiate a vertically polarized plane wave in far field at nadir. At 400 mm above the ground, the antenna footprint is between 300-500 mm wide. In the simulations, we consider that the rough surface is of length  $L = 2400$  mm and is illuminated by a Thorsos beam [48] with attenuation parameter  $g = L/8$  (the Thorsos beam has a Gaussian spatial distribution of the impinging field that mitigates the edge effects to negligible levels). The spatial sampling of the two rough interfaces is tailored to the inner wavelength according to  $\Delta x = |\lambda_2|/8$ , where  $\lambda_2$  is the wavelength inside  $\Omega_2$  with  $\lambda_2 = \lambda_0/\sqrt{\epsilon_{r2}}$  ( $\lambda_0$  is the wavelength in the air) and  $|\dots|$  is the modulus. In simulations, we take an incident wave with normal incidence ( $\theta_i = 0$ ), then calculate the first two backscattered echoes  $s_1$  and  $s_2$  from the scattered field,  $s_1 = E_1/E_i$  and  $s_2 = E_2/E_i$ , respectively. PILE method is performed at each frequency over the selected band [0.5; 10.5] GHz with sampling step  $\Delta f = 0.1$  GHz to get the frequency behaviour of the two primary backscattered echoes. Finally, for calculating the mean scattered field from the random rough interfaces, a Monte Carlo process which consists of 100 independent trials of the random rough surface generation is applied.

case #	Upper interface roughness ( $\Sigma_A$ ) $\sigma_{hA}, L_{cA}$	Lower interface roughness ( $\Sigma_B$ ) $\sigma_{hB}, L_{cB}$
<i>a</i>	(0.5, 6.4) mm	(1.0, 15) mm
<i>b</i>	(0.5, 6.4) mm	(2.0, 15) mm
<i>c</i>	(1.0, 6.4) mm	(2.0, 15) mm

Table 3.1: Roughness parameters (RMS height and correlation length) of both interfaces  $\Sigma_A$  and  $\Sigma_B$  to be used for the simulations

### 3.2.3 Simulation results

Firstly, following [15], we start the numerical simulations at a fixed radar frequency  $f$  to study the influence of the interface roughness on the backscattered echoes. The centre of frequency band,  $f = f_c = 5.5$  GHz, is studied. With 10000 realisations of the Monte-Carlo process, the histogram of the echoes  $s_1$  and  $s_2$  are computed. A comparison with the flat interface is also made. The following three figures (Figs. 3.2–3.4) give simulation results of computed histogram of  $s_1$  and  $s_2$  for 3 different cases. 4 sub-figures are plotted for each echo, which represent the histogram of the real part, the imaginary part, the amplitude and the phase (in degrees), respectively. The mean value is plotted in a dashed vertical line, and the mean value plus and minus the standard deviation are plotted in dotted vertical lines. The red line represents a Gaussian PDF having the same mean value and standard deviation as the data. Then, a comparison is made with the flat interface in green vertical line. Figs. 3.2–3.4 show that the histogram of the real part, imaginary part, amplitude and phase of backscattered echoes are close to Gaussian distributions. Concerning the imaginary part and the phase of the two echoes, there is a slight difference with the flat case. By contrast, a significant difference occurs in the real part and amplitude of the echoes: the roughness induces a decrease of the echoes (real part and amplitude) compared to the flat interface.

It is shown in Figs. 3.2–3.4 that the phase variations of both echoes are small compared to the magnitude variations, thus in the following we do not take the phase information into consideration [15, 46]. According to the previous section, PILE provides the amplitude of the two backscattered echoes  $s_1$  and  $s_2$  at each frequency over the frequency band  $[0.5; 10.5]$  GHz. As shown in Fig. 3.5, the interface roughness provides a continuous frequency decrease of the magnitude for both echoes  $s_1$  and  $s_2$ . The magnitude of echoes suffers more decrease with larger interface roughness (increasing RMS height). The magnitude of  $s_2$  is more sensitive to the lower interface roughness than to the surface roughness [15, 46]. For the influence of interface roughness, the frequency decrease of echo magnitude over the band  $[0.5, 10.5]$  GHz is given in the Table 3.2. As expected, it can be seen from Fig. 3.5 that if the RMS heights are the same, the backscattered echoes have the same frequency behaviour. In the following subsection, approximate expressions of the echo magnitude variations with respect to the frequency are derived from curve fittings. This parametrization allows to build a new data model which takes the interface roughness into account.

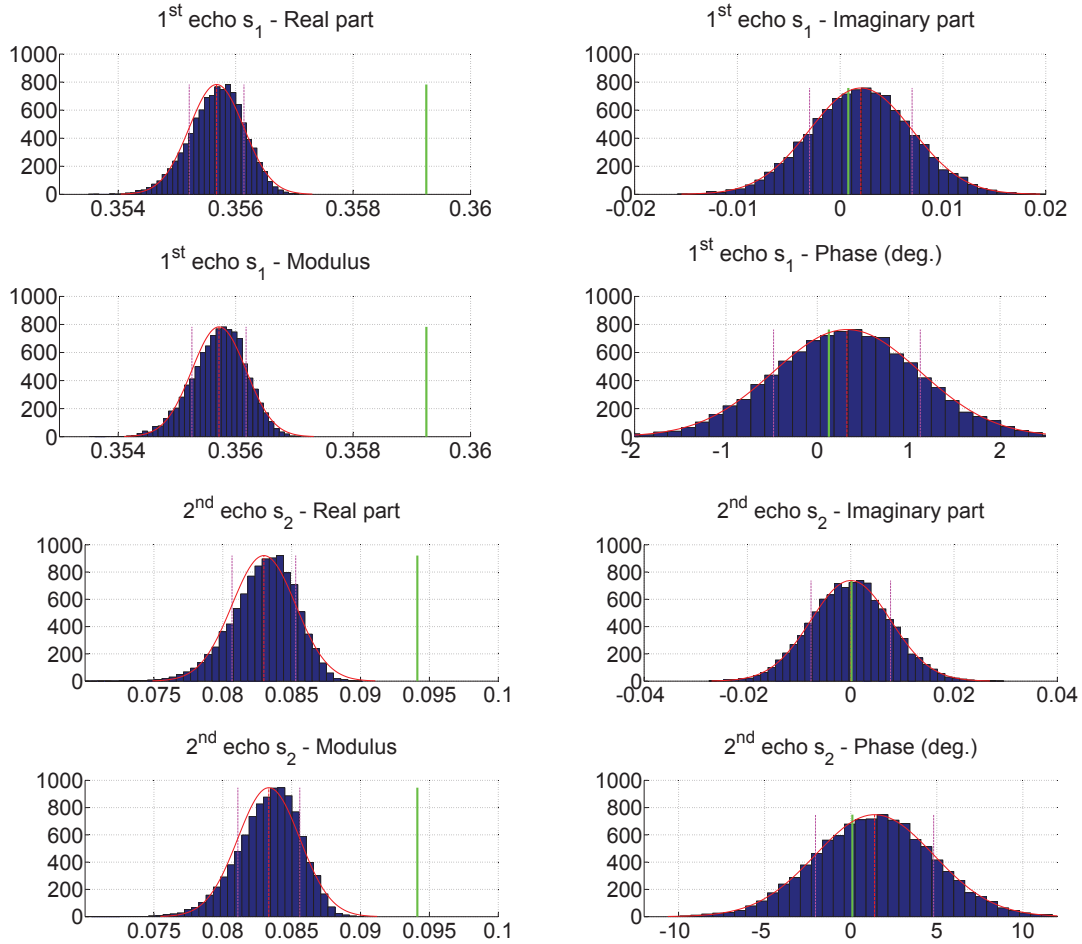


Figure 3.2: Case  $a$ : Histogram of the real part, imaginary part, amplitude and phase of the echoes with 10000 realisations with radar frequency  $f = 5.5$  GHz

Decrease (%)	Case			
		$a$	$b$	$c$
$s_k$				
	$s_1$	2.86	2.86	10.95
	$s_2$	36.49	82.30	83.32

Table 3.2: Variations of the echoes magnitude within the frequency band  $f \in [0.5; 10.5]$  GHz for a two layer stratified medium with three roughness scenarios (Decrease (%) =  $\frac{s_k(f_1) - s_k(f_N)}{s_k(f_1)} \times 100$ ,  $k = 1, 2$ ,  $f_1 = 0.5$  GHz,  $f_N = 10.5$  GHz)

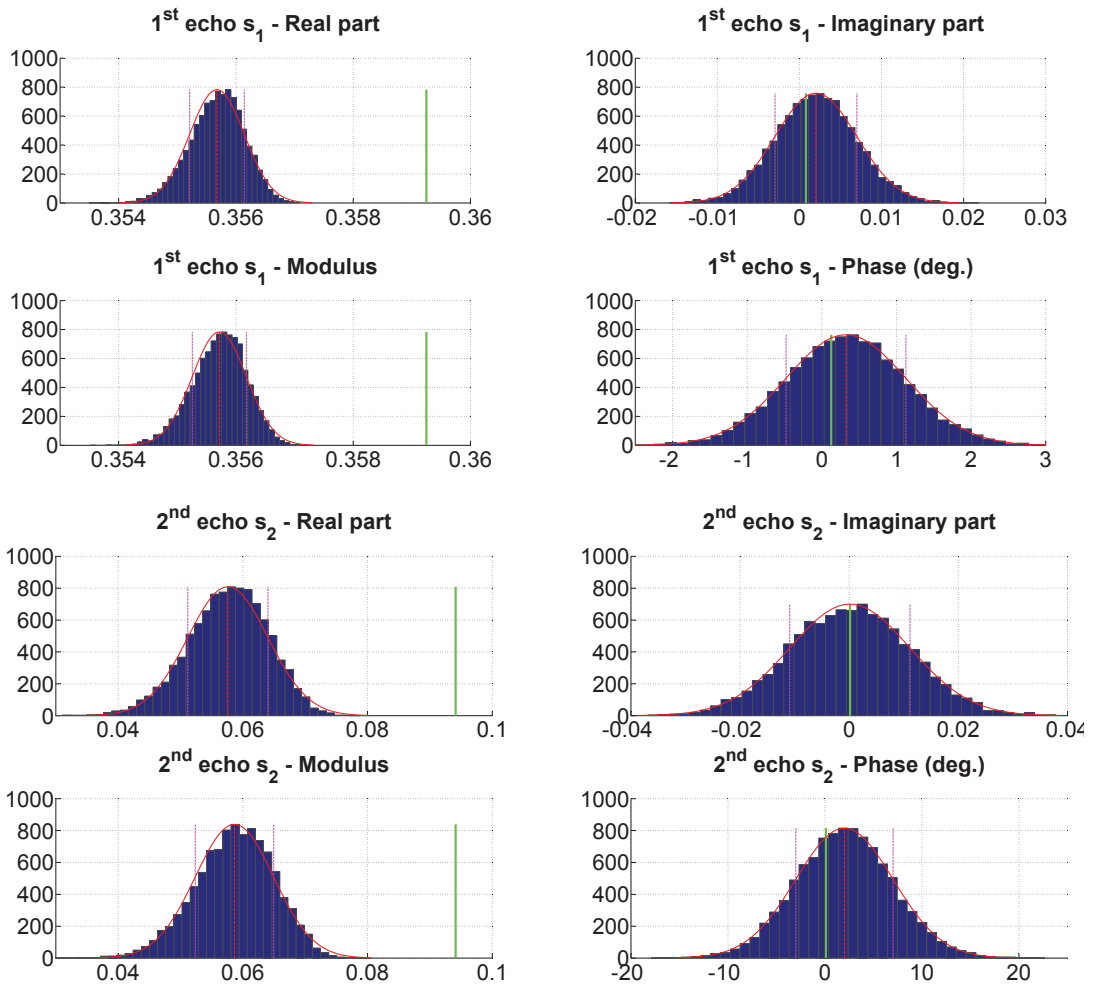


Figure 3.3: Case *b*: Histogram of the real part, imaginary part, amplitude and phase of the echoes with 10000 realisations with radar frequency  $f = 5.5$  GHz

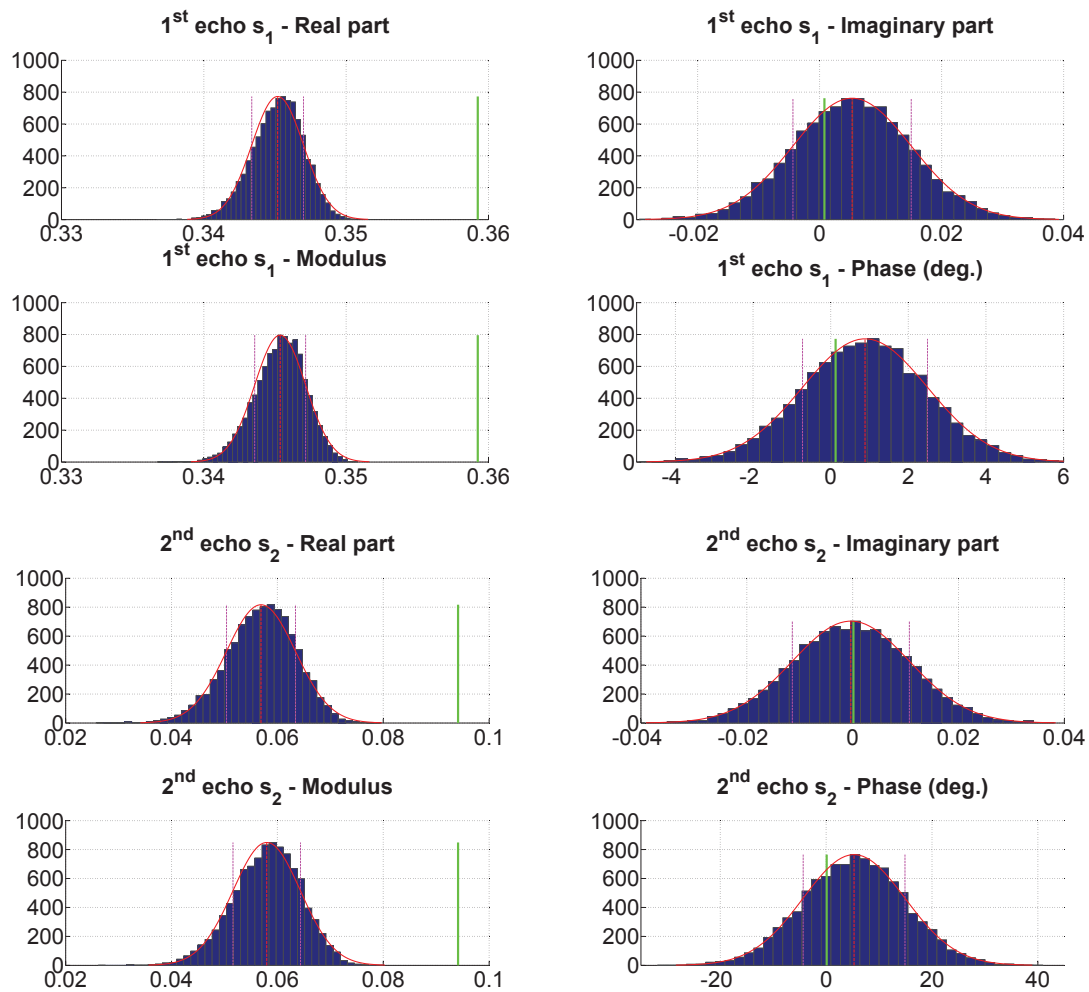


Figure 3.4: Case *c*: Histogram of the real part, imaginary part, amplitude and phase of the echoes with 10000 realisations with radar frequency  $f = 5.5$  GHz

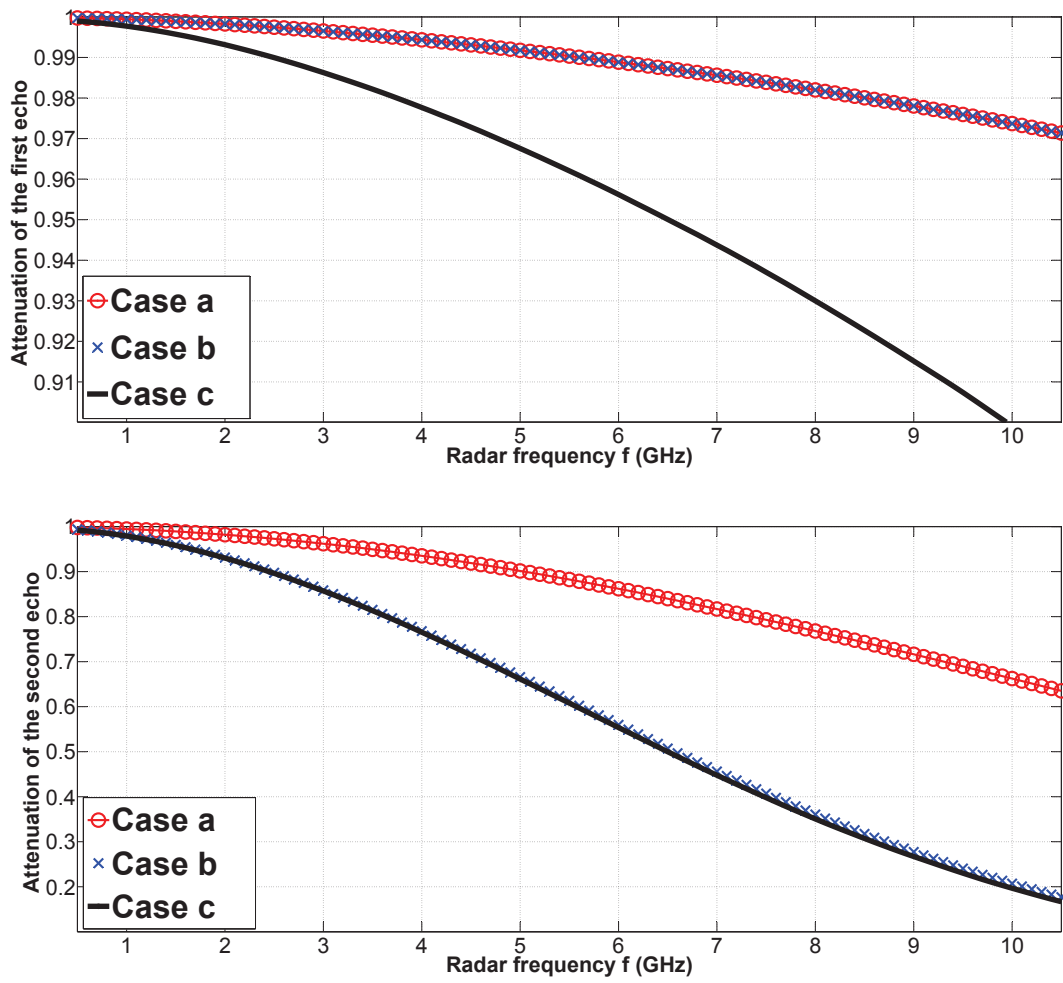


Figure 3.5: Frequency behaviour of the first two backscattered echoes  $s_1$  and  $s_2$  within the frequency band  $[0.5; 10.5]$  GHz for 3 different rough pavements with PILE method

### 3.3 Curve fitting

In order to characterise the frequency behaviour of backscattered echoes, curve fittings are made to estimate the parameters of the approximated expression of echoes. By using PILE method, the frequency behaviour of the first two scattered echoes is obtained. The next step is to deduce approximated expressions of the frequency behaviour of the two echoes, which can be used in the signal processing part.

The LMSE method is used to estimate the parameters of the approximated expression. The error associated with this method is expressed as follows:

$$R_{LMSE} = \sum_f |s_{k,data}(f) - s_{k,model}(f)|^2 \quad (3.4)$$

where  $s_{k,data}(f)$  is the frequency behaviour of the  $k$ th backscattered echoes computed from PILE,  $s_{k,model}(f)$  is the assumed expression of the frequency behaviour of the  $k$ th echo. To find the best solution to model the frequency behaviour of echo amplitude, several conditions (different approximated expressions and different frequency bands) are considered. In the following, we choose three different forms of the backscattered echo amplitudes:

1. The exponential shape  $|s(f)| = s_k \times \exp(-bf)$  with unknown parameter  $b$ ;
2. The Gaussian shape  $|s(f)| = s_k \times \exp(-bf^2)$  with unknown parameter  $b$ ;
3. The mixed shape  $|s(f)| = s_k \times \exp(-bf^2 - cf)$  with unknown parameters  $b$  and  $c$ .

In these approximated expressions,  $s_k$  is the amplitude of considered backscattered echo for the flat pavement. Curve fittings are carried out with radar data in narrow bands, middle bands and large bands. In the following, only case  $c$  (with  $\sigma_{hA} = 1.0$  mm,  $\sigma_{hB} = 2.0$  mm) is studied, and the curve fitting results of cases  $a$  and  $b$  are shown in Appendix A.

#### 3.3.1 Curve fitting results in narrow band

For narrowband frequency, 4 cases are studied: the frequency bands  $f \in [0.5; 1.5]$  GHz,  $f \in [0.5; 2.5]$  GHz,  $f \in [1; 3]$  GHz, and  $f \in [0.5; 3.5]$  GHz. Figs. 3.6 and 3.7 present the fitting results in different narrow bands. In addition, in order to evaluate the fitting performance, Table 3.3 gives the Root-Mean-Square Error (RMSE) of the curve fitting:

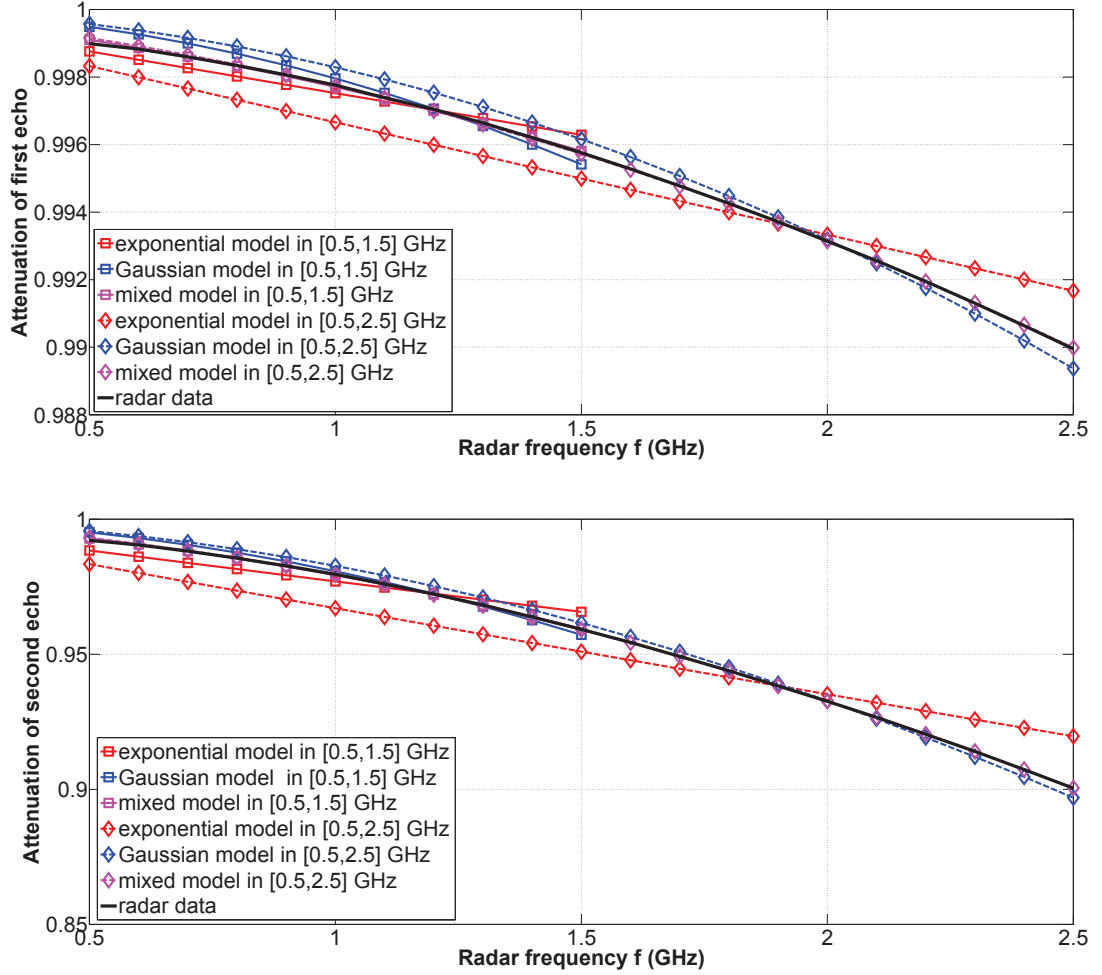


Figure 3.6: Curve fittings for  $f \in [0.5; 1.5]$  GHz and  $f \in [0.5; 2.5]$  GHz

Table 3.3: Curve fittings results in narrow band

RMSE % ( $s_1/s_2$ )	Model	Frequency		
		$ s(f)  = s_k \times \exp(-bf)$	$ s(f)  = s_k \times \exp(-bf^2)$	$ s(f)  = s_k \times \exp(-bf^2 - cf)$
[0.5, 1.5] GHz		0.0290/0.371	0.0307/0.179	$4.70 \times 10^{-3}$ /0.0284
[0.5, 2.5] GHz		0.0906/1.04	0.0433/0.257	$4.97 \times 10^{-3}$ /0.0369
[1.0, 3.0] GHz		0.130/1.46	0.0485/0.273	$1.49 \times 10^{-3}$ / $9.57 \times 10^{-3}$
[0.5, 3.5] GHz		0.171/1.94	0.0605/0.324	$4.59 \times 10^{-3}$ /0.0282

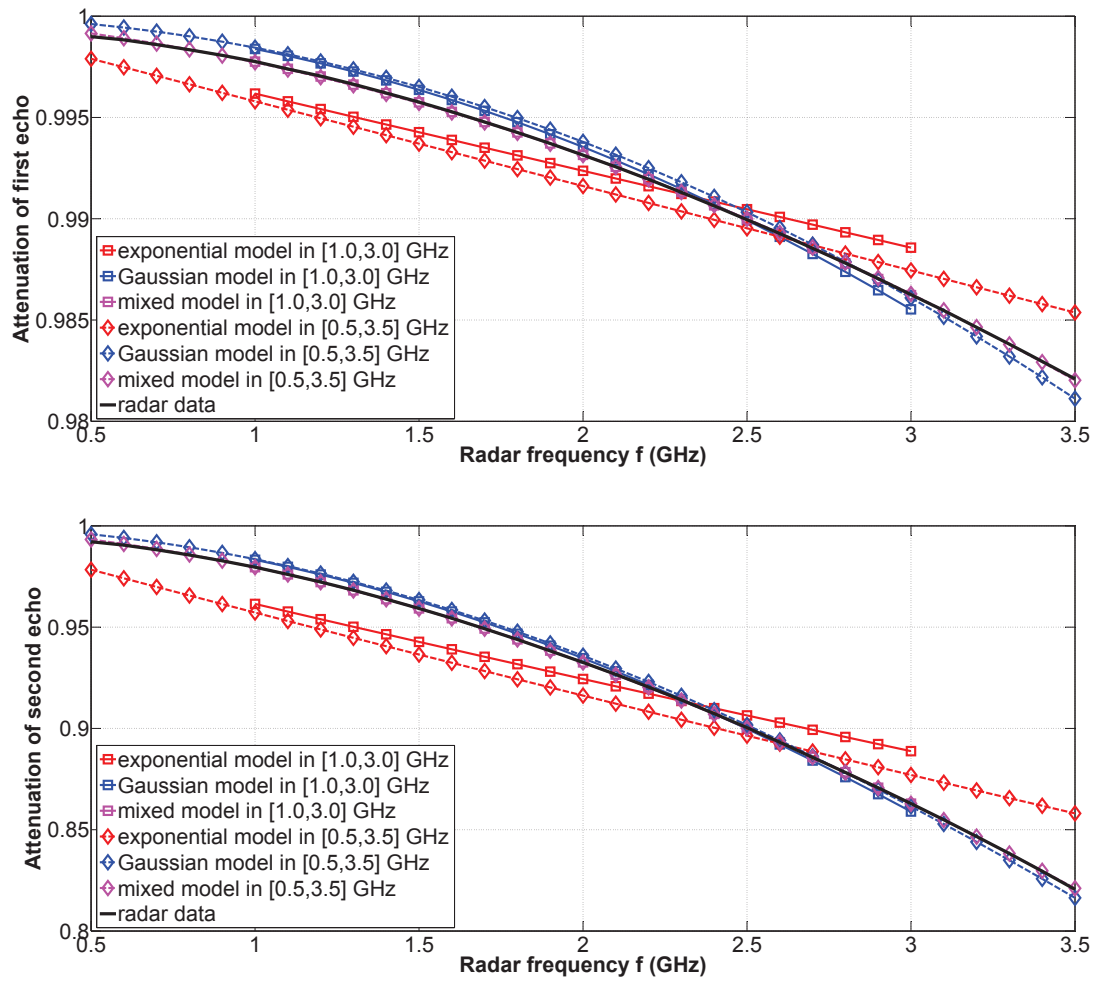


Figure 3.7: Curve fittings for  $f \in [1.0; 3.0]$  GHz and  $f \in [0.5; 3.5]$  GHz

$$RMSE = \sqrt{\frac{\sum_{i=1}^N (\bar{x}_i - x_i)^2}{N}}$$

where  $N$  is the number of sampling points,  $\bar{x}_i$  the fitting value at the  $i$ th sample point, and  $x_i$  the true value at the  $i$ th sample point. In narrow bands, the three models perfectly match the PILE data. The results are shown in Table 3.3. They highlight that the mixed model has the smallest RMSE. For the Gaussian model, only slight differences between the Gaussian model and the PILE data can be observed in the lower frequencies. The performance of the exponential model gets worse with increasing frequency band; nevertheless, it can be accepted for a frequency bandwidth up to 2 GHz.

### 3.3.2 Curve fitting results in middle band

For the curve fitting in middle frequency bands, we select two cases:  $f \in [0.5; 4.5]$  GHz and  $f \in [0.5; 6.5]$  GHz. Fig. 3.8 shows the fitting results in the two middle bands, and the curve fitting errors are calculated in Table 3.4.

Table 3.4: Curve fittings results in middle band

RMSE % ( $s_1/s_2$ ) \ Model	$ s(f)  = s_k \times \exp(-bf)$	$ s(f)  = s_k \times \exp(-bf^2)$	$ s(f)  = s_k \times \exp(-bf^2 - cf)$
Frequency			
[0.5, 4.5] GHz	0.261/3.07	0.0890 /0.348	0.0136 /0.0600
[0.5, 6.5] GHz	0.463/5.63	0.00170/0.346	0.0347/0.108

From the curve fitting results, we observe that the mixed model remains in excellent agreement with PILE data. Meanwhile, for the Gaussian model, the curve fittings also have a general good agreement with PILE data. However, for the performance of the exponential model, substantial deviations have been found. These results are not surprising as recent work [46] showed that the Ament model, which has a Gaussian frequency variation shape, is a valid asymptotic electromagnetic model for describing the backscattered echoes.

### 3.3.3 Curve fitting results in large band

In large frequency bands, we make curve fittings in two frequency bands:  $f \in [0.5; 8.5]$  GHz and  $f \in [0.5; 10.5]$  GHz. The curve fitting results and errors are shown in Fig. 3.9 and Table 3.5, respectively.

The performance of these three models is similar to that for the middle bands. The mixed model and Gaussian model show general good agreement in the large frequency

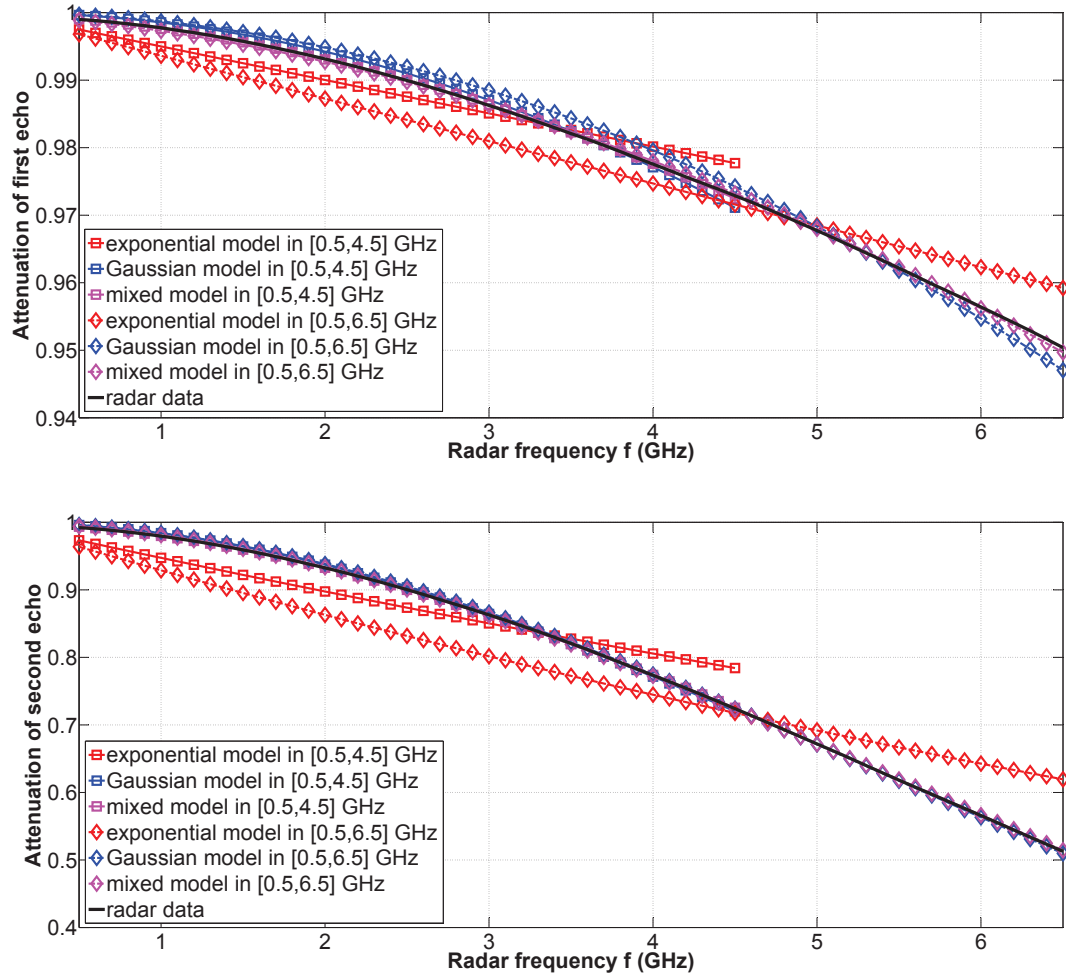
Figure 3.8: Curve fittings in  $f \in [0.5; 4.5]$  GHz and  $f \in [0.5; 6.5]$  GHz

Table 3.5: Curve fittings results in large band

RMSE % ( $s_1/s_2$ )	Model	$ s(f)  = s_k \times \exp(-bf)$	$ s(f)  = s_k \times \exp(-bf^2)$	$ s(f)  = s_k \times \exp(-bf^2 - cf)$	
		Frequency			
		[0.5, 8.5] GHz	0.698/7.99	0.270/0.355	0.0562/0.103
		[0.5, 10.5] GHz	0.983/9.88	0.367/0.323	0.0669/0.166

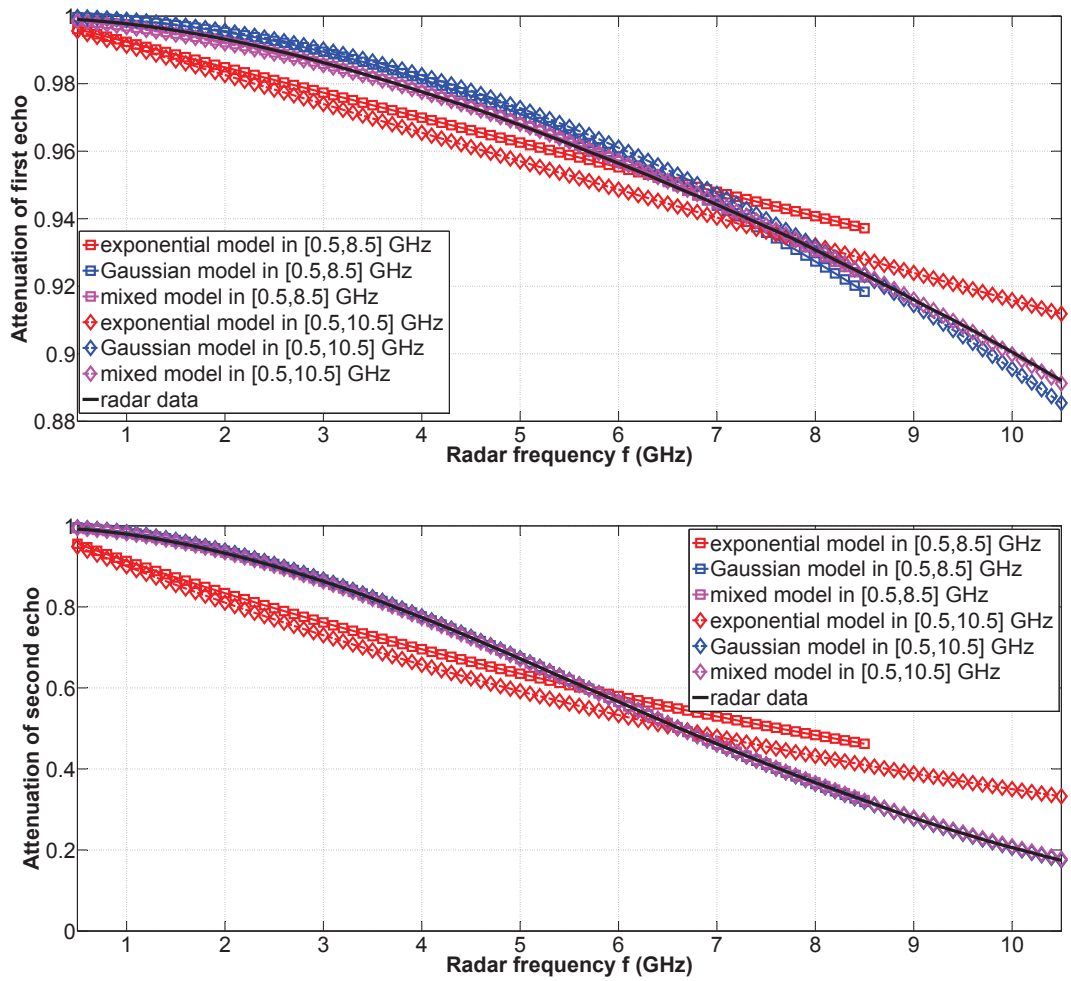


Figure 3.9: Curve fittings in  $f \in [0.5; 8.5]$  GHz and  $f \in [0.5; 10.5]$  GHz

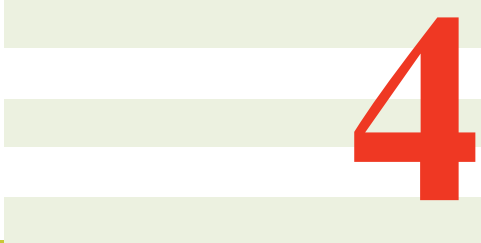
bands. Only slight differences appear in the first echo of the Gaussian model. For the exponential model, important differences appear in the large frequency bands.

Thus, the mixed model and Gaussian model have a good match with PILE data in narrow, middle and large bands. However, the curve fitting of echoes also has a general good agreement with PILE data in the whole frequency range. The exponential model shows poor performances in these three different conditions except for the frequency band is smaller than 2 GHz.

### 3.4 Conclusion

In this chapter, we have presented the impact of interface roughness on the frequency behaviour of backscattered echoes for different bandwidths (narrow, middle and large bands) by using PILE method. It has been shown that the interface roughness introduces some notable frequency variations of the magnitude of the backscattered echoes, which may degrade the performance of classical time delay processing techniques.

In order to study the frequency variations of the magnitude of the backscattered echoes with interface roughness, curve fittings have been made to estimate the parameters of the approximated expression of the echoes. The parameter called roughness parameter accounting for the frequency variations (by assuming an exponential shape, a Gaussian shape or a mixed shape) is estimated by curve fitting. We propose 3 different signal models which take the interface roughness into account. In the following chapters, new signal processing methods are proposed to deal with these new signal models. In Chapter 4, new algorithms are proposed for the exponential model. In Chapter 5, the Gaussian and mixed models are studied and new algorithms are presented.



# 4

---

## Parameter estimation for exponential model

In the previous chapter, the influence of interface roughness has been addressed. In the literature, when the interface roughness is taken into account, it is often used to analyse the errors coming from the roughness [15, 16]. In this chapter, we take the interface roughness into account in the signal model and focus on the estimation of time delays and interface roughness. New signal processing algorithms are proposed in this chapter in order to jointly estimate the time delay and a new parameter: the roughness parameter (the roughness of the interfaces). The proposed algorithms can estimate different parameters of the stratified medium (the roughness of the interfaces as well as the thickness of the layers). These estimations will make it possible to detect and evaluate damaged zones (interface debonding of pavements and seal coats of bridges).

It has been established in Chapter 3 that the frequency decrease of the echo magnitude can be approximated in narrow frequency band (less than 2 GHz) by an exponential function  $w_k(f_i) \approx \exp(-b_k f_i)$ , with  $b_k$  as the roughness parameter of the  $k$ th interface. This enables a simple parametrization of the frequency variations for data modelling. To jointly estimate the time delays and roughness parameters, high resolution methods (subspace methods) are presented. In this chapter, we propose 4 algorithms: a modified 2-D MUSIC, a modified root-MUSIC, a modified matrix pen-

cil method (MPM) and TDRP-ESPRIT. The performance of the proposed algorithms is tested on the data simulated from PILE method [15, 44, 49]. The simulations will provide the performance analysis on the proposed methods with respect to the time-delays, the roughness parameters, the thicknesses and the permittivities.

This chapter is organized as follows: section 2 presents the radar data model and the preprocessing method SSP which is used to mitigate the influence of the correlation magnitude between the backscattered echoes. In section 3, we present the modified 2-D MUSIC, the modified root-MUSIC, the modified MPM and TDRP-ESPRIT to estimate the time delays and roughness parameters. In addition, the permittivity of layers can be estimated from known time delays. Simulation results and discussions on the performance of the proposed algorithms are provided in section 4.

## 4.1 Signal model

### 4.1.1 Signal model in the whole band

The previous chapter has shown that the frequency behaviour of the backscattered echoes of rough interfaces can be obtained [47]. Here, we focus on the first two or three top layers of the roadway, which are low-loss media. For pavement materials, the conductivity typically ranges within the interval  $[10^{-3}; 10^{-2}]$  S/m, according to the data provided in [4]. Thus, the media can be considered as a low-loss media. In addition, for the flat surface, according to the work in [29], if the surface medium is slightly lossy, the dispersivity of the medium can be neglected. As a consequence, the echoes are simply time-shifted and attenuated copies of the transmitted signal, as mentioned in [6, 10, 12, 13, 23, 30, 50]. On the same basis, we present a new signal model taking the interface roughness into account but without considering the conductivity (for the low-loss media, the dispersivity of medium can be neglected). The new signal model can be written as:

$$r(f_i) = \sum_{k=1}^d e(f_i) s_k w_k(f_i) \exp(-j2\pi f_i t_k) + n(f_i) \quad (4.1)$$

where  $d$  is the number of interfaces,  $e(f_i)$  the radar pulse in the frequency domain,  $s_k$  the reflection coefficient of the  $k$ th scattered echo with flat interfaces and by assuming the media to be lossless, which implies that  $s_k$  is independent of  $f_i$ .  $n(f_i)$  is an additive white Gaussian noise with zero mean and variance  $\sigma^2$ .  $w_k(f_i)$  represents the frequency behaviour of the  $k$ th scattered echo at the frequency  $f_i = f_1 + (i - 1)\Delta f$ , with  $i =$

$1, 2 \dots N$ ,  $N$  being the number of used frequencies,  $f_1$  the lowest frequency of the studied frequency band and  $\Delta f$  the frequency shift. From the previous chapter and [47],  $w_k(f_i) = \exp(-b_k f_i)$  is assumed to be dependent on the interface roughness through the parameter  $b_k$ . Eq. (4.1) can be written in the following vector form:

$$\mathbf{r} = \mathbf{\Lambda} \mathbf{A} \mathbf{s} + \mathbf{n} \quad (4.2)$$

with the following notation definitions:

1.  $\mathbf{r} = [r(f_1) \ r(f_2) \ \dots \ r(f_N)]^T$  is the  $(N \times 1)$  received signal vector, called observation vector, which may represent either the Fourier transform of the measured GPR signal or the measurements by a step-frequency radar;
2.  $\mathbf{\Lambda} = \text{diag}(e(f_1), e(f_2), \dots, e(f_N))$  is a  $(N \times N)$  diagonal matrix, whose diagonal elements are the Fourier transform  $e(f)$  of the radar pulse;
3.  $\mathbf{A} = [\mathbf{a}(t_1, b_1) \ \mathbf{a}(t_2, b_2) \ \dots \ \mathbf{a}(t_d, b_d)]$  is called the  $(N \times d)$  mode matrix;
4.  $\mathbf{a}(t_k, b_k) = [e^{-2j\pi f_1 t_k - b_k f_1} \ e^{-2j\pi f_2 t_k - b_k f_2} \ \dots \ e^{-2j\pi f_N t_k - b_k f_N}]^T$  is the mode vector;
5.  $\mathbf{s} = [s_1 \ s_2 \ \dots \ s_d]^T$  is the  $(d \times 1)$  vector of echoes amplitudes in the case of flat interfaces and lossless media;
6.  $\mathbf{n} = [n(f_1) \ n(f_2) \ \dots \ n(f_N)]^T$  is the  $(N \times 1)$  noise vector, in which each element is a white Gaussian noise with zero mean and variance  $\sigma^2$ .

According to the signal model (4.2) and by assuming the noise to be independent of the echoes, the covariance matrix  $\mathbf{Y}_0$  of  $\mathbf{r}$  can be written as:

$$\begin{aligned} \mathbf{Y}_0 &= E(\mathbf{r}\mathbf{r}^H) = \mathbf{\Lambda} \mathbf{A} E(\mathbf{s}\mathbf{s}^H) \mathbf{A}^H \mathbf{\Lambda}^H + E(\mathbf{n}\mathbf{n}^H) \\ &= \mathbf{\Lambda} \mathbf{A} \mathbf{S} \mathbf{A}^H \mathbf{\Lambda}^H + \sigma^2 \mathbf{I} \end{aligned} \quad (4.3)$$

where  $\mathbf{S}$  is the  $(d \times d)$  dimensional covariance matrix of vector  $\mathbf{s}$ . In the following, the data is divided by the pulse as follows:

$$\mathbf{r}' = \mathbf{A} \mathbf{s} + \mathbf{\Lambda}^{-1} \mathbf{n} = \mathbf{A} \mathbf{s} + \mathbf{b} \quad (4.4)$$

where vector  $\mathbf{n}'$  is the new noise vector after the data are divided by the pulse. Thus, the modified covariance matrix can be written as:

$$\begin{aligned} \mathbf{R}_0 &= E(\mathbf{r}'\mathbf{r}'^H) = \mathbf{\Lambda}^{-1} \mathbf{Y}_0 \mathbf{\Lambda}^{-H} = \mathbf{A} \mathbf{S} \mathbf{A}^H + \sigma^2 \mathbf{\Lambda}^{-1} \mathbf{\Lambda}^{-H} \\ &= \mathbf{A} \mathbf{S} \mathbf{A}^H + \sigma^2 \mathbf{\Sigma} \end{aligned} \quad (4.5)$$

with

$$\mathbf{\Sigma} = \mathbf{\Lambda}^{-1} \mathbf{\Lambda}^{-H} = \text{diag}\left(\frac{1}{|e(f_1)|^2}, \frac{1}{|e(f_2)|^2}, \dots, \frac{1}{|e(f_N)|^2}\right) \quad (4.6)$$

### 4.1.2 Spatial smoothing preprocessing technique

As shown in section 2.4, in practice, the backscattered echoes come from the same Tx source but with different paths. Thus, the cross-correlation between the echoes may be high enough to degrade the performance of high resolution methods. Thus, it is necessary to mitigate the influence of the cross-correlation magnitude by a sub-band averaging preprocessing. In this chapter, only the SSP [32], which has been introduced in Chapter 2, is considered in this section. The other methods can not be used (they are difficult to be adapted to the new signal model).

When the interface roughness is taken into account, matrix  $\mathbf{D}$  which is defined in Eq.(2.10) should be rewritten with the new signal model.  $\mathbf{D}$  can be expressed as:

$$\mathbf{D} = \text{diag}\left(e^{-(2j\pi t_1 + b_1)\Delta f}, \dots, e^{-(2j\pi t_d + b_d)\Delta f}\right) \quad (4.7)$$

The data covariance matrix  $\mathbf{R}_{k0}$  of the  $k$ th sub-band is written as follows:

$$\mathbf{R}_{k0} = E(\mathbf{r}'_k \mathbf{r}'_k{}^H) \quad (4.8)$$

$$\mathbf{R}_{k0} = \mathbf{A}_L \mathbf{D}^{k-1} \mathbf{S} (\mathbf{D}^{k-1})^H \mathbf{A}_L^H + \sigma^2 \mathbf{\Sigma}_k \quad (4.9)$$

where  $\mathbf{\Sigma}_k$  is the  $k$ th noise sub-band matrix of  $\mathbf{\Sigma}$ .

As the radar pulse is known, and the noise variance  $\sigma^2$  is estimated (by EVM or PM from Chapter 2). Then, the  $k$ th sub-band of the new noise-free covariance matrix can be written as follows:

$$\mathbf{R}_k = \mathbf{R}_{k0} - \hat{\sigma}^2 \mathbf{\Sigma}_k \approx \mathbf{A}_L \mathbf{D}^{k-1} \mathbf{S} (\mathbf{D}^{k-1})^H \mathbf{A}_L^H \quad (4.10)$$

where  $\hat{\sigma}^2$  is the estimated noise variance. The SSP estimates the modified covariance matrix  $\mathbf{R}_{SSP}$  as the averaging over  $M$  frequency overlapping sub-bands as follows:

$$\mathbf{R}_{SSP} = \frac{1}{M} \sum_{k=1}^M \mathbf{R}_{k0} \quad (4.11)$$

$$\mathbf{R}_{SSP} = \mathbf{A}_L \left[ \frac{1}{M} \sum_{k=1}^M \mathbf{D}^{k-1} \mathbf{S} (\mathbf{D}^{k-1})^H \right] \mathbf{A}_L^H + \sigma^2 \mathbf{\Sigma}_o \quad (4.12)$$

where  $\Sigma_o = \frac{1}{M} \sum_{k=1}^M \Sigma_k$ .

After taking PM into consideration, the modified covariance matrix is as follows:

$$\begin{aligned} \mathbf{R}_{SSP-PM} &= \frac{1}{M} \sum_{k=1}^M \mathbf{R}_k \approx \mathbf{A}_L \left[ \frac{1}{M} \sum_{k=1}^M \mathbf{D}^{k-1} \mathbf{S} (\mathbf{D}^{k-1})^H \right] \mathbf{A}_L^H \\ &= \mathbf{A}_L \bar{\mathbf{S}} \mathbf{A}_L^H \end{aligned} \quad (4.13)$$

The effective correlation coefficient between the  $i$ th and  $j$ th echoes after the SSP can be expressed as:

$$\rho_{SSP} = \frac{\sin(M\pi\Delta f(t_j - t_i))}{M \sin(\pi\Delta f(t_j - t_i))} \exp(-j(M-1)\pi\Delta f(t_j - t_i)) \exp((M-1)(-b_j - b_i)) \quad (4.14)$$

where  $t_i$  and  $t_j$ ,  $b_i$  and  $b_j$  are the time delays and roughness parameters of  $i$ th and  $j$ th echoes, respectively, and  $M$  is number of overlapping sub-bands. In this case, the roughness parameter is also embedded in the effective correlation coefficient. As a result, Fig. 4.1 shows the ability of SSP to reduce the magnitude of the correlation coefficient between echoes with regards to the number of sub-bands. For the parameters at hand, the influence of interface roughness is found to be slight on the correlation magnitude for the SSP.

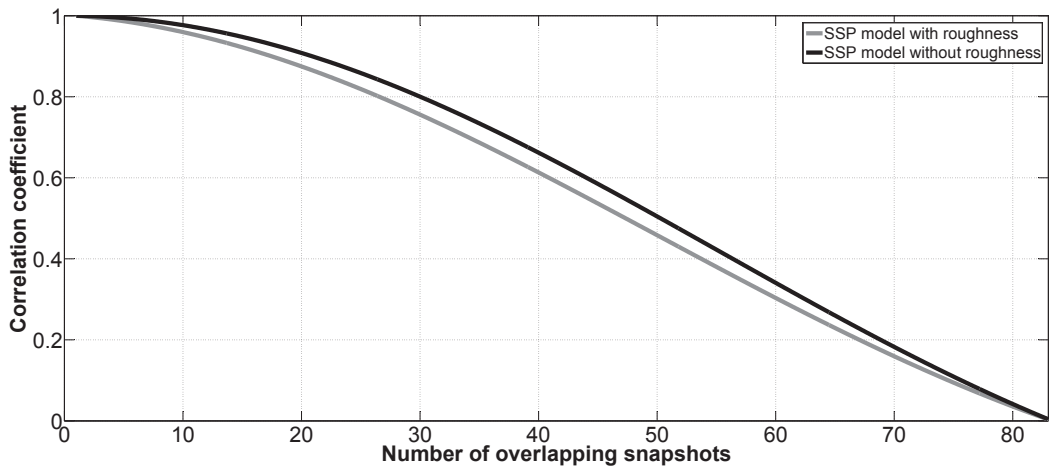


Figure 4.1: Effective correlation for SSP with the following parameters:  $N = 101$ ,  $f_1 = 1.0$  GHz,  $\Delta f = 0.02$  GHz,  $b_1 = 3.83 \times 10^{-12}$ ,  $b_2 = 3.93 \times 10^{-11}$ ,  $t_1 = 1$  ns,  $t_2 = 1.3$  ns.

## 4.2 Subspace methods

In this section, we present 4 subspace methods (the modified 2-D MUSIC, the modified root-MUSIC, the modified MPM and TDRP-ESPRIT) which are extended to jointly estimate the time delays and roughness parameters.

### 4.2.1 Modified two-dimensional MUSIC

To estimate two different parameters, a modified 2-D MUSIC algorithm is proposed. Like classical MUSIC algorithm, 2-D MUSIC algorithm uses the principle of orthogonality between the source directional vectors and the noise subspace. 2-D MUSIC extends MUSIC into 2 dimensions. The covariance matrix after preprocessing SSP and PM can be written as Eq. (4.13). Modified 2-D MUSIC allows us to jointly estimate both the time delays and the roughness parameters by searching the peaks of following equation:

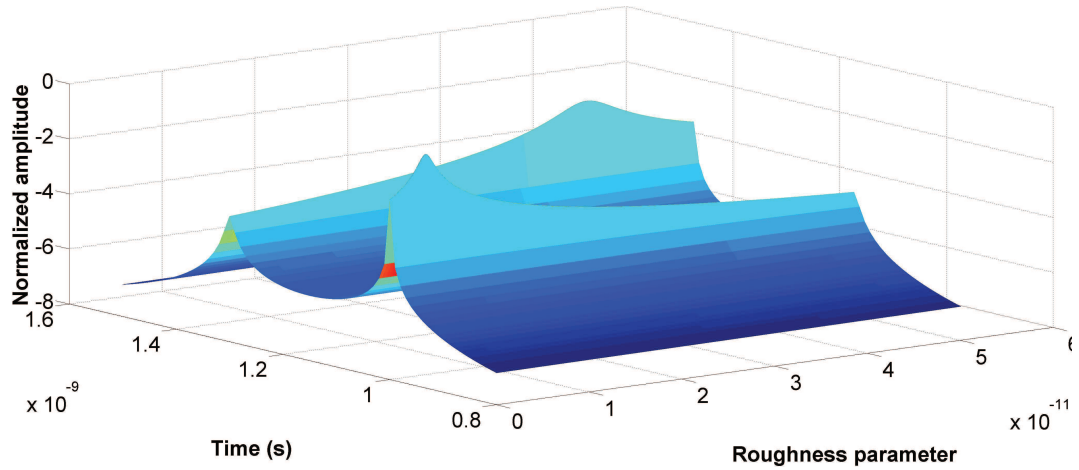
$$P_{MU} = \frac{\mathbf{a}^H(t, b)\mathbf{a}(t, b)}{\mathbf{a}^H(t, b)\mathbf{U}_N\mathbf{U}_N^H\mathbf{a}(t, b)} \quad (4.15)$$

where  $\mathbf{a}(t, b) = [e^{-2j\pi f_1 t - b f_1} \ e^{-2j\pi f_2 t - b f_2} \ \dots \ e^{-2j\pi f_L t - b f_L}]^T$ ,  $\mathbf{U}_N$  being the  $L \times (L - d)$  noise matrix whose columns are the  $L - d$  noise eigenvectors. The advantage of 2-D MUSIC is that it is easy to be applied for parameters estimation. However, the algorithm greatly increases the computational complexity.

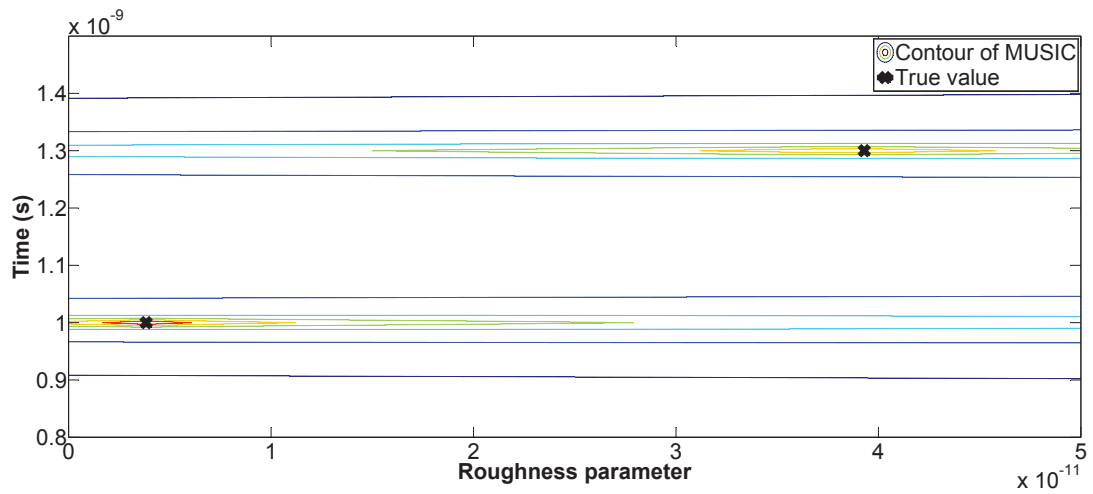
Fig. 4.2 presents an example of the modified 2-D MUSIC (the pseudo-spectrum and the contour) with SSP. By searching the peak positions, the time delays and roughness parameters are estimated. The estimated roughness parameters  $\hat{b}_1 = 3.86 \times 10^{-12}$  and  $\hat{b}_2 = 3.85 \times 10^{-11}$ , which corresponds to small errors (0.78% and 2.03%) in comparison with the true values.

### 4.2.2 Modified root-MUSIC

The main drawback of the modified 2-D MUSIC is that it need for searching the spectrum of both the time delays and roughness parameters, which greatly increases the computational complexity. Thus, in order to reduce the complexity, a modified root-MUSIC algorithm has been proposed by [22] enables the time delay estimation of backscattered echoes, whose the magnitudes are frequency dependent. This algorithm is applied in this subsection to jointly estimate the time delays and the interface roughness parameters. According to [22], we modify the data covariance matrix in (4.13).



(a) Pseudo-spectrum of 2-D MUSIC



(b) Contour of 2-D MUSIC

Figure 4.2: Simulation example on the modified 2-D MUSIC with the following parameters:  $N = 51, L = 31, f_1 = 1.0$  GHz,  $f_N = 3.0$  GHz,  $\Delta f = 0.04$  GHz,  $b_1 = 3.83 \times 10^{-12}$ ,  $b_2 = 3.93 \times 10^{-11}$ ,  $t_1 = 1$  ns,  $t_2 = 1.3$  ns, SNR = 30 dB for 2 backscattered echoes

After some normalization, the modified data covariance matrix  $\bar{\mathbf{R}}$  can be written as:

$$\bar{\mathbf{R}} = \mathbf{W}\mathbf{A}_L\bar{\mathbf{S}}\mathbf{A}_L^H\mathbf{W} = \bar{\mathbf{A}}_L\bar{\mathbf{S}}\bar{\mathbf{A}}_L^H \quad (4.16)$$

where

- $\mathbf{W} = \text{diag}\{\exp(bf_1), \exp(bf_2), \dots, \exp(bf_L)\}$ , where the detail of  $b$  is given in the following paragraph;
- $\bar{\mathbf{A}}_L = [\mathbf{a}'(t_1, b_1) \ \mathbf{a}'(t_2, b_2) \ \dots \ \mathbf{a}'(t_d, b_d)]$ ;
- $\mathbf{a}'(t_k, b_k) = [\exp(-j2\pi f_1 t_k) \exp(-b_k f_1 + b f_1) \ \dots \ \exp(-j2\pi f_L t_k) \exp(-b_k f_L + b f_L)]^T$ .

Defining the roots of the root-MUSIC polynomial (RMP) which correspond to the  $k$ th backscattered echoes  $x_k = \exp(-j2\pi\Delta f t + b\Delta f - b_k\Delta f)$ , the model vector  $\mathbf{a}'(t_k, b_k)$  becomes  $\mathbf{a}'(x_k) = \exp(-2j\pi f_1 t + b f_1 - b_k f_1) [1 \ x_k \ \dots \ x_k^{L-1}]^T$ . Then the root-MUSIC polynomial (RMP) can be written as:

$$P(x_k) = \mathbf{a}'^H(x_k)\mathbf{U}_N\mathbf{U}_N^H\mathbf{a}'(x_k) = \mathbf{a}'^T(x_k^*)\mathbf{U}_N\mathbf{U}_N^H\mathbf{a}'(x_k) = 0 \quad (4.17)$$

where  $\mathbf{U}_N$  is the  $L \times (L - d)$  noise matrix whose columns are the  $L - d$  noise eigenvectors; the roots of RMP are approximately in conjugate reciprocal pairs. We should notice that when  $b = b_k$ ,  $k = 1, 2, \dots, d$ , the roots of the  $k$ th backscattered echoes appear in conjugate reciprocal pairs on the unit circle of the complex plane; as the value  $b$  varies, each root-pair of backscattered echo also moves in the complex plane. Therefore, the roughness parameter of each backscattered echo is determined when the root pair is closest to the unit circle with the change of  $b$ , which corresponds to finding the minimum of the root-pair separation of the group, according to [22]. The time delays of the echoes are then determined from the phase of the roots.

An example is shown in Fig. 4.3 which plots the distance variance between the root-pairs of RMP with respect to the roughness parameter  $b$ . The latter parameter is estimated from the minimum of the root-pair distance. The roughness parameters estimated by root-MUSIC are  $\hat{b}_1 = 3.93 \times 10^{-12}$  and  $\hat{b}_2 = 3.98 \times 10^{-11}$ , with errors 2.61% and 1.27%, respectively.

### 4.2.3 Matrix pencil method

MPM [51] has been developed from a generalized idea of Pencil-of-Function method. It can be adapted to estimate the time delays and roughness parameters. We rewrite the mode vector  $\mathbf{a}(t_k, b_k) = z_{k0}[1, z_k, z_k^2, \dots, z_k^{N-1}]^T$ ,  $z_k = \exp(-j2\pi\Delta f t_k - b_k\Delta f)$

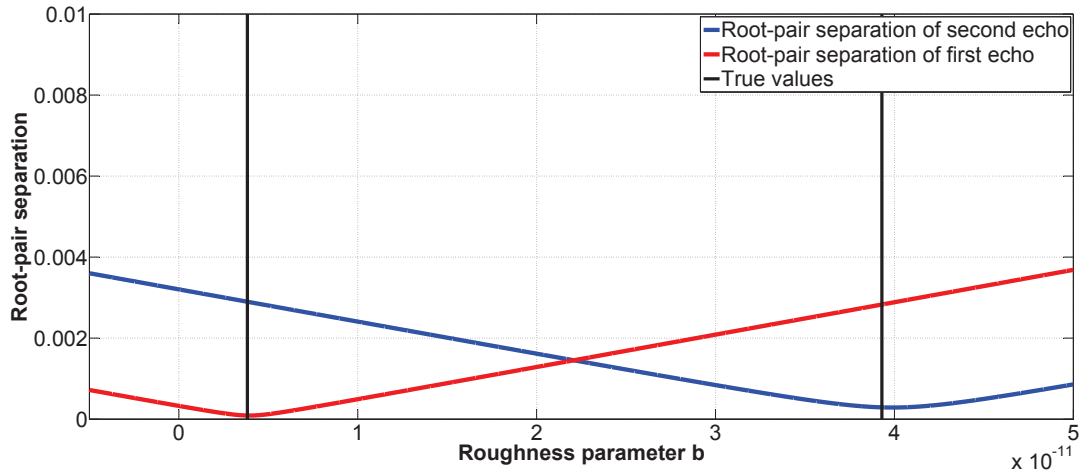


Figure 4.3: Root-pair separation of the modified root-MUSIC polynomial versus the roughness parameter – same simulation parameters as in Fig. 4.2

and  $z_{k0} = \exp(-j2\pi f_1 t_k - b_k f_1)$ . In the first step, we deal with the noiseless received signal vector in Eq. 4.4, defined as  $\mathbf{r}' = \mathbf{x} + \mathbf{b}$ , with  $\mathbf{x} = \mathbf{A}\mathbf{s}$ . To motivate the MPM, a Hankel data matrix of vector  $\mathbf{x}$  is constructed:

$$\mathbf{X} = \begin{pmatrix} x(1) & x(2) & \dots & x(M+1) \\ x(2) & x(3) & \dots & x(M+2) \\ \dots & \dots & \dots & \dots \\ x(N-M) & x(N-M+1) & \dots & x(N) \end{pmatrix} \quad (4.18)$$

where  $M$  is the pencil parameter with  $d \leq M \leq N - d$  [52, 53], which is used to eliminate the noise effects in the data. The matrix pencil is defined as  $\mathbf{X}_2 - \lambda \mathbf{X}_1$ , with  $\mathbf{X}_1$  and  $\mathbf{X}_2$  are the two sub-matrices of  $\mathbf{X}$ , where  $\mathbf{X}_1 = \mathbf{X}(:, 1 : M)$  and  $\mathbf{X}_2 = \mathbf{X}(:, 2 : M + 1)$ , with a scalar parameter  $\lambda$ .  $\mathbf{X}_1$  and  $\mathbf{X}_2$  can be written as:

$$\begin{aligned} \mathbf{X}_1 &= \mathbf{Z}_1 \mathbf{S}_0 \mathbf{Z}_2 \\ \mathbf{X}_2 &= \mathbf{Z}_1 \mathbf{S}_0 \mathbf{Z}_0 \mathbf{Z}_2 \end{aligned}$$

where

$$\mathbf{Z}_1 = \begin{pmatrix} 1 & 1 & \dots & 1 \\ z_1 & z_2 & \dots & z_d \\ \dots & \dots & \dots & \dots \\ z_1^{N-M-1} & z_2^{N-M-1} & \dots & z_d^{N-M-1} \end{pmatrix}$$

$$\mathbf{Z}_2 = \begin{pmatrix} 1 & z_1 & \dots & z_1^{M-1} \\ 1 & z_2 & \dots & z_2^{M-1} \\ \dots & \dots & \dots & \dots \\ 1 & z_d & \dots & z_d^{M-1} \end{pmatrix}$$

$$\mathbf{Z}_0 = \text{diag}\{z_1, z_2, \dots, z_d\}$$

$$\mathbf{S}_0 = \text{diag}\{z_{10}s_1, z_{20}s_2, \dots, z_{d0}s_d\}$$

Using the above notation, the matrix pencil becomes:

$$\mathbf{X}_2 - \lambda \mathbf{X}_1 = \mathbf{Z}_1 \mathbf{S}_0 \{\mathbf{Z}_0 - \lambda \mathbf{I}_{d \times d}\} \mathbf{Z}_2 \quad (4.19)$$

where  $\mathbf{I}_{d \times d}$  is a  $d \times d$  identity matrix. Because of  $d \leq M \leq N - d$ , the rank of  $\mathbf{X}_1$  and  $\mathbf{X}_2$  is  $d$ . Under the condition of  $\lambda = z_k$ ,  $k = 1, 2, \dots, d$ ,  $\mathbf{X}_2 - \lambda \mathbf{X}_1 = 0$ . Then, the parameters  $z_k$  can be estimated as the generalized eigenvalues of the matrix pair  $[\mathbf{X}_2, \mathbf{X}_1]$ ,  $\mathbf{Z} = \mathbf{X}_1^+ \mathbf{X}_2$ ,  $\mathbf{Z}$  is a matrix whose eigenvalues are the estimated generalized eigenvalues of the matrix pair  $[\mathbf{X}_2, \mathbf{X}_1]$ .

In practice, noise is considered, then the received signal vector becomes  $\mathbf{A}\mathbf{s} + \mathbf{b}$ . The total least-squares MPM [52, 54] is used for the time delays and roughness parameters estimation. The details are shown as follows:

1. The singular-value decomposition (SVD) is carried out on  $\mathbf{X}$ ,  $\mathbf{X} = \mathbf{U}\mathbf{\Phi}\mathbf{V}^H$ .  $\mathbf{U}$  and  $\mathbf{V}$  are the matrices composed of the eigenvectors of  $\mathbf{X}\mathbf{X}^H$  and  $\mathbf{X}^H\mathbf{X}$ , respectively,  $\mathbf{\Phi}$  is a diagonal matrix which contains the singular values of  $\mathbf{X}$ .
2. Let us write the SVD-truncated versions of  $\mathbf{X}_1$  and  $\mathbf{X}_2$ :

$$\mathbf{X}_{d,1} = \mathbf{U}_d \mathbf{\Phi}_d \mathbf{V}_{d,1}^H \quad (4.20)$$

$$\mathbf{X}_{d,2} = \mathbf{U}_d \mathbf{\Phi}_d \mathbf{V}_{d,2}^H \quad (4.21)$$

where  $\mathbf{\Phi}_d$  is the upper left ( $d \times d$ ) block of  $\mathbf{\Phi}$  which contains the largest  $d$  singular values of  $\mathbf{X}$ ,  $\mathbf{U}_d$  and  $\mathbf{V}_d$  are the matrices containing the first  $d$  columns of  $\mathbf{U}$  and  $\mathbf{V}$  corresponding to the largest  $d$  singular values of  $\mathbf{X}$ , respectively.

$$\mathbf{V}_d = \begin{pmatrix} \mathbf{V}_{d,1} \\ - \end{pmatrix} = \begin{pmatrix} - \\ \mathbf{V}_{d,2} \end{pmatrix} \quad (4.22)$$

3. As the eigenvalues of  $\mathbf{Z}$  depend on the time delays and roughness parameters, we calculate  $\mathbf{Z}$  by a least square solution:

$$\begin{aligned}\mathbf{Z} &= \mathbf{X}_{d,1}^+ \mathbf{X}_{d,2} = \{\mathbf{U}_d \mathbf{\Phi}_d \mathbf{V}_{d,1}^H\}^+ \mathbf{U}_d \mathbf{\Phi}_d \mathbf{V}_{d,2}^H \\ &= (\mathbf{V}_{d,1}^H)^+ \mathbf{\Phi}_d^+ \mathbf{U}_d^+ \mathbf{U}_d \mathbf{\Phi}_d \mathbf{V}_{d,2}^H = (\mathbf{V}_{d,1}^H)^+ \mathbf{V}_{d,2}^H\end{aligned}\quad (4.23)$$

4. The time delays and roughness parameters can be estimated by calculating the eigenvalues of  $\mathbf{Z}$  as follows:

$$\begin{aligned}t_k &= -\angle z_k / (2\pi \Delta f) \\ b_k &= -\ln |z_k| / (\Delta f)\end{aligned}$$

where  $z_k$  is the  $k$ th largest eigenvalue of  $\mathbf{Z}$  ( $k = 1, 2, \dots, d$ ),  $\angle$  the angle and  $|\cdot|$  the absolute value.

#### 4.2.4 Time Delays and Roughness Parameters with ESPRIT

As the interface roughness is taken into account in the signal model, ESPRIT algorithm [36] is extended for estimating the time delays and the roughness parameters. Then, it will be called TDRP-ESPRIT (for Time Delays and Roughness Parameters). ESPRIT algorithm will be applied on the covariance matrix  $\mathbf{R}_{SSP}$  in Eq. (4.11) and  $\mathbf{R}_{SSP-PM}$  in Eq. (4.13). In the following section, the TDRP-ESPRIT is explained with matrix  $\mathbf{R}_{SSP}$  in Eq. (4.13). For the case where the TDRP-ESPRIT is used with matrix  $\mathbf{R}_{SSP-PM}$ , the calculation is simplified. ESPRIT algorithm divides the mode matrix  $\mathbf{A}_L$  into two overlapping data sub-bands. Sub-bands comprise of  $L - 1$  samples and overlap with each other by  $L - 2$  samples. The  $((L - 1) \times d)$  dimensional mode matrices of each sub-band,  $\mathbf{A}_1$  and  $\mathbf{A}_2$ , are related to each other by the  $(d \times d)$  diagonal matrix  $\mathbf{D}$ , whose elements depend on the time delays and roughness parameters to be estimated as:

$$\mathbf{A}_2 = \mathbf{A}_1 \mathbf{D} \quad (4.24)$$

such that

$$\mathbf{A}_L = \begin{pmatrix} \mathbf{A}_1 \\ - \end{pmatrix} = \begin{pmatrix} - \\ \mathbf{A}_2 \end{pmatrix} \quad (4.25)$$

As matrix  $\mathbf{D}$  cannot be estimated from data, according to [38], on the basis of the generalized singular value decomposition (GSVD) of the data covariance matrix, it

can be shown that the diagonal elements of  $\mathbf{D}$  can be retrieved from the following similar matrix  $\Psi$ . We try to find matrix  $\Psi$  which has the same eigenvalues as matrix  $\mathbf{D}$ :

$$\Psi = \mathbf{T}^{-1}\Phi\mathbf{T} \quad (4.26)$$

where  $\mathbf{T}$  is a  $(d \times d)$  dimensional invertible matrix. The idea of this algorithm is the similar with the algorithm presented in section 2.5.4. In this section, ESPRIT is adapted to the new signal model in Eq. (4.1). According to [38], from the GSVD of the signal covariance matrix  $\mathbf{R}_{sig} = \mathbf{A}_L \left[ \frac{1}{M} \sum_{k=1}^M \mathbf{D}^{k-1} \mathbf{S} (\mathbf{D}^{k-1})^H \right] \mathbf{A}_L^H = \mathbf{A}_L \bar{\mathbf{S}} \mathbf{A}_L^H$ , we have:

$$\mathbf{R}_{sig} \mathbf{V}_{sig} = \Sigma_o \mathbf{V}_{sig} \mathbf{K} \quad (4.27)$$

where the generalized eigenvectors  $\mathbf{v}_k$  associated with the signal subspace are arranged in matrix  $\mathbf{V}_{sig}$  as columns, matrix  $\mathbf{K} = \text{diag}(\lambda_1, \lambda_2, \dots, \lambda_d)$ ;  $\lambda_i$  is the  $i$ th generalized eigenvalue of covariance matrix  $\mathbf{R}_{sig}$ . Because matrix  $\mathbf{D}$  cannot be estimated from data, ESPRIT further exploits the linear relation in Eq. (4.24) within the GSVD of the data covariance matrix in Eq. (4.27). Let us write the GSVD in Eq. (4.27) in each sub-band data as follows:

$$\mathbf{R}_{sig,1} \mathbf{V}_{sig} = \Sigma_{o,1} \mathbf{V}_{sig} \mathbf{K} \quad (4.28)$$

$$\mathbf{R}_{sig,2} \mathbf{V}_{sig} = \Sigma_{o,2} \mathbf{V}_{sig} \mathbf{K} \quad (4.29)$$

where  $\mathbf{R}_{sig,j}$  ( $j = 1, 2$ ) are the  $((L-1) \times L)$  dimensional matrices, defined from the partitioning of the covariance matrix of the signal, which are expressed as:

$$\mathbf{R}_{sig,1} = \mathbf{A}_1 \bar{\mathbf{S}} \mathbf{A}_L^H \quad (4.30)$$

$$\mathbf{R}_{sig,2} = \mathbf{A}_2 \bar{\mathbf{S}} \mathbf{A}_L^H \quad (4.31)$$

where  $\Sigma_{o,1}$  and  $\Sigma_{o,2}$  are two  $((L-1) \times L)$  dimensional sub-matrices of  $\Sigma_o$  defined as:

$$\Sigma_o = \begin{pmatrix} \Sigma_{o,1} \\ - \end{pmatrix} = \begin{pmatrix} - \\ \Sigma_{o,2} \end{pmatrix} \quad (4.32)$$

At the first step, the latter definition and the expression of  $\mathbf{A}_2$  in Eq. (4.24) are substituted for Eq. (4.29). Some mathematical manipulations lead to the following equation:

$$\mathbf{A}_1 \mathbf{D} \mathbf{T} = \Sigma_{o,2} \mathbf{V}_{sig} \quad (4.33)$$

where

$$\mathbf{T} = \bar{\mathbf{S}} \mathbf{A}_L^H \mathbf{V}_{sig} \mathbf{K}^{-1}. \quad (4.34)$$

Similarly, Eqs. (4.28), (4.30) and (4.31) are used to obtain the following expression for matrix  $\mathbf{A}_1$ :

$$\mathbf{A}_1 = \Sigma_{o,1} \mathbf{V}_{sig} \mathbf{T}^{-1} \quad (4.35)$$

At the second step, substituting Eq. (4.35) for Eq. (4.33), this leads to:

$$\Sigma_{o,1} \mathbf{V}_{sig} \mathbf{T}^{-1} \mathbf{D} \mathbf{T} = \Sigma_{o,2} \mathbf{V}_{sig} = \Sigma_{o,1} \mathbf{V}_{sig} \Psi \quad (4.36)$$

where  $\Psi$  is a  $(d \times d)$  dimensional matrix defined in Eq. (4.26), which shows that  $\Psi$  and  $\mathbf{D}$  are similar matrices, therefore they have the same eigenvalues. A least squares solution can be used to calculate  $\Psi$  from Eq. (4.36):

$$\Psi = \left( (\Sigma_{o,1} \mathbf{V}_{sig})^H \Sigma_{o,1} \mathbf{V}_{sig} \right)^{-1} (\Sigma_{o,1} \mathbf{V}_{sig})^H \Sigma_{o,2} \mathbf{V}_{sig}$$

The time delays and roughness parameters can be estimated by calculating the eigenvalues of  $\Psi$  as follows:

$$\begin{aligned} t_k &= -\angle \psi_k / (2\pi \Delta f) \\ b_k &= -\ln |\psi_k| / (\Delta f) \end{aligned}$$

where  $\psi_k$  is the  $k$ th eigenvalue of  $\Psi$ .

When the covariance matrix  $\mathbf{R}_{SPP-PM}$  is applied, we make an eigendecomposition of the signal matrix  $\mathbf{R}_{sig}$  with  $\mathbf{R}_{sig} \mathbf{V}_{sig} = \mathbf{V}_{sig} \mathbf{K}$ . Then, the TDRP-ESPRIT algorithm is applied.

### 4.3 Permittivity estimation

By using the estimated time delays  $\hat{t}_k$  and roughness parameters  $\hat{b}_k$ , the echoes amplitude  $s$  can be estimated from the signal model. Then, the permittivity of each layer can be deduced from [8]. Since the noise is considered as a white Gaussian noise with zero mean, a least squares method is used to estimate the echoes amplitudes as follows:

$$\hat{\mathbf{s}} = (\hat{\mathbf{A}}^H \hat{\mathbf{A}})^{-1} \hat{\mathbf{A}}^H \mathbf{\Lambda}^{-1} \mathbf{r} \quad (4.37)$$

with  $\hat{\mathbf{A}} = \left[ \mathbf{a}(\hat{T}_1, \hat{b}_1) \ \mathbf{a}(\hat{T}_2, \hat{b}_2) \ \dots \ \mathbf{a}(\hat{T}_d, \hat{b}_d) \right]$ , the  $(N \times d)$  mode matrix of which the time delays and the roughness parameters are estimated by high resolution methods (subspace methods). Then, the permittivity of each layer can be deduced from the echo amplitudes. In our case, we only study the permittivity of the first layer. It is given by the following relation [8]:

$$\hat{\epsilon}_r = \left( \frac{1 - \hat{s}_1}{1 + \hat{s}_1} \right)^2 \quad (4.38)$$

where  $\hat{s}_1$  represents the estimated amplitude of the first backscattered echo.

## 4.4 Performance evaluation

In this section, the performance of high resolution methods: the modified root-MUSIC, TDRP-ESPRIT and the modified MPM is tested on the data simulated from PILE method. Because of the high computational load, the performance of 2-D MUSIC is not studied, only an example is shown in section 4.2.1. In the following, we evaluate the performance of the proposed algorithms by calculating the RRMSE on the estimated time delays and roughness parameters against the SNR. In addition, the thickness and the permittivity estimations are also analysed.

### 4.4.1 Simulation parameters

The performance of the proposed algorithms is evaluated by a Monte-Carlo process. The simulation data represent the radar backscattered signal at nadir from a rough pavement made up of two uncorrelated random rough interfaces separating homogeneous media. The studied pavement structure (see Fig. 3.1) is made up of a layer medium of UTAS with relative permittivity equal to 4.5 overlying a baseband with relative permittivity equal to 7. In the simulations, we study 4 pavements with differ-

Case #	Roughness parameters ( $\sigma_{hA}, L_{cA}, \sigma_{hB}, L_{cB}$ )	Fitting results ( $b_1, b_2$ )	Conductivity ( $\delta_A, \delta_B$ )
a	(0.5, 6.4, 1.0, 15) mm	$(1.13, 10.9) \times 10^{-3} \text{ GHz}^{-1}$	(0, 0)
b	(0.5, 6.4, 2.0, 15) mm	$(1.13, 40.4) \times 10^{-3} \text{ GHz}^{-1}$	(0, 0)
c	(1.0, 6.4, 2.0, 15) mm	$(3.83, 39.3) \times 10^{-3} \text{ GHz}^{-1}$	(0, 0)
d	(1.0, 6.4, 2.0, 15) mm	$(3.85, 40.9) \times 10^{-3} \text{ GHz}^{-1}$	$(5, 10) \times 10^{-3} \text{ S/m}$

Table 4.1: Parameters of the layered medium pavement and fitting results: for each case ( $a, b, c, d$ ), the root mean square height  $\sigma_h$  and the correlation length  $L_h$  of the two interfaces and the curve fitting results of associated PILE method [44]. The subscript  $A$  represents the first interface and  $B$  the second interface. The symbol  $\delta$  represents the conductivity.

ent interface roughnesses (the rough interfaces are assumed to have a Gaussian height probability density function and an exponential height autocorrelation function) [15] and media conductivities. From curve fitting results of PILE in the previous chapter, the roughness parameters are estimated and presented in Table 4.4.1. Case 3 and case 4 have same surface layer roughness, but with the different conductivities (for the first two layers). Case 3 represents lossless media, whereas case 4 represents slightly lossy media. The fitting results for the lossless media and low-loss media are almost the same (cases  $c$  and  $d$ ). Indeed, the roughness parameters increase of 0.5% (from  $3.83 \times 10^{-3} \text{ GHz}^{-1}$  to  $3.85 \times 10^{-3} \text{ GHz}^{-1}$ ) and 4% (from  $39.3 \times 10^{-3} \text{ GHz}^{-1}$  to  $40.9 \times 10^{-3} \text{ GHz}^{-1}$ ) for the first and the second interfaces, respectively. In this case, the conductivity has a very small influence. The frequency band is 1.0 – 3.0 GHz, with 0.04 GHz steps (51 frequency samples). The preprocessing PM is also used. A comparison of the results from the modified root-MUSIC, TDRP-ESPRIT and the modified MPM is carried out. SSP technique is used to reduce the cross-correlation between the echoes, the number of sub-bands ( $M$ ) is equal to 20 (note that SSP and the PM are not used in the modified MPM). The SNR is defined as the ratio between the power of the second echo (which is associated to the scattering from the lower interface) at the first frequency and the noise variance. The performance of the proposed algorithms is assessed with a Monte-Carlo process of 200 independent runs of the algorithm with independent noise snapshots and by the RRMSE of the evaluated parameter as follows:

$$RRMSE(z) = \frac{\sqrt{\frac{1}{U} \sum_{j=1}^U (\hat{z}_j - z)^2}}{z}$$

where  $\hat{z}_j$  denotes the estimated parameter for the  $j^{th}$  run of the algorithm, and  $z$  the true value. In the simulations, the parameter  $z$  can represent either the first ( $t_1$ ) or

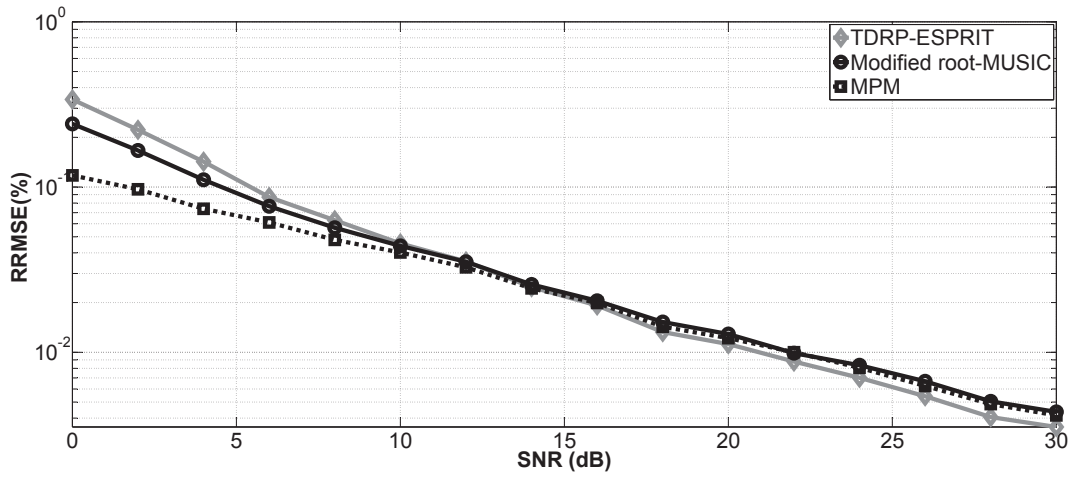
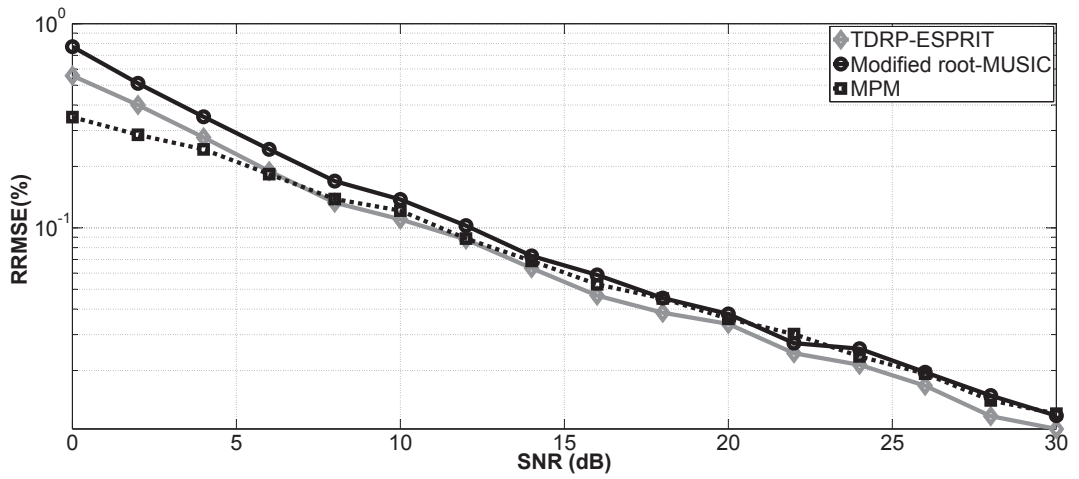
the second ( $t_2$ ) time delay, the first ( $b_1$ ) or the second ( $b_2$ ) roughness parameter, the permittivity of the first layer ( $\epsilon_r$ ), or the thickness ( $H$ ) of the first layer.

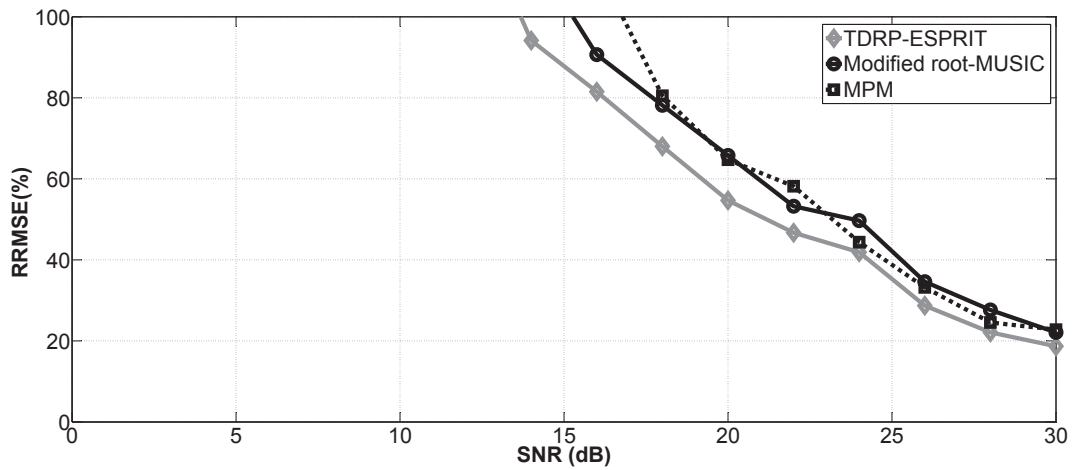
#### 4.4.2 Simulation results

In the first eight simulations (Figs. 4.4–4.11), we consider two backscattered echoes with time delays 1 ns and 1.3 ns, corresponding to a layer thickness  $H \approx 20$  mm (the relative permittivity is equal to 4.5). The two echoes are slightly overlapped, as the  $B\Delta\tau$  product is equal to 0.6. A comparison is carried out between the modified root-MUSIC, the modified MPM and TDRP-ESPRIT. Figs. 4.4, 4.6, 4.8, 4.10 plot the RRMSE on the estimated time delay  $\hat{t}_1$  or  $\hat{t}_2$  versus the SNR for the 4 cases depicted in Table 4.4.1. Figs. 4.5, 4.7, 4.9, 4.11 plot the RRMSE on the estimated roughness parameter  $\hat{b}_1$  or  $\hat{b}_2$  versus the SNR for the 4 different cases. For both the time delays and roughness parameters, as expected, it can be seen that the RRMSE continuously decreases with increasing SNR. For the TDE, the RRMSE vs. the SNR is similar with different roughness parameters, which means that the interface roughness has only a slight influence on the estimation of the time of arrival. For the roughness parameter estimation, the RRMSE of the roughness parameter of the second echo is smaller than the first one and we can notice that the larger  $b$  is, the smaller RRMSE we have, as it is easy to detect large roughness. Furthermore, the proposed algorithms can also handle the low-loss media case (case  $d$ ) with small RRMSE, as shown in Figs. 4.10 and 4.11.

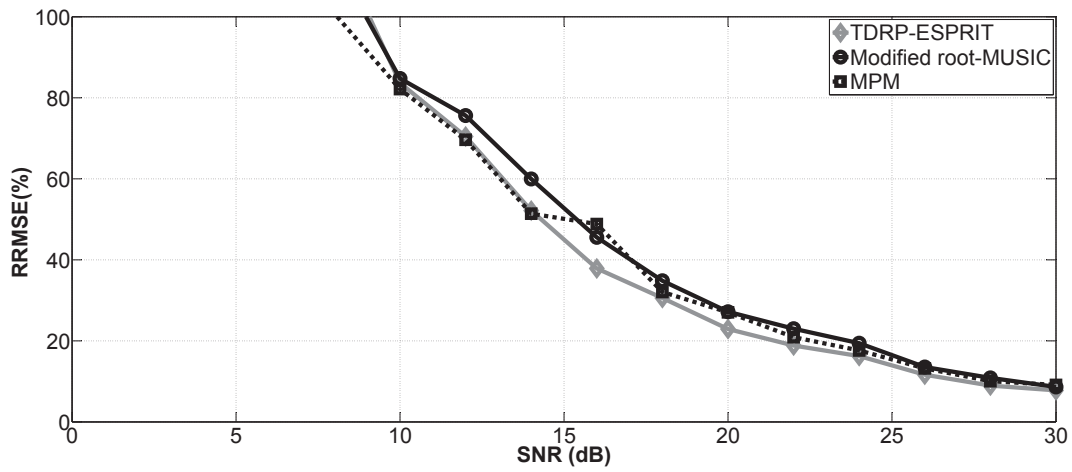
Comparing the 3 algorithms, the modified MPM offers the best performance especially at low SNR for both the time delays and roughness parameters estimation for the 4 different rough pavements. However, at high SNR, these methods tend toward similar performances.

In the second simulation, the layer permittivity and thickness are assessed by using estimated time delays and roughness parameters from the TDRP-ESPRIT. Fig. 4.12 shows the RRMSE of the estimated permittivity and thickness of the first layer ( $\hat{\epsilon}_r, \hat{H}$ ) vs. the SNR for case 3. RRMSE also continuously decreases with increasing SNR. According to Fig. 4.12, the RRMSE of the permittivity and thickness is smaller than 5% when  $\text{SNR} = 0$  dB, and tends to be much smaller with increasing SNR. From simulations, it can be seen that the proposed algorithm shows good performance in parameter estimations.

(a)  $t_1$ (b)  $t_2$ Figure 4.4: Case  $a$ : RRMSE on the estimated time of arrival  $t_k$  ( $k = 1, 2$ ) versus SNR after SSP



(a)  $b_1$



(b)  $b_2$

Figure 4.5: Case  $a$ : RRMSE on the estimated roughness parameter  $b_k$  ( $k = 1, 2$ ) versus SNR after SSP

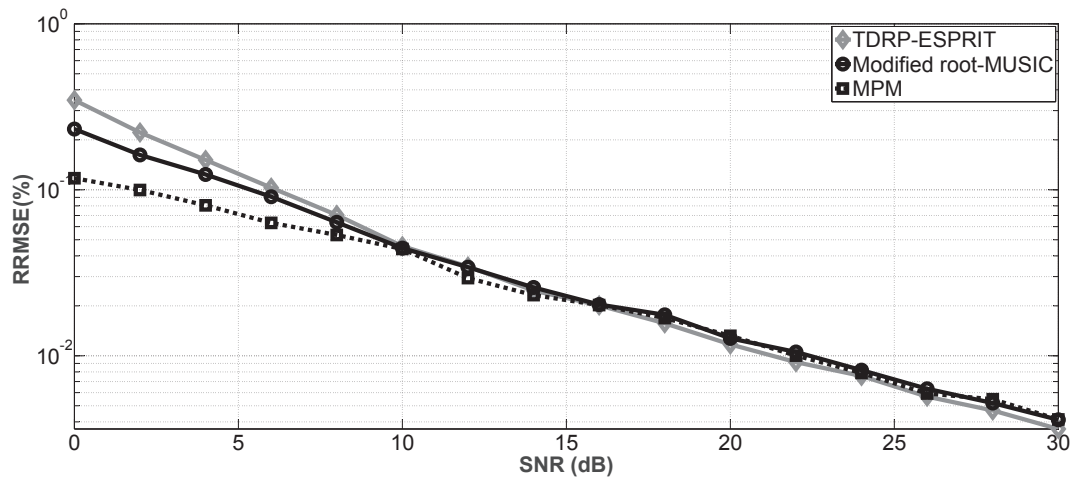
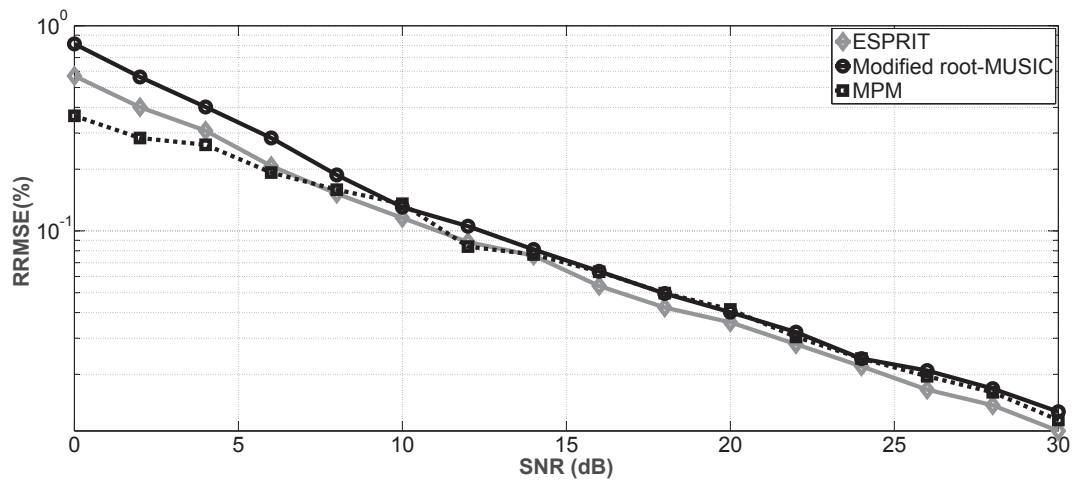
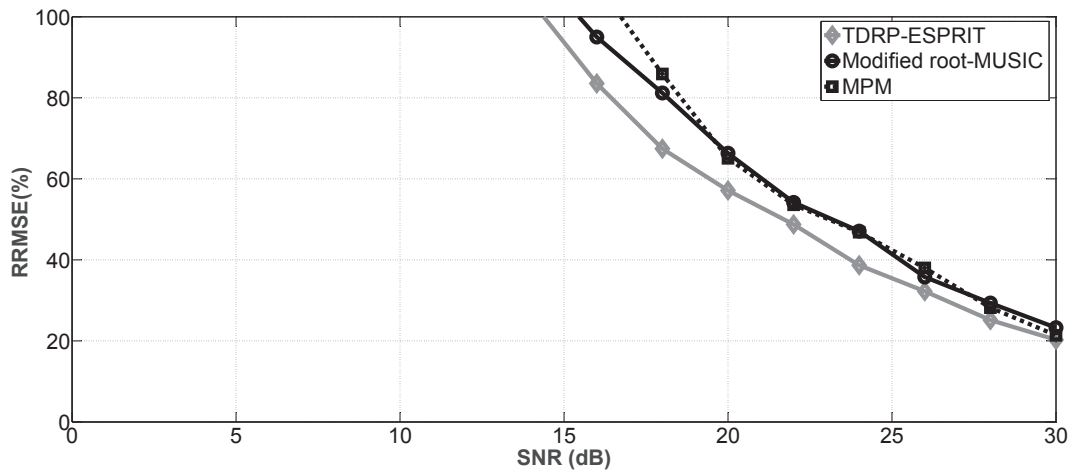
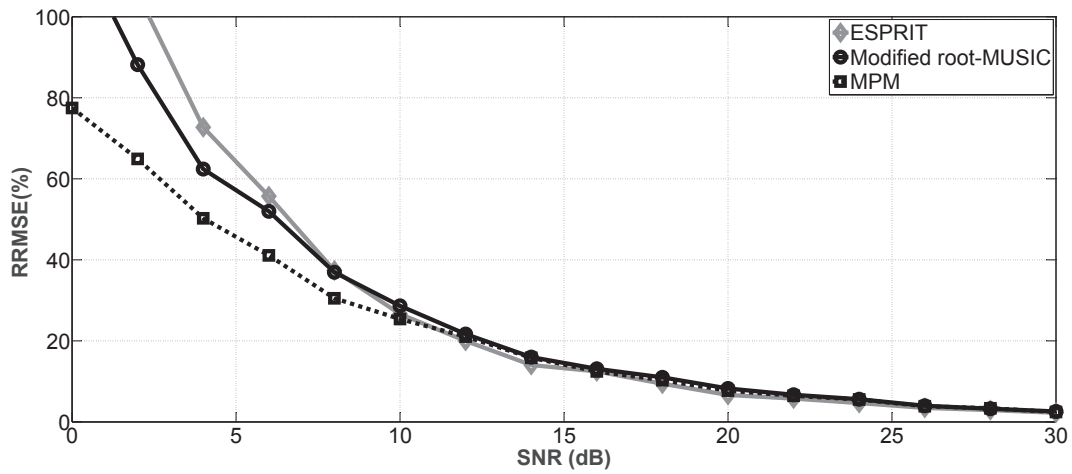
(a)  $t_1$ (b)  $t_2$ 

Figure 4.6: Case  $b$ : RRMSE on the estimated time of arrival  $t_k$  ( $k = 1, 2$ ) versus SNR after SSP



(a)  $b_1$



(b)  $b_2$

Figure 4.7: Case  $b$ : RRMSE on the estimated roughness parameter  $b_k$  ( $k = 1, 2$ ) versus SNR after SSP

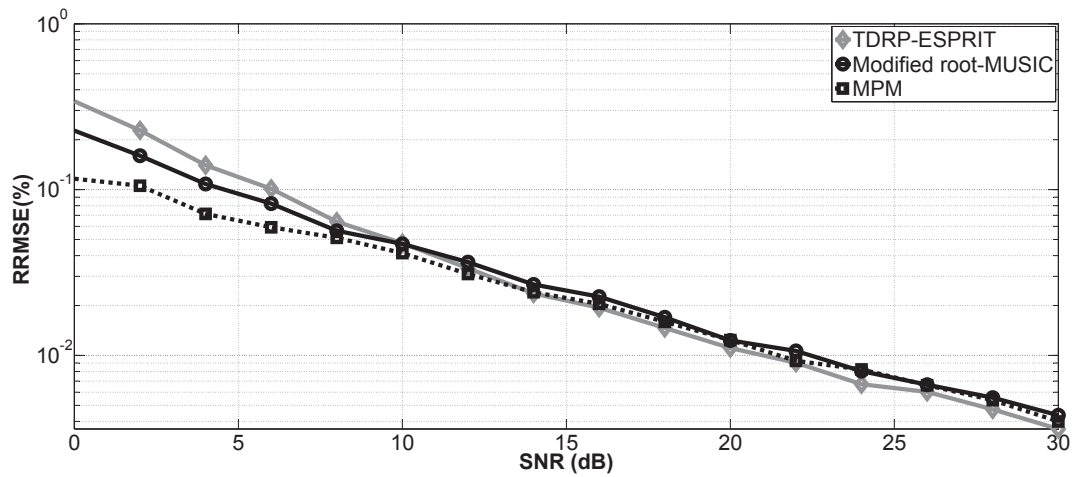
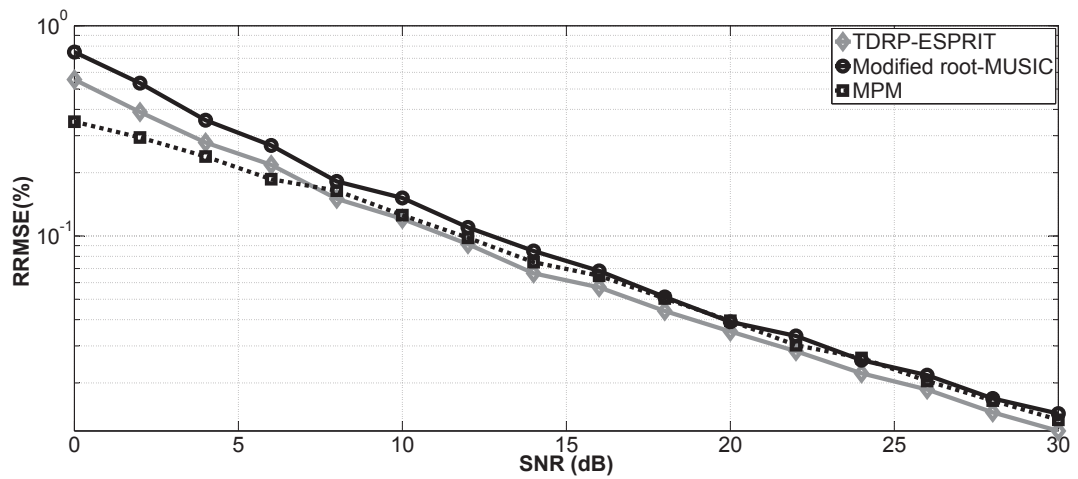
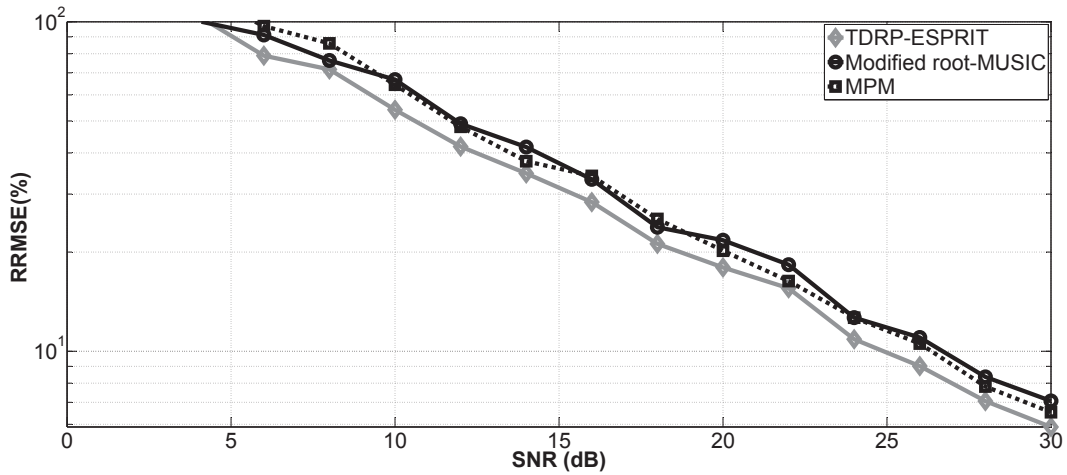
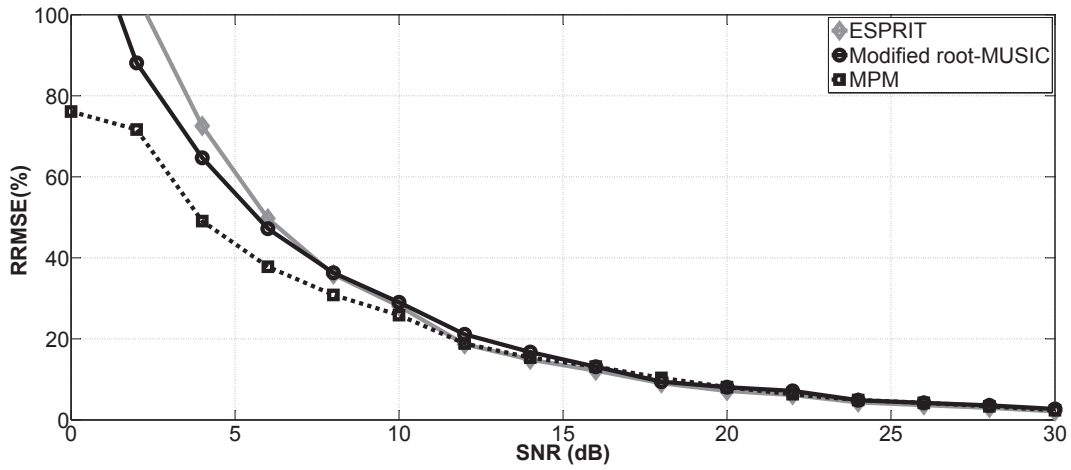
(a)  $t_1$ (b)  $t_2$ 

Figure 4.8: Case  $c$ : RRMSE on the estimated time of arrival  $t_k$  ( $k = 1, 2$ ) versus SNR after SSP



(a)  $b_1$



(b)  $b_2$

Figure 4.9: Case  $c$ : RRMSE on the estimated roughness parameter  $b_k$  ( $k = 1, 2$ ) versus SNR after SSP

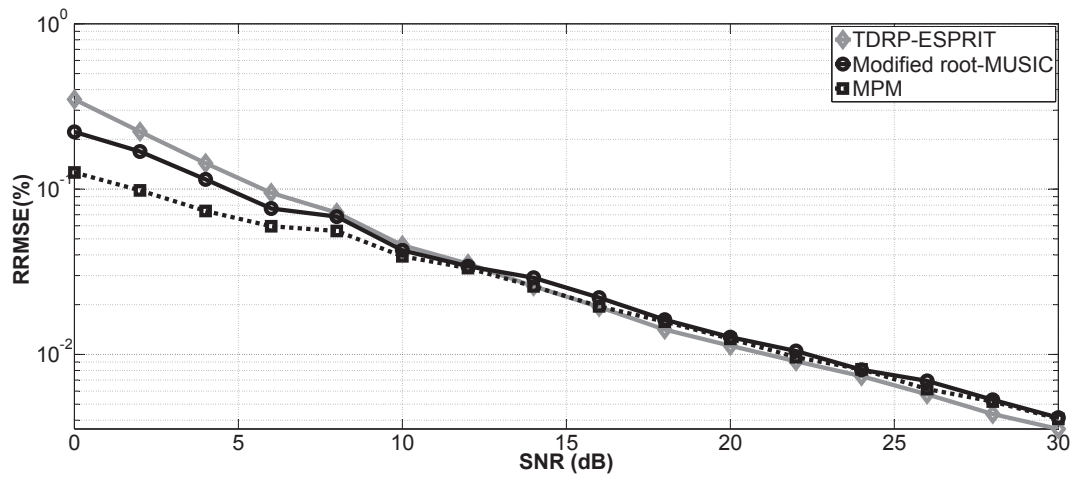
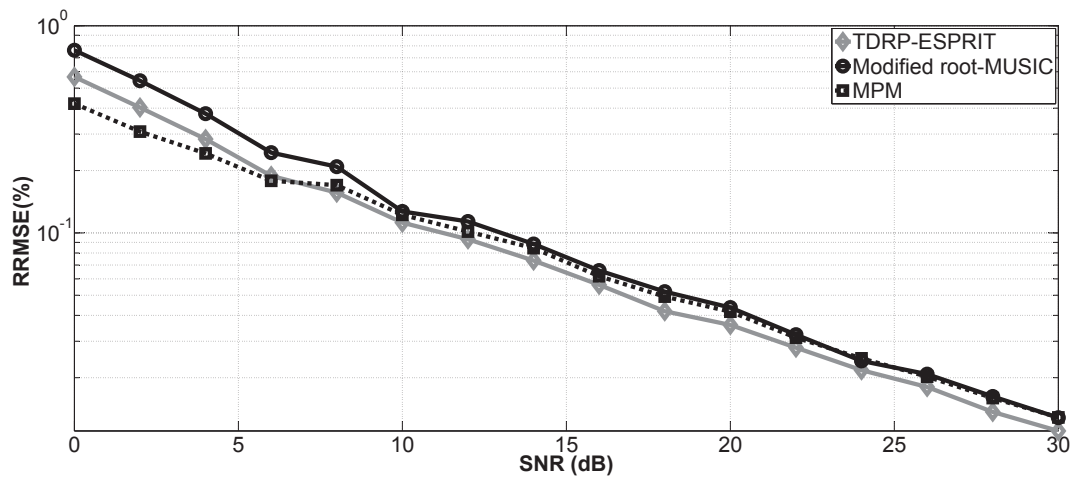
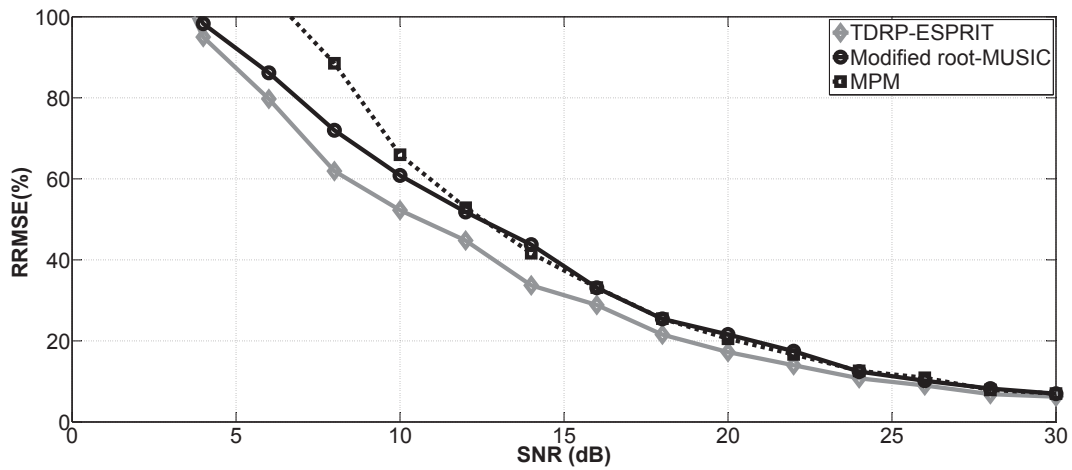
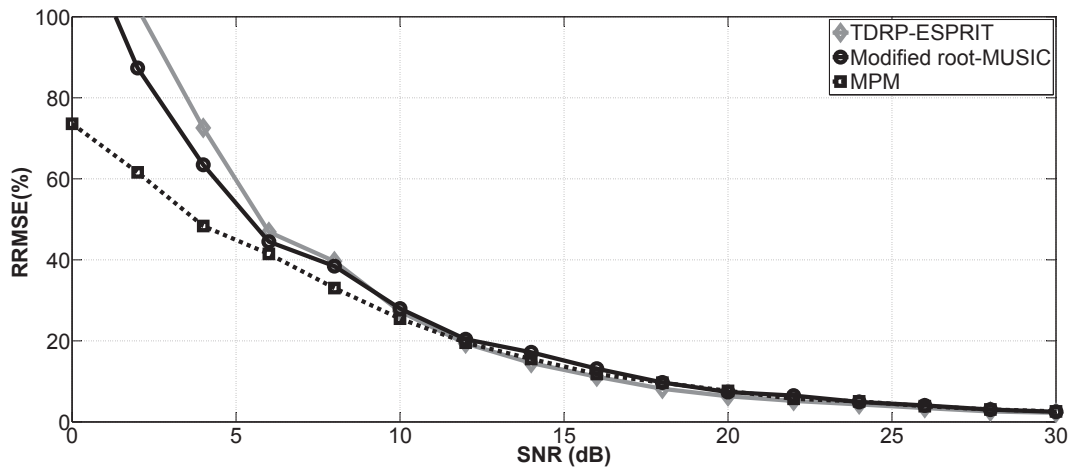
(a)  $t_1$ (b)  $t_2$ 

Figure 4.10: Case  $d$ : RRMSE on the estimated time of arrival  $t_k$  ( $k = 1, 2$ ) versus SNR after SSP



(a)  $b_1$



(b)  $b_2$

Figure 4.11: Case  $d$ : RRMSE on the estimated roughness parameter  $b_k$  ( $k = 1, 2$ ) versus SNR after SSP

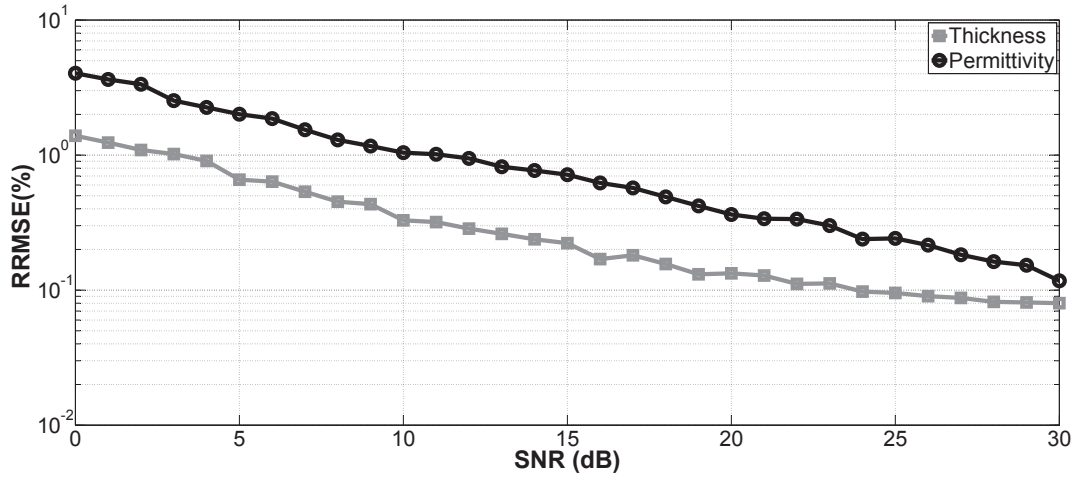


Figure 4.12: Case *c*: RRMSE of the estimated permittivity and thickness of the first layer ( $\epsilon_r$ ,  $H$ ) vs. the SNR by TDRP-ESPRIT

## 4.5 Conclusion

In this chapter, the influence of interface roughness has been taken into account in the signal model. The frequency behaviour of backscattered echoes can be modelled by an exponential function, which provides satisfactory results for a narrow frequency bandwidth (less than 2 GHz). We have proposed to extend the subspace methods (the modified 2-D MUSIC, the modified root-MUSIC, the modified MPM and TDRP-ESPRIT) for jointly estimating the time delays and interface roughness by using the exponential model. Preprocessing methods (SSP and PM) have been applied in order to enhance the performance of the proposed algorithms.

The proposed algorithms can be applied to road surface layer surveys (for the estimation of thin pavement thicknesses) by taking the interface roughness into account. The performance of the proposed algorithms has been tested on different roughness pavements. The modified 2-D MUSIC, the modified root-MUSIC, the modified MPM and TDRP-ESPRIT show a good performance in parameter estimations. In the following chapter, more complex but realistic signal models (Gaussian and mixed models) are presented.



## Parameter estimation for Gaussian and mixed models

In the previous chapter, the time delays and roughness parameters estimation has been carried out by taking into account an exponential frequency behaviour. In this situation, the high resolution methods can be easily applied for parameter estimation (time delays and roughness). However, this assumption is only suitable for narrow frequency bands (less than 2 GHz). With widening of the frequency band, curve fitting errors increase rapidly, which may bring errors to the interface roughness estimation.

It has been found in Chapter 3 that the frequency behaviour  $w(f)$  can be better approximated by a Gaussian function or a mixed function for UWB radar ( $B > 2$  GHz). In these case, we can assume that the frequency behaviour has an expression  $w_k(f_i) \approx \exp(-b_k f_i^2)$  for the Gaussian model and  $w_k(f_i) \approx \exp(-b_k f_i^2 - c_k f_i)$  for the mixed model, with  $b_k$  and  $c_k$  are the roughness parameters of the  $k$ th interface.

In order to estimate the time delays and roughness parameters for the Gaussian and mixed models, firstly we propose multi-dimensional search methods: the MLE and generalized MUSIC algorithm, however their computational burdens are very high. Then, to reduce the computational complexity of the multi-dimensional methods, we propose a modified MUSIC algorithm with one dimensional search for TDE. It can take into account several possible frequency behaviours, more suitable for UWB GPR. Finally, the frequency behaviour of backscattered echoes can be estimated.

This chapter is organized as follows: in section 2, the radar data models of the Gaussian and mixed models are presented. Then, in section 3, we propose multi-dimensional search methods for the time delays and roughness parameters estimation. In section 4, a modified MUSIC algorithm is proposed to estimate the time delays without knowing the frequency behaviour. Then, the frequency behaviour of backscattered echoes is calculated with the estimated time delays. Simulation results and a discussion on the performance of the proposed algorithms are given in section 5. Finally, conclusions are drawn.

## 5.1 Signal model

In the previous chapter, the signal model of the echoes backscattered from random rough inferences has been defined as Eq. (4.1):

$$r(f_i) = \sum_{k=1}^d e(f_i) s_k w_k(f_i) \exp(-j2\pi f_i t_k) + n(f_i)$$

the signal model in vector form shares same expression as Eq.(4.2):

$$\mathbf{r} = \mathbf{\Lambda} \mathbf{A} \mathbf{s} + \mathbf{n}$$

nevertheless in this section, there are some new definitions:

1. For Gaussian model, the mode matrix is defined as follows:  
 $\mathbf{A} = [\mathbf{a}(t_1, b_1) \ \mathbf{a}(t_2, b_2) \ \dots \ \mathbf{a}(t_d, b_d)]$  is the  $(N \times d)$  mode matrix;
2.  $\mathbf{a}(t_k, b_k) = [\exp(-2j\pi f_1 t_k - b_k f_1^2) \ \exp(-2j\pi f_2 t_k - b_k f_2^2) \ \dots \ \exp(-2j\pi f_N t_k - b_k f_N^2)]^T$  is the mode vector;
3. For the mixed model, the mode matrix is defined as follows:  
 $\mathbf{A} = [\mathbf{a}(t_1, b_1, c_1) \ \mathbf{a}(t_2, b_2, c_2) \ \dots \ \mathbf{a}(t_d, b_d, c_d)]$  is called the  $(N \times d)$  mode matrix;
4.  $\mathbf{a}(t_k, b_k, c_k) = [\exp(-2j\pi f_1 t_k - b_k f_1^2 - c_k f_1) \ \exp(-2j\pi f_2 t_k - b_k f_2^2 - c_k f_2) \ \dots \ \exp(-2j\pi f_N t_k - b_k f_N^2 - c_k f_N)]^T$  is the mode vector.

Then, the data are divided by the pulse and the new covariance matrix  $\mathbf{R}_0$  (same definition as Eq. (4.5)) is:

$$\mathbf{R}_0 = E(\mathbf{r}'\mathbf{r}'^H) = \mathbf{\Lambda}^{-1} \mathbf{Y} \mathbf{\Lambda}^{-H} = \mathbf{A} \mathbf{S} \mathbf{A}^H + \sigma^2 \mathbf{\Sigma}$$

## 5.2 Multi-dimensional search methods

In this section, we present 2 multi-dimensional search methods: the MLE and generalized MUSIC algorithms for the time delays and roughness parameters estimation.

### 5.2.1 Maximum likelihood estimation

In this section, MLE is applied for both the Gaussian and mixed models.

#### Gaussian model

For the Gaussian model, the frequency behaviour takes the form  $w_k(f_i) = \exp(-b_k f_i^2)$ . As the  $N$ -point data sets  $[r(f_1) r(f_2) \cdots r(f_N)]$  depends on the time delays and roughness parameters. We can rewrite the signal model as:

$$r(f) = \sum_{k=1}^d s_k e(f) \exp(-j2\pi f t_k - b_k f^2) + n(f) \quad (5.1)$$

The noise being a Gaussian white noise with zero mean and variance  $\sigma^2$ , the PDF of the noise is given by

$$F[n(f)] = \frac{1}{\pi\sigma^2} \exp\left\{-\frac{|r(f) - \sum_{k=1}^d s_k e(f) \exp(-j2\pi f t_k - b_k f^2)|^2}{\sigma^2}\right\}. \quad (5.2)$$

As we have  $N$  sampling points which are independent and equally distributed, the joint PDF for all observations is:

$$\begin{aligned} F(\mathbf{r}, t_k, b_k) \\ = \frac{1}{(\pi\sigma^2)^N} \exp\left\{-\frac{\sum_{i=1}^N |r(f_i) - \sum_{k=1}^d s_k e(f_i) \exp(-j2\pi f_i t_k - b_k f_i^2)|^2}{\sigma^2}\right\}. \end{aligned} \quad (5.3)$$

For the MLE, the results are obtained by maximizing a log-likelihood function instead of the joint density function, and the log-likelihood function is as follows:

$$\begin{aligned} L(\mathbf{r}, t_k, b_k) &= \ln F(\mathbf{r}, t_k, b_k) \\ &= -\frac{\sum_{i=1}^N |r(f_i) - \sum_{k=1}^d s_k e(f_i) \exp(-j2\pi f_i t_k - b_k f_i^2)|^2}{\sigma^2} - N \ln(\pi\sigma^2). \end{aligned} \quad (5.4)$$

The optimal estimation (for the time-delay  $t_k$  and the roughness parameter  $b_k$ ) is ob-

tained by finding the solution of the following equations:

$$\begin{cases} \frac{\partial L(\mathbf{r}, t_k, b_k)}{\partial t_k} = 0 \\ \frac{\partial L(\mathbf{r}, t_k, b_k)}{\partial b_k} = 0 \end{cases} \quad (5.5)$$

### Mixed model

For the mixed model, by using the same way as for the Gaussian model, the time delays and roughness parameters can be estimated. The difference comes from the expression of frequency behaviour: here,  $w_k(f_i) = \exp(-b_k f_i^2 - c_k f_i)$ . To replace  $w_k(f_i)$  in Eq. (5.1), (5.2), (5.3) and (5.4), we can get a new log-likelihood function is as follows:

$$\begin{aligned} L(\mathbf{r}, t_k, b_k, c_k) &= \ln F(\mathbf{r}, t_k, b_k, c_k) \\ &= -\frac{\sum_{i=1}^N |r(f_i) - \sum_{k=1}^d s_k e(f_i) \exp(-j2\pi f_i t_k - b_k f_i^2 - c_k f_i)|^2}{\sigma^2} - N \ln(\pi\sigma^2) \end{aligned} \quad (5.6)$$

For the mixed model, the optimal estimation is obtained by finding the solution of the following equations:

$$\begin{cases} \frac{\partial L(\mathbf{r}, t_k, b_k, c_k)}{\partial t_k} = 0 \\ \frac{\partial L(\mathbf{r}, t_k, b_k, c_k)}{\partial b_k} = 0 \\ \frac{\partial L(\mathbf{r}, t_k, b_k, c_k)}{\partial c_k} = 0 \end{cases} \quad (5.7)$$

## 5.2.2 Generalized MUSIC algorithm

In the previous chapter, MUSIC and a modified root-MUSIC have been used for the time delays and roughness parameters with an exponential frequency behaviour. As the backscattered echoes are perfectly correlated, sub-band averaging techniques should be applied. For a large frequency band ( $B > 2$  GHz), the exponential model is not realistic enough for describing the frequency variations of the amplitude of backscattered echoes. For a large frequency bandwidth, the Gaussian and mixed models are proposed. In this case, the frequency behaviour of backscattered echoes is no longer uniformly linear, and sub-band averaging techniques do not work. To solve this problem, we propose a generalized MUSIC algorithm [55] which is capable of handling coherent echoes with an arbitrary frequency behaviour. The drawback is that the pro-

posed algorithm still requires a multi-dimensional search.

We can use the generalized MUSIC algorithm for the time delays and roughness parameters estimation for both the Gaussian model and the mixed model. Note that we apply the Gaussian model for the following calculation. From [55], when echoes are fully correlated, we can find the relationship as follows:

$$\begin{aligned} & \mathbf{P}\{\mathbf{a}(t_1, b_1) + \rho_1 \mathbf{a}(t_2, b_2) + \dots + \rho_{d-1} \mathbf{a}(t_d, b_d)\} \\ &= \mathbf{P}\{\mathbf{a}(t_1, b_1), \mathbf{a}(t_2, b_2), \dots, \mathbf{a}(t_d, b_d)\} \begin{pmatrix} 1 \\ \rho_1 \\ \dots \\ \rho_{d-1} \end{pmatrix} \\ &= \mathbf{P}\{\mathbf{a}_1, \mathbf{a}_2, \dots, \mathbf{a}_d\} \mathbf{c} = 0 \end{aligned}$$

where  $\mathbf{P} = \mathbf{U}_n \mathbf{U}_n^H$ ,  $\mathbf{U}_n$  being the  $N \times (N - d)$  noise matrix whose columns are the  $N - d$  noise eigenvectors,  $\rho_i$  is the magnitude of reflection coefficient of the  $i$ th backscattered echoes of a flat pavement,  $\mathbf{a}_k = \mathbf{a}(t_k, b_k)$ ,  $k = 1, 2, \dots, d$ . Then, the pseudo-spectrum of the generalized MUSIC can be written as:

$$\begin{aligned} & P_G(t_1, b_1, t_2, b_2, \dots, t_d, b_d) \\ &= [\min_{\mathbf{c}} \left\{ \frac{\mathbf{c}^H \{\mathbf{a}_1, \mathbf{a}_2, \dots, \mathbf{a}_d\}^H \mathbf{P} \{\mathbf{a}_1, \mathbf{a}_2, \dots, \mathbf{a}_d\} \mathbf{c}}{\mathbf{c}^H \{\mathbf{a}_1, \mathbf{a}_2, \dots, \mathbf{a}_d\}^H \{\mathbf{a}_1, \mathbf{a}_2, \dots, \mathbf{a}_d\} \mathbf{c}} \right\}]^{-1} \end{aligned} \quad (5.8)$$

we can find that the above equation can be computed as the minimum root of the following quadratic equation in  $\lambda$ :

$$\det[\{\mathbf{a}_1, \mathbf{a}_2, \dots, \mathbf{a}_d\}^H \mathbf{P} \{\mathbf{a}_1, \mathbf{a}_2, \dots, \mathbf{a}_d\} - \lambda \{\mathbf{a}_1, \mathbf{a}_2, \dots, \mathbf{a}_d\}^H \{\mathbf{a}_1, \mathbf{a}_2, \dots, \mathbf{a}_d\}] = 0 \quad (5.9)$$

therefore, we can rewrite the pseudo-spectrum of the generalized MUSIC as:

$$P_G = \frac{1}{\lambda_{min}} \quad (5.10)$$

Eq. (5.9) is a generalized eigenvalue equation and has the root  $\lambda = 0$  only if  $\{\mathbf{a}_1, \mathbf{a}_2, \dots, \mathbf{a}_d\}^H \mathbf{P} \{\mathbf{a}_1, \mathbf{a}_2, \dots, \mathbf{a}_d\}$  is singular. Thus, the noise covariance matrix  $\mathbf{P}$  should be constructed from at least  $d$  noise eigenvectors (otherwise  $\lambda = 0$  is a root of the above equation for all echoes). By using the generalized MUSIC algorithm, the parameters estimation can be solved for the Gaussian model. In the same way, the algorithm can be easily applied on the mixed model.

### 5.2.3 Simulation examples

In this subsection, we provide some simulation examples about the multi-dimensional search methods. Because of computational complexity of the methods, only one rough layer is studied. The studied pavement structure is made up of a layer medium of UTAS with relative permittivity equal to 4.5. Thus, for a flat pavement, the reflection coefficient of the first backscattered echo is  $s \approx 0.3592$ . A curve fitting is made on the frequency behaviour of the echo by using the least squares method. Simulation parameters come from curve fitting results in Chapter 3. The roughness parameter of echo is  $b_1 = 1.62 \times 10^{-3} \text{ GHz}^{-2}$  (only the Gaussian model is tested here). We consider the echo corresponding to the time delay 1 ns, the frequency band is 0.5, 3.5 GHz with 61 frequency samples. The performance of the MLE and generalized MUSIC is assessed with a Monte-Carlo process of 200 independent runs with 500 independent snapshots and by the RRMSE of the evaluated parameter as follows:

$$RRMSE(z) = \frac{\sqrt{\frac{1}{U} \sum_{j=1}^U (\hat{z}_j - z)^2}}{z},$$

where  $\hat{z}_j$  denotes the estimated parameter for the  $j$ th run of the algorithm, and  $z$  the true value. In the simulation, the parameter  $z$  can represent either the ( $t_1$ ) time delay or the ( $b_1$ ) roughness parameter. Figs. 5.1 and 5.2 provide the RRMSE on the estimated

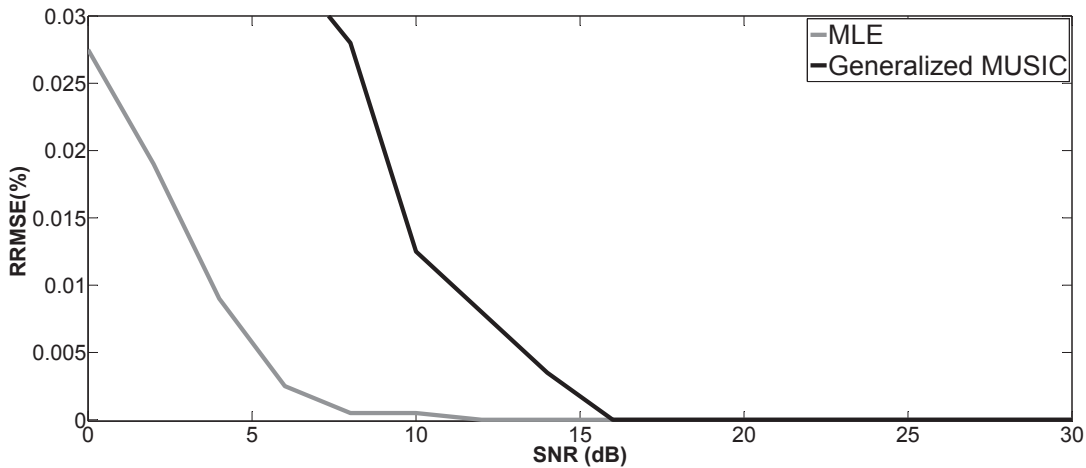


Figure 5.1: RRMSE on the estimated time delay  $t_1$  versus SNR by both MLE and generalized MUSIC after 200 Monte-Carlo simulations

time delay and roughness parameter versus SNR, respectively. For both the time delay and roughness parameter, it can be seen that the RRMSE continuously decreases with

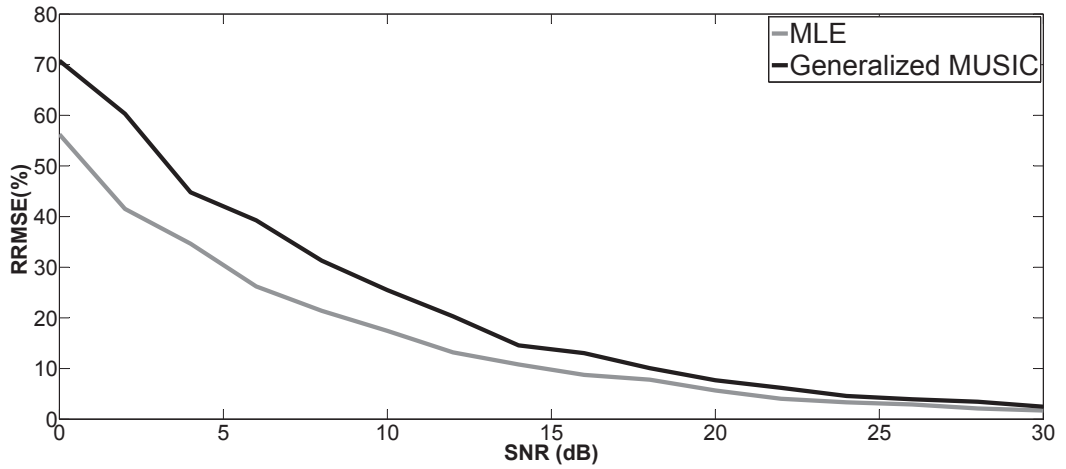


Figure 5.2: RRMSE on the estimated roughness parameter  $b_1$  versus SNR by both MLE and generalized MUSIC after 200 Monte-Carlo simulations

increasing SNR. We also observe from Figs. 5.1 and 5.2 that the MLE gives a better performance than the generalized MUSIC. It has smaller RRMSE in the whole SNR sets (see Figs. 5.1 and 5.2). For multiple layers, the computational load is substantial. Nevertheless, the methods are theoretically applicable to coherent echoes sets of the Gaussian and mixed models. To reduce the computational burden, in next section, a new modified MUSIC which needs only one search dimensional is proposed.

## 5.3 Modified MUSIC algorithm

In this section, we present a new modified MUSIC algorithm for the TDE with unknown shape of the frequency behaviour. An interpolation spatial smoothing technique is used to decorrelate the correlation between echoes.

### 5.3.1 Interpolation spatial smoothing technique

In practice, the correlation between echoes degrades the performance of the subspace methods. In this situation, preprocessing methods like the spatial smoothing techniques are used to obtain a new covariance matrix with restored rank. This kind of techniques only work for a uniformly linear frequency behaviour [39]. As the frequency behaviour of backscattered echoes can be various shapes, methods like the spatial smoothing technique cannot be used directly. In order to solve this problem, we propose to interpolate the frequency behaviour of backscattered echoes into a uni-

formly linear frequency behaviour. Then, the spatial smoothing techniques can be applied. This kind of algorithm is called interpolation spatial smoothing technique [56, 57].

The mode vector can be written as:

$$\begin{aligned} \mathbf{a}(t) &= [\exp(-2j\pi f_1 t)w(f_1) \exp(-2j\pi f_2 t)w(f_2) \dots \exp(-2j\pi f_N t)w(f_N)]^T \\ &= \text{diag}\{w(f_1), w(f_2) \dots w(f_N)\} [\exp(-2j\pi f_1 t), \exp(-2j\pi f_2 t) \dots \exp(-2j\pi f_N t)]^T \\ &= \mathbf{C}\bar{\mathbf{a}} \end{aligned}$$

The frequency behaviour  $w(f)$  depends on the RMS height  $\sigma_h$  and the correlation length  $L_h$ , thus matrix  $\mathbf{C}$  also changes with  $\sigma_h$  and  $L_c$ ; it may then be expressed as  $\mathbf{C}(\sigma_h, L_c)$ . We propose to interpolate  $w(f)$  into a uniform linear frequency behaviour. The procedure is presented as follows:

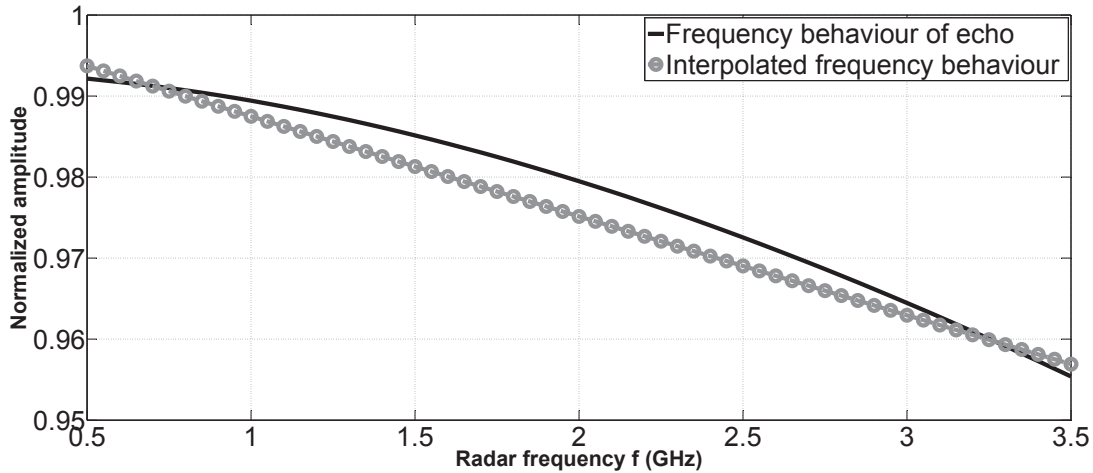


Figure 5.3: Linear interpolation on frequency behaviour  $w(f)$

- Define a set of  $\sigma_h = \{\sigma_{h1}, \sigma_{h2} \dots \sigma_{hG}\}$  and  $L_h = \{L_{c1}, L_{c2} \dots L_{cP}\}$ ;
- Compute the model vectors associated with the set of  $\sigma_h$  and  $L_c$ , and arrange them in a matrix form as follows:  

$$\mathbf{C}_r = [\mathbf{C}(\sigma_{h1}, L_{c1}) \mathbf{C}(\sigma_{h1}, L_{c2}) \dots \mathbf{C}(\sigma_{h1}, L_{cP}) \mathbf{C}(\sigma_{h2}, L_{c1}) \dots \mathbf{C}(\sigma_{hG}, L_{cP})],$$
 $\mathbf{C}_r$  is called the array manifold of the real array;
- Make an interpolation on the frequency behaviour  $w(f)$ . Thus, the interpolated frequency behaviour can be  $\hat{w}(f) = e^{\frac{\ln\{w(f_N)/w(f_1)\}}{f_N - f_1} f}$ ; Fig. 5.3 gives an example of interpolation of the frequency behaviour  $w(f)$ .

Then, place the “virtual elements  $\hat{w}(f)$ ” of the interpolated matrix:

$$\mathbf{C}_v = [\hat{\mathbf{C}}(\sigma_{h1}, L_{c1}) \hat{\mathbf{C}}(\sigma_{h1}, L_{c2}) \dots \hat{\mathbf{C}}(\sigma_{h1}, L_{cP}) \hat{\mathbf{C}}(\sigma_{h2}, L_{c1}) \dots \hat{\mathbf{C}}(\sigma_{hG}, L_{cP})].$$

$\hat{\mathbf{C}} = \hat{\mathbf{C}}(\sigma_h, L_c) = \text{diag}\{\hat{w}(f_1), \hat{w}(f_2) \dots \hat{w}(f_N)\}$  and  $\hat{\mathbf{C}}$  has a uniformly linear frequency behaviour.

- Find the transformation matrix  $\mathbf{B}$  by a least squares solution of  $\mathbf{B}\mathbf{C}_r = \mathbf{C}_v$ . The “best” interpolation matrix  $\mathbf{C}_v$  is the one which minimizes  $\|\mathbf{B}\mathbf{C}_r - \mathbf{C}_v\|^2$ .

After the interpolation, a new covariance matrix can be written as follows:

$$\bar{\mathbf{R}} = \mathbf{B}\mathbf{A}\mathbf{S}\mathbf{A}^H\mathbf{B}^H + \sigma^2\mathbf{B}\mathbf{\Sigma}\mathbf{B}^H \quad (5.11)$$

where  $\mathbf{B}$  is the transformation matrix of interpolation. In the following subsection, a modified MUSIC algorithm is proposed and applied for the time delay estimation. This algorithm supposes that the noise is a Gaussian white noise. To ensure this condition, like in [58], the noise covariance matrix must be removed. As the radar pulse (measured by the echo backscattered from a metallic plane) and the transformation matrix  $\mathbf{B}$  are known, and the noise variance  $\sigma^2$  is estimated, the new noise-free covariance matrix  $\mathbf{R}$  can be written as follows:

$$\mathbf{R} = \mathbf{B}\mathbf{A}\mathbf{S}\mathbf{A}^H\mathbf{B}^H + 0 \times \mathbf{I} \approx \bar{\mathbf{R}} - \hat{\sigma}^2\mathbf{B}\mathbf{\Sigma}\mathbf{B}^H \quad (5.12)$$

where  $\hat{\sigma}^2$  is the estimated noise variance. Then, the SSP technique can be applied (see Chapter 2).

### 5.3.2 Minimum eigenvalue search by modified MUSIC

When the interface roughness is taken into account, high resolution methods like MUSIC or ESPRIT cannot be used directly in theory, due to the unknown frequency behaviour  $w(f)$  of echoes. Therefore, we propose a modified MUSIC algorithm to estimate first the time delays, and then the interface roughness.

In this section, a modified MUSIC algorithm is proposed, which allows estimating only the time delays. The mode vector  $\mathbf{a}$  can be written as follows:

$$\begin{aligned} \mathbf{a}(t) &= [\exp(-2j\pi f_1 t)\hat{w}(f_1) \exp(-2j\pi f_2 t)\hat{w}(f_2) \\ &\quad \dots \exp(-2j\pi f_L t)\hat{w}(f_L)]^T \\ &= \text{diag}\{\exp(-2j\pi f_1 t), \exp(-2j\pi f_2 t) \dots, \exp(-2j\pi f_L t)\} \\ &\quad [\hat{w}(f_1)\hat{w}(f_2) \dots \hat{w}(f_L)]^T \\ &= \hat{\mathbf{A}}\mathbf{k} \end{aligned}$$

where  $\hat{\mathbf{A}} = \text{diag}\{\exp(-2j\pi f_1 t), \exp(-2j\pi f_2 t), \dots, \exp(-2j\pi f_L t)\}$  and  $\mathbf{k} = [\hat{w}(f_1)$

$\hat{w}(f_2) \dots \hat{w}(f_L)]^T$  with  $\hat{w}(f)$  the frequency behaviour of backscattered echoes after interpolation.  $\mathbf{k}$  is a real vector.

The MUSIC pseudo-spectrum can be written as:

$$P(t) = [\min_k \left\{ \frac{\mathbf{k}^H \hat{\mathbf{A}}^H \mathbf{U}_N \mathbf{U}_N^H \hat{\mathbf{A}} \mathbf{k}}{\mathbf{k}^H \hat{\mathbf{A}}^H \hat{\mathbf{A}} \mathbf{k}} \right\}]^{-1} \quad (5.13)$$

where  $\mathbf{U}_N$  is the  $L \times (L-d)$  noise matrix whose columns are the  $L-d$  noise eigenvectors. Referring to [59],  $P(t)$  is equal to the minimum generalized eigenvalue  $\lambda_{\min}$  of  $\hat{\mathbf{A}}^H \mathbf{U}_N \mathbf{U}_N^H \hat{\mathbf{A}}$  and  $\hat{\mathbf{A}}^H \hat{\mathbf{A}}$ , satisfying (with  $\mathbf{k}_{\min}$  the corresponding generalized eigenvector):

$$\hat{\mathbf{A}}^H \mathbf{U}_N \mathbf{U}_N^H \hat{\mathbf{A}} \mathbf{k}_{\min} = \lambda_{\min} \hat{\mathbf{A}}^H \hat{\mathbf{A}} \mathbf{k}_{\min} = \lambda_{\min} \mathbf{k}_{\min} \quad (5.14)$$

The pseudo-spectrum of MUSIC can also be written as the reciprocal of the minimum eigenvalue of  $\text{real}\{\hat{\mathbf{A}}^H \mathbf{U}_N \mathbf{U}_N^H \hat{\mathbf{A}}\}$  [59, 60]:

$$P(t) = \frac{1}{\lambda_{\min}(t)} \quad (5.15)$$

By using (5.15), we only need to search the spectrum in the time domain without knowing the influence of frequency behaviour. However, it has a false peak in the middle of two true values. For example, when two echoes are considered, if we assume that  $t_1$  and  $t_2$  ( $t_2 > t_1$ ) are the time delays of the echoes, we can prove that  $t_3 = \frac{t_2 - t_1}{2}$  is also a solution of  $\lambda_{\min}(t) = 0$ . The proof is shown in Appendix B. In [60], based on the characteristics of  $\lambda_{\min}(t)$  corresponding to the false time delay and the true time delays, a new pseudo-spectrum of MUSIC is proposed to cancel the false time delay, which can be expressed as:

$$P(t) = \frac{\lambda_2(t)}{\lambda_1(t)} \quad (5.16)$$

where  $\lambda_k(t)$  is the  $k$ th eigenvalue of  $\text{real}\{\hat{\mathbf{A}}^H \mathbf{U}_N \mathbf{U}_N^H \hat{\mathbf{A}}\}$ , and  $\lambda_L(t) \geq \lambda_{L-1}(t) \geq \dots \geq \lambda_1(t)$ . Nevertheless, the above method only works for the case of two echoes. For the case where the number of echoes is superior to 2, Eq. (5.16) does not work. For example, when a true time delay has the same value as a false delay, this true time delay will also be cancelled. In Appendix B, we show that the number of zero eigenvalues of  $\text{real}\{\hat{\mathbf{A}}^H \mathbf{U}_N \mathbf{U}_N^H \hat{\mathbf{A}}\}$  corresponding to the true time delay is odd and the number corresponding to the false time delay is even. Based on the above characteristics, we

propose a generalized pseudo-spectrum for modified MUSIC:

$$P(t) = \begin{cases} \frac{\lambda_2(t)}{\lambda_1(t)} \frac{\lambda_4(t)}{\lambda_3(t)} \cdots \frac{\lambda_{L-1}(t)}{\lambda_{L-2}(t)} & L = 2n + 1 \\ \frac{\lambda_2(t)}{\lambda_1(t)} \frac{\lambda_4(t)}{\lambda_3(t)} \cdots \frac{\lambda_L(t)}{\lambda_{L-1}(t)} & L = 2n \end{cases} \quad (5.17)$$

where  $n = 1, 2, \dots$  and  $L$  can be odd or even numbers. The MUSIC pseudo-spectrum

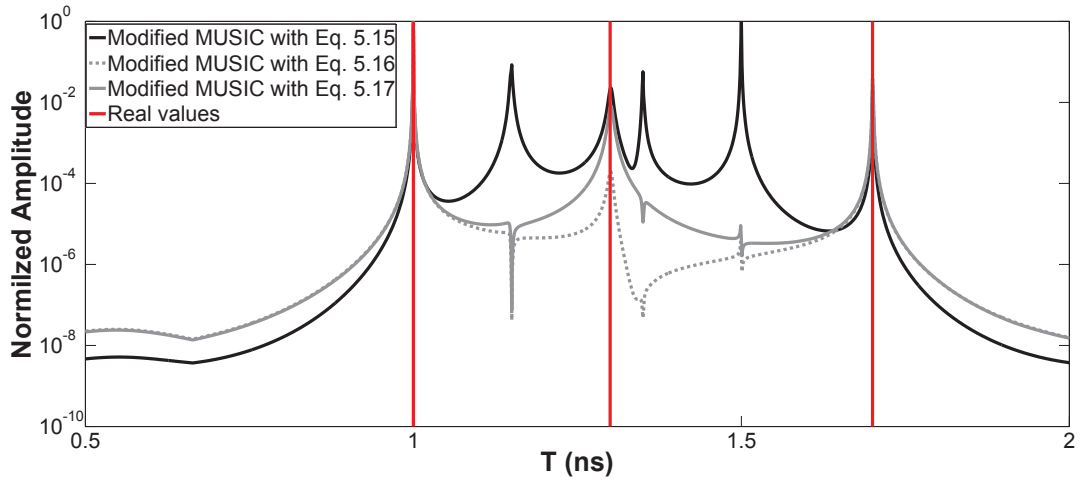


Figure 5.4: MUSIC pseudo-spectrum for TDE with SNR=30 dB and time delays 1 ns, 1.3 ns and 1.7 ns

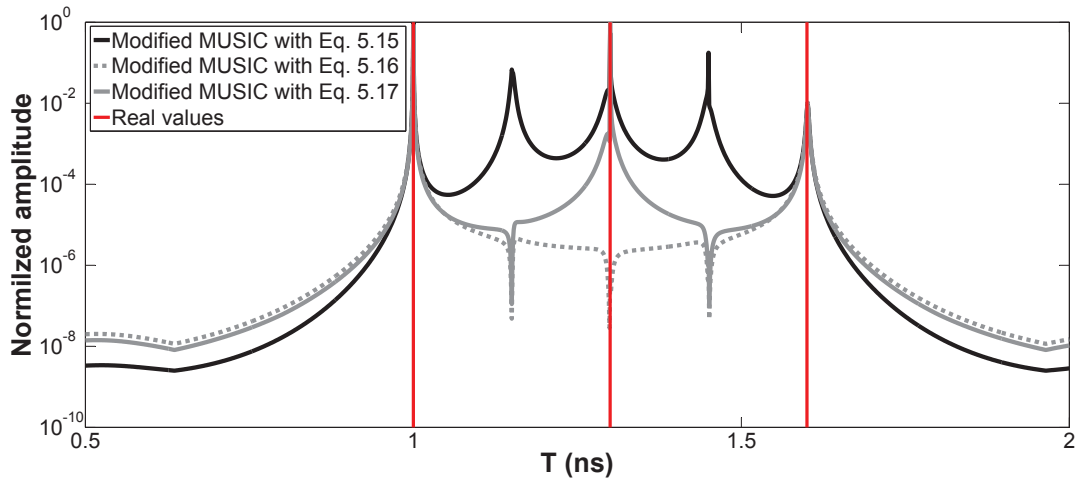


Figure 5.5: MUSIC pseudo-spectrum for TDE with SNR=30 dB and time delays 1 ns, 1.3 ns and 1.6 ns

in Eqs. (5.15), (5.16) and (5.17) are shown in Figs. 5.4 and 5.5. In order to make a better comparison between the three pseudo-spectrum, an amplitude normalization

is made in Figs. 5.4 and 5.5. In Fig. 5.4, 3 time delays (1 ns, 1.3 ns and 1.7 ns) are considered. The modified MUSIC with Eq. (5.15) obtains three false peaks at 1.15 ns, 1.35 ns and 1.5 ns. By using the modified MUSIC with Eq. (5.16) and the modified MUSIC with Eq. (5.17), the three false peaks are removed. In Fig. 5.5, we also consider 3 time delays (1 ns, 1.3 ns and 1.6 ns), but the second time delay is in the middle of the other two time delays. The modified MUSIC with Eq. (5.15) obtains two false peaks at 1.15 ns and 1.45 ns. By using the modified MUSIC with Eq. (5.16), the two false peaks are removed, but also the second time delay. Only the proposed modified MUSIC with Eq. (5.17) can successfully remove the false time delays and keep the true time delays. Thus, in the following, Eq. (5.17) is used as the pseudo-spectrum of the modified MUSIC.

### 5.3.3 Interface roughness estimation

When the time delays are calculated, we propose two ways to calculate the interface roughness. The first one is to use the MLE to estimate the roughness parameters of each interface. Another way is to use MUSIC algorithm.

#### MLE for interface roughness estimation

For the frequency behaviour of backscattered echoes, it has been mentioned in the previous section that the frequency behaviour  $w(f)$  can be approximated by a Gaussian or a mixed function for UWB radar. It enables a parametrization of the frequency variations for data modelling. We assume that the frequency behaviour can be expressed as  $w_k(f_i) = \exp(-b_k f_i^2)$  or  $w_k(f_i) = \exp(-b_k f_i^2 - c_k f_i)$ , where  $b_k$  and  $c_k$  are the roughness parameters of the  $k$ th interface. For flat interfaces,  $b_k = c_k = 0$ . These parameters can be calculated by the MLE with estimated time delays.

#### MUSIC for interface roughness estimation

The frequency behaviour of backscattered echoes can also be calculated from associated eigenvectors of the estimated time delays by using Eq. (5.13):

$$P = [\min_{\mathbf{k}} \left\{ \frac{\mathbf{k}^H \hat{\mathbf{A}}^H(\hat{t}) \mathbf{U}_N \mathbf{U}_N^H \hat{\mathbf{A}}(\hat{t}) \mathbf{k}}{\mathbf{k}^H \hat{\mathbf{A}}^H(\hat{t}) \hat{\mathbf{A}}(\hat{t}) \mathbf{k}} \right\}]^{-1}$$

$\mathbf{k}_{min}$  is a vector whose elements contain the information of the frequency behaviour after interpolation. After calculating the vector  $\mathbf{k}_{min}$ , the estimated frequency behaviour of the backscattered echoes is  $\mathbf{B}^{-1} \mathbf{k}_{min}$ ,  $\mathbf{B}$  being a transformation matrix of interpolation.

## 5.4 Performance evaluation

In this section, we present the simulation results of the modified MUSIC for the time delays and interface roughness estimations. Three simulations are made in the following: the first simulation is to estimate the time delays and interface roughness from various pavements with different roughness; the second simulation evaluates the performance of the modified MUSIC by calculating RRMSE variations on the estimated time delay versus SNR; in addition, in the third simulation, we extend the studied media into a pavement made up of 3 rough interfaces.

### 5.4.1 Simulation parameters

In the simulations, the performance of the modified MUSIC is tested on the data provided by PILE method. The simulated data represent the radar backscattered signal at nadir from a rough pavement made up of two rough interfaces separating homogeneous media. The studied pavement structure is made up of a layer of UTAS with relative permittivity equal to 4.5 overlying a base band with relative permittivity equal to 7. The thickness of the first layer is approximately 20 mm and the second layer is of infinite thickness.

In the first simulation, five pavements are studied (the rough interfaces are assumed to have a Gaussian height probability density function and an exponential height autocorrelation function) [61, 62] with different root mean square heights  $\sigma_h$ , correlation lengths  $L_h$  and conductivities of the layers  $\delta$ :

- case 1:  $\sigma_{hA} = 0.5$  mm,  $L_{cA} = 6.4$  mm,  $\sigma_{hB} = 1.0$  mm,  $L_{cB} = 15$  mm, lossless media;
- case 2:  $\sigma_{hA} = 1.0$  mm,  $L_{cA} = 6.4$  mm,  $\sigma_{hB} = 2.0$  mm,  $L_{cB} = 15$  mm, lossless media;
- case 3:  $\sigma_{hA} = 1.0$  mm,  $L_{cA} = 6.4$  mm,  $\sigma_{hB} = 2.5$  mm,  $L_{cB} = 15$  mm, lossless media;
- case 4:  $\sigma_{hA} = 1.5$  mm,  $L_{cA} = 6.4$  mm,  $\sigma_{hB} = 3.0$  mm,  $L_{cB} = 15$  mm, lossless media;
- case 5:  $\sigma_{hA} = 1.0$  mm,  $L_{cA} = 6.4$  mm,  $\sigma_{hB} = 2.0$  mm,  $L_{cB} = 15$  mm, low-loss media ( $\delta_A = 5 \times 10^{-3}$  S/m,  $\delta_B = 10^{-2}$  S/m).

When the frequency band is 0.5 – 3.5 GHz, with 0.05 GHz frequency step (61 frequency samples), the echoes are slightly overlapped. When the frequency band is 0.5 – 6.5 GHz, with 0.1 GHz frequency step (61 frequency samples), the echoes are

non-overlapped. The covariance matrix is estimated from 1000 independent snapshots. The interpolation SSP technique is used to reduce the cross-correlation between the echoes; the number of sub-bands ( $M$ ) is equal to 20. The signal-to-noise ratio (SNR) is defined as the ratio between the power of the second echo and the noise variance. In the first simulation, a fixed SNR = 20 dB is used for four different rough pavements. In the second simulation, we evaluate the performance of the proposed modified MUSIC, which is assessed with a Monte-Carlo process of 200 independent runs of the algorithm with independent noise snapshots and by the RRMSE of the evaluated parameter as follows:

$$RRMSE(z) = \frac{\sqrt{\frac{1}{U} \sum_{j=1}^U (\hat{z}_j - z)^2}}{z},$$

where  $\hat{z}_j$  denotes the estimated parameter for the  $j$ th run of the algorithm, and  $z$  the true value. In the simulation, the parameter  $z$  can represent either the first ( $t_1$ ) or the second ( $t_2$ ) time delay. Only case 2 is considered.

In the third simulation, the performance of the proposed method is tested on a pavement which is composed of 3 rough interfaces (four layers). The simulation parameters of the pavement are chosen as follows: the permittivities of the first three layers are  $\varepsilon_{r2} = 4.5$ ,  $\varepsilon_{r3} = 7$  and  $\varepsilon_{r4} = 9$ , respectively. We consider three backscattered echoes corresponding to the first three time delays 1 ns, 1.3 ns and 1.7 ns, which corresponds to a thickness of the second layer as approximately 20 mm, of the third layer as approximately 23 mm, and of the fourth layer as infinite. The roughness parameters of the three rough interfaces are chosen as follows:  $b_1 = 1.60 \times 10^{-3} \text{ GHz}^{-2}$ ,  $b_2 = 1.70 \times 10^{-2} \text{ GHz}^{-2}$  and  $b_3 = 3.00 \times 10^{-2} \text{ GHz}^{-2}$ , which are obtained from the signal model, the MLE is used to estimate the roughness parameters.

## 5.4.2 Simulation results

For the first simulation, Figs. 5.6-5.11 show the pseudo-spectrum of the modified MUSIC. Two peaks corresponding to the time delays of the first two scattered echoes are well estimated. The simulation results demonstrate that the proposed algorithm can handle cases where both echoes are either overlapped or non-overlapped and for either lossless or low-loss media. Table 5.1 gives the results of estimated time delays ( $\hat{t}_k$ ). After the time delays are estimated, the next step is to estimate the interface roughness. The interface roughness can be determined by the frequency behaviour of the backscattered echoes. Thus, to estimate the interface roughness is equivalent to

Parameter	$\hat{t}_1$	$\hat{t}_2$
case 1 overlapped	1.000 ns	1.300 ns
case 2 overlapped	0.999 ns	1.303 ns
case 3 overlapped	0.998 ns	1.304 ns
case 4 overlapped	0.996 ns	1.307 ns
case 5 overlapped	1.000 ns	1.306 ns
case 2 non-overlapped	1.000 ns	1.301 ns

Table 5.1: Estimated time delays by modified MUSIC,  $\hat{t}_k$  representing the estimated time delays

estimate the frequency behaviour. We compare the estimated frequency behaviours with the data from PILE in Figs. 5.12-5.17. From the frequency behaviour of the five different cases, it is shown that the expressions of the echoes are in agreement with the data from PILE for various roughness parameters with either lossless or low-loss media.

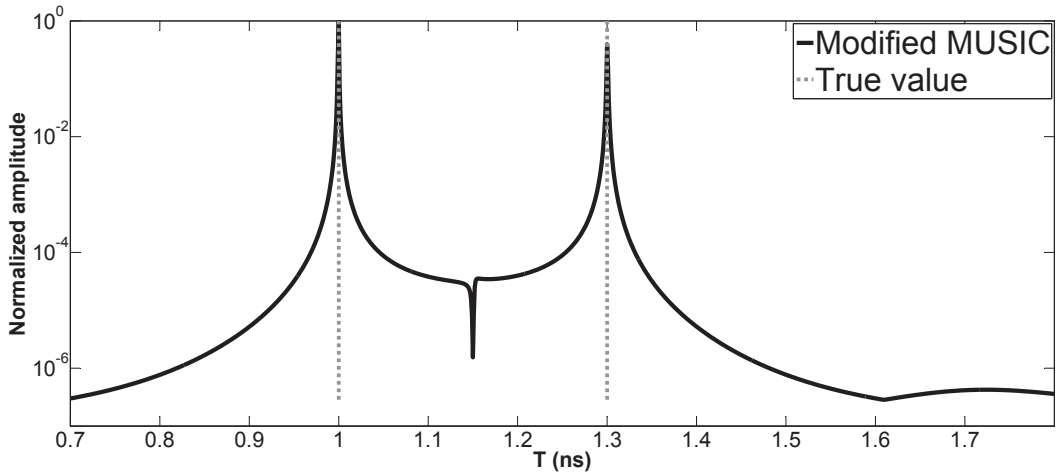


Figure 5.6: Case 1: Pseudo-spectrum of MUSIC for TDE with SNR=20 dB, the two time delays being 1 ns and 1.3 ns (represented in black dashed line), slightly overlapped,  $B = 3.0$  GHz

In the second simulation, we only consider case 2. Fig. 5.18 plots the RRMSE on the estimated time delays versus SNR for case 2. As expected, it can be seen that the RRMSE is continuously decreasing when SNR increases. Fig. 5.18 shows that the proposed modified MUSIC gives a relatively good performance in TDE.

In the third simulation, Figs. 5.19 and 5.20 present the pseudo-spectrum of the modified MUSIC and the frequency behaviour of backscattered echoes for a rough pavement with 3 layers estimated by MLE. It can be seen that the three peaks cor-

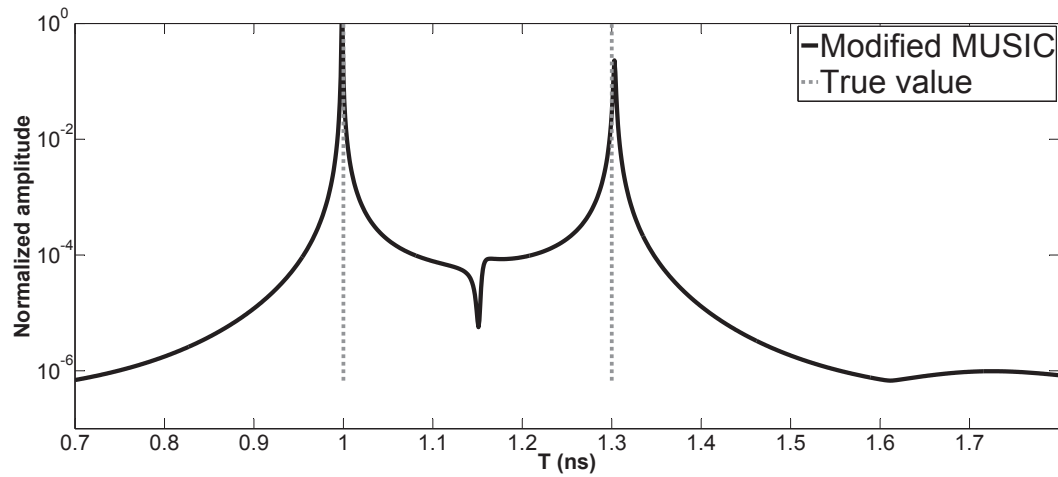


Figure 5.7: Case 2: Pseudo-spectrum of MUSIC for TDE with SNR=20 dB, the two time delays being 1 ns and 1.3 ns (represented in black dashed line), slightly overlapped,  $B = 3.0$  GHz

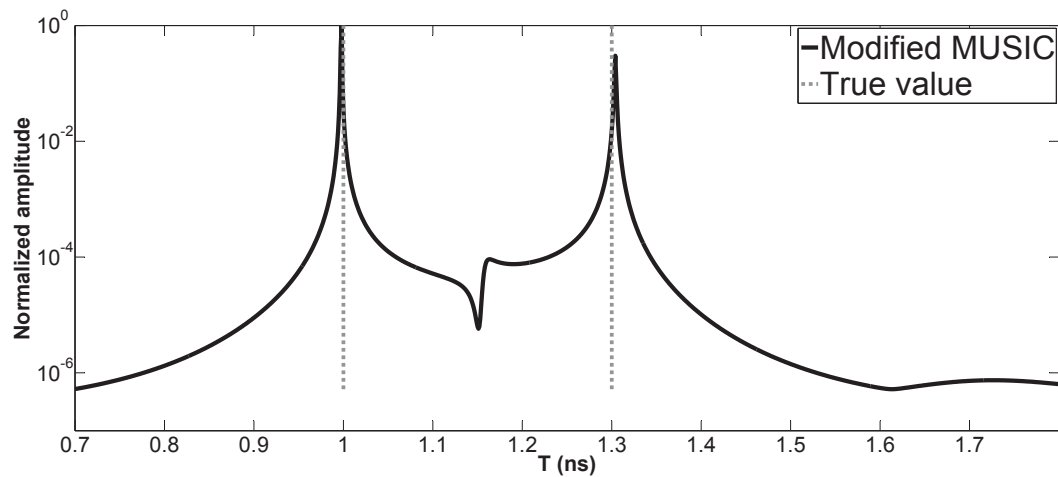


Figure 5.8: Case 3: Pseudo-spectrum of MUSIC for TDE with SNR=20 dB, the two time delays being 1 ns and 1.3 ns (represented in black dashed line), slightly overlapped,  $B = 3.0$  GHz

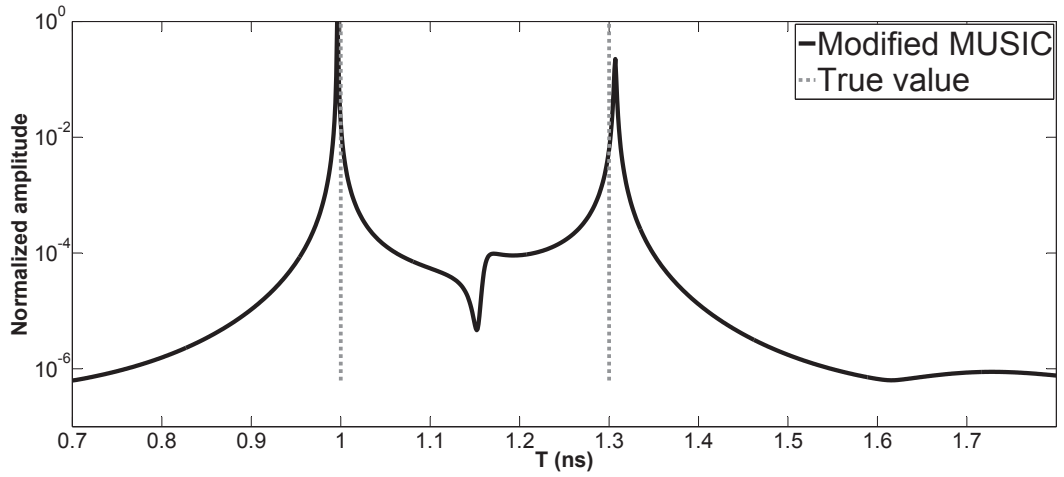


Figure 5.9: Case 4: Pseudo-spectrum of MUSIC for TDE with SNR=20 dB, the two time delays being 1 ns and 1.3 ns (represented in black dashed line), slightly overlapped,  $B = 3.0$  GHz

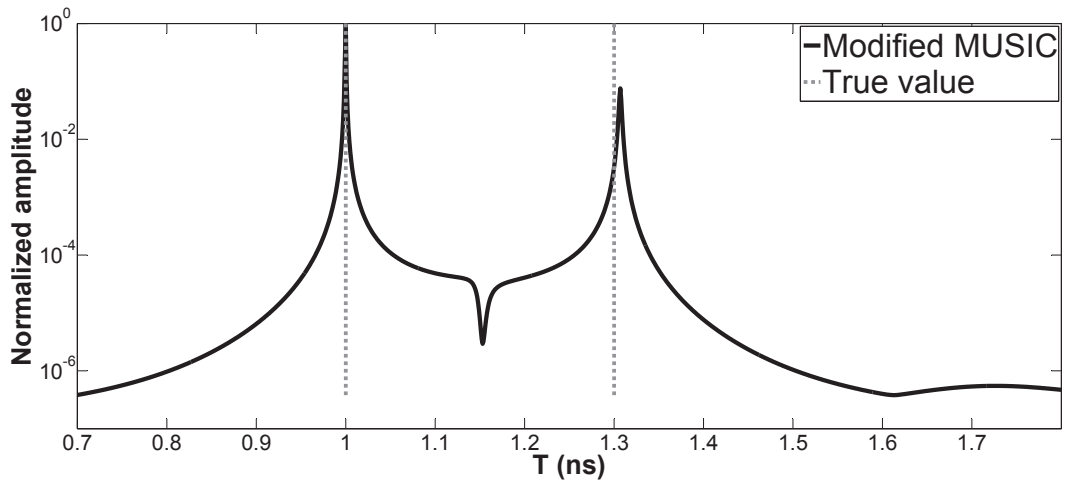


Figure 5.10: Case 5: Pseudo-spectrum of MUSIC for TDE with SNR=20 dB, the two time delays being 1 ns and 1.3 ns (represented in black dashed line), slightly overlapped,  $B = 3.0$  GHz

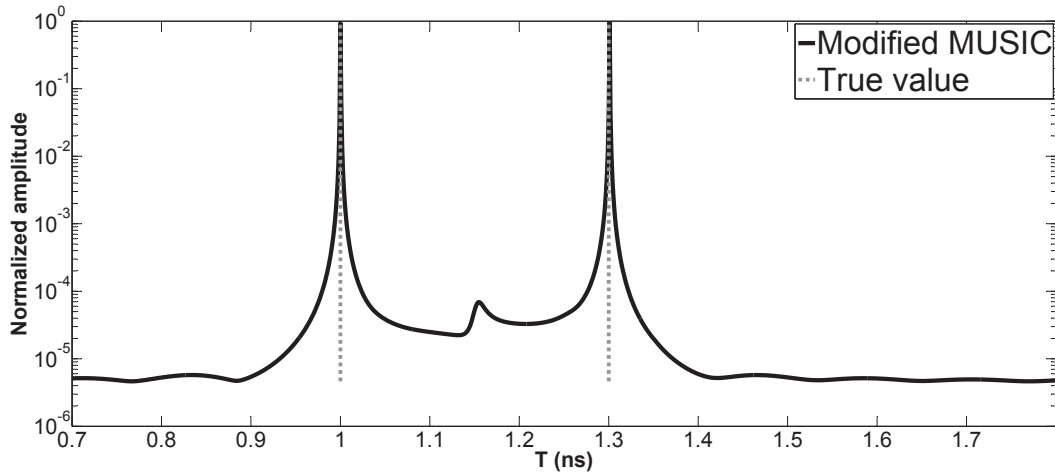


Figure 5.11: Case 2: Pseudo-spectrum of MUSIC for TDE with SNR=20 dB, the two time delays being 1 ns and 1.3 ns (represented in black dashed line), non-overlapped,  $B = 6.0$  GHz

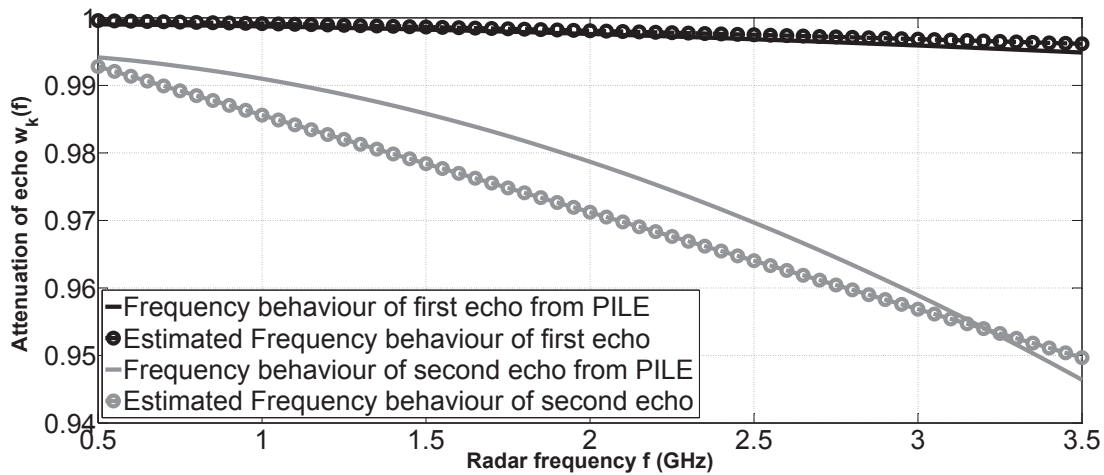


Figure 5.12: Case 1: Expression of the frequency behaviour of backscattered echoes by using the estimated roughness parameter versus the frequency behaviour of backscattered echoes from radar data, slightly overlapped

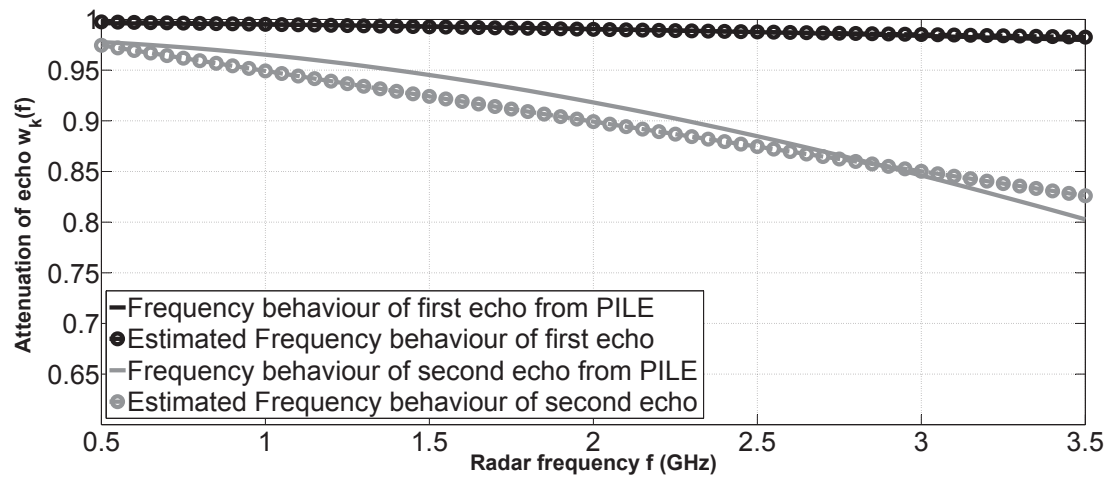


Figure 5.13: Case 2: Expression of the frequency behaviour of backscattered echoes by using the estimated roughness parameter versus the frequency behaviour of backscattered echoes from radar data, slightly overlapped

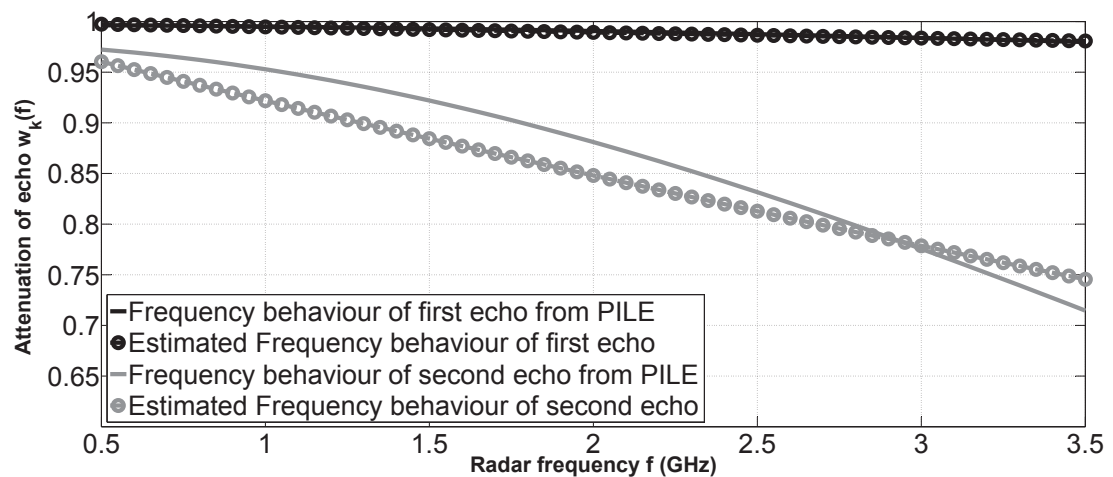


Figure 5.14: Case 3: Expression of the frequency behaviour of backscattered echoes by using the estimated roughness parameter versus the frequency behaviour of backscattered echoes from radar data, slightly overlapped

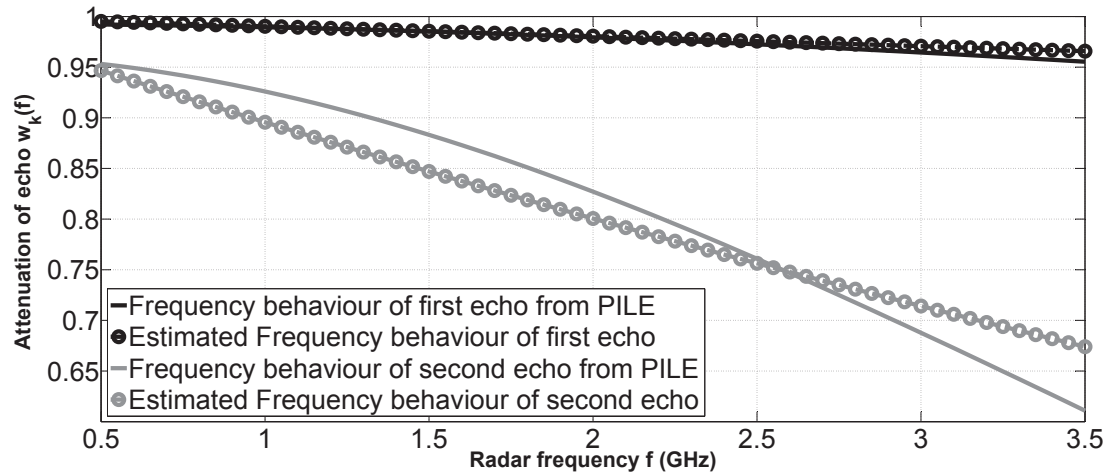


Figure 5.15: Case 4: Expression of the frequency behaviour of backscattered echoes by using the estimated roughness parameter versus the frequency behaviour of backscattered echoes from radar data, slightly overlapped

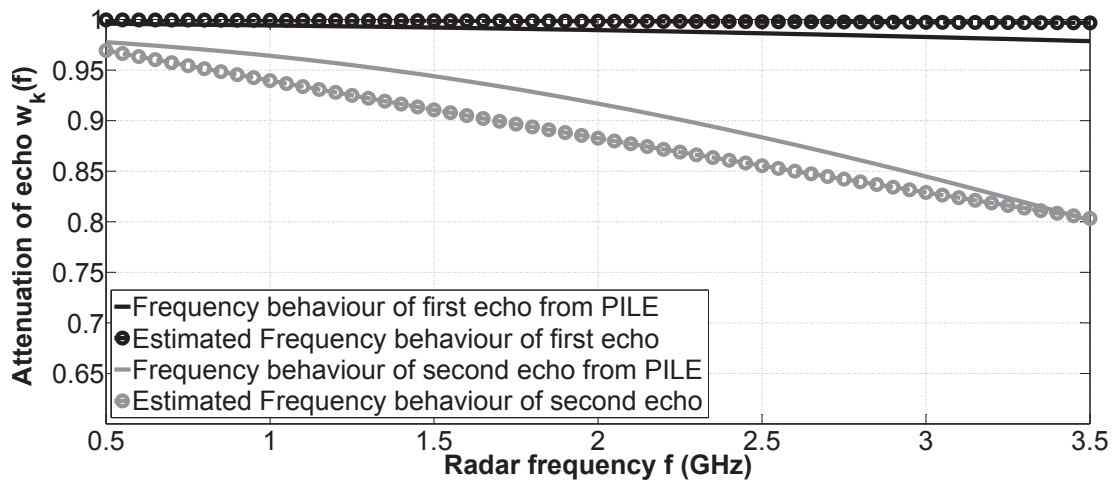


Figure 5.16: Case 5: Expression of the frequency behaviour of backscattered echoes by using the estimated roughness parameter versus the frequency behaviour of backscattered echoes from radar data, slightly overlapped

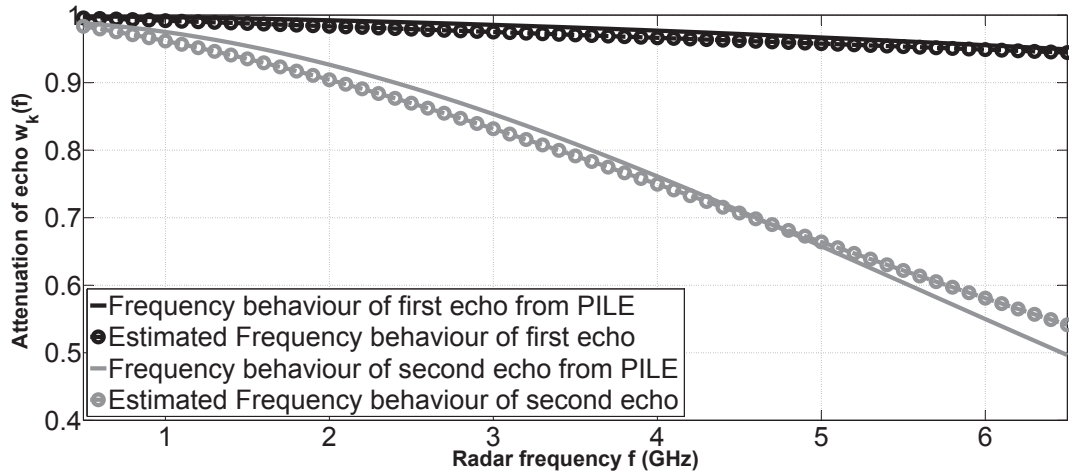


Figure 5.17: Case 2: Expression of the frequency behaviour of backscattered echoes by using the estimated roughness parameter versus the frequency behaviour of backscattered echoes from radar data, non-overlapped

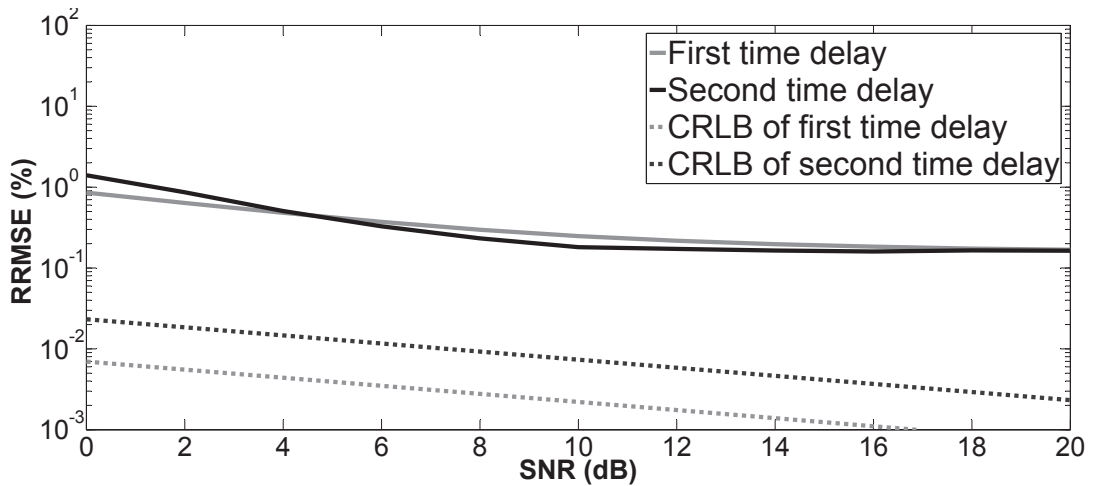


Figure 5.18: Simulation 2, RRMSE on the estimated time delay  $t_k$ , ( $k = 1, 2$ ) versus SNR after 200 Monte-Carlo simulations, slightly overlapped

responding to the time delays of the first three scattered echoes are well estimated (estimated time delays are  $\hat{t}_1 = 0.999$  ns,  $\hat{t}_2 = 1.302$  ns and  $\hat{t}_3 = 1.705$  ns). Furthermore, the estimated frequency behaviours of backscattered echoes are in relatively good agreement with the data from the signal model (estimated roughness parameters are  $\hat{b}_1 = 1.50 \times 10^{-3}$  GHz $^{-2}$ ,  $\hat{b}_2 = 1.83 \times 10^{-2}$  GHz $^{-2}$  and  $\hat{b}_3 = 2.93 \times 10^{-2}$  GHz $^{-2}$ ).

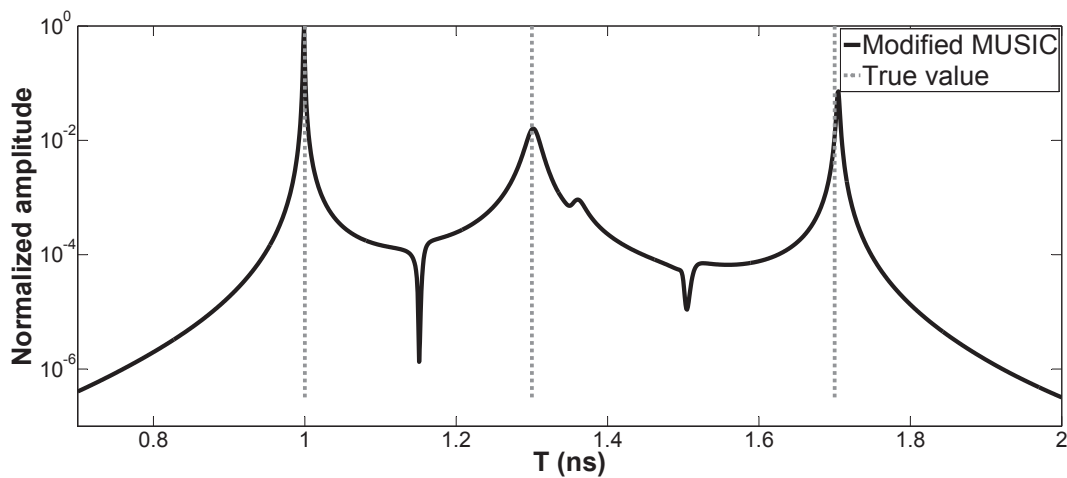


Figure 5.19: Simulation 3: MUSIC pseudo-spectrum for the time delay estimation with SNR=20 dB, the three time delays are 1 ns, 1.3 ns and 1.7 ns (represented in grey dashed line)

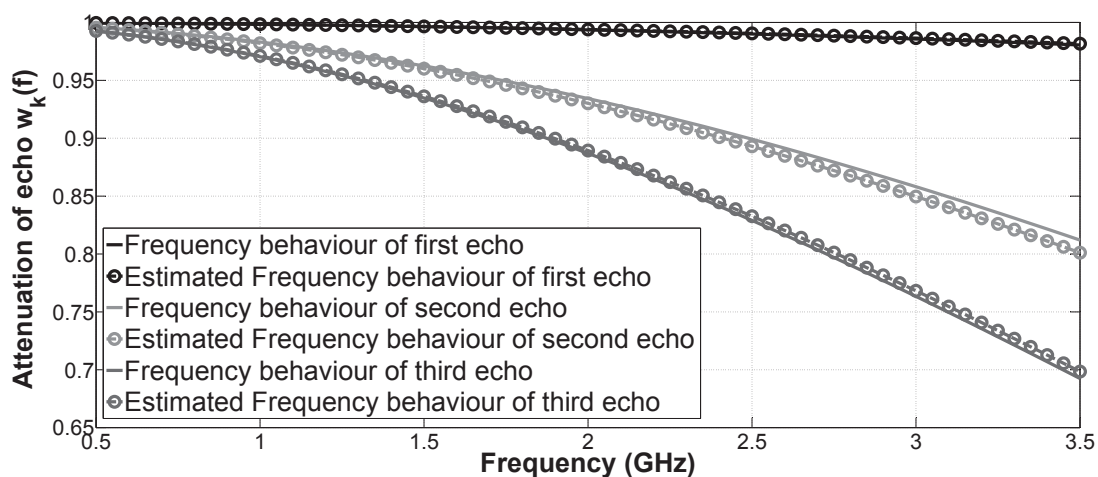


Figure 5.20: Simulation 3: Expression of the frequency behaviour of backscattered echoes by using the estimated roughness parameter versus the frequency behaviour of backscattered echoes from radar data

## 5.5 Conclusion

In the previous chapter, several algorithms have been proposed for the time delays and interface roughness estimation, by using an exponential model. Nevertheless, these algorithms cannot be applied for Gaussian and mixed models. Thus, in this chapter, we presented 2 multi-dimensional search methods: MLE and generalized MUSIC as well as a one dimensional search method: the modified MUSIC. These methods can estimate the time delays and interface roughness estimation with both the Gaussian and the mixed models.

The multi-dimensional search methods can deal with echoes which may be correlated or non-correlated. However, a main drawback is their heavy computational burdens, which is hard to be used in practice. Thus, an one-dimensional search method called the modified MUSIC combined with interpolation spatial smoothing technique is proposed, which has low computational complexity and is able to handle several possible frequency behaviours (more adaptable for UWB GPR).

The performance of the proposed algorithm has been tested on simulated data from PILE with different interface roughnesses. The proposed algorithm shows good performance in terms of the time delays and interface roughness estimation. They can be applied to evaluate the pavement. In the following chapter, we test the performance of the proposed algorithm on the experimental data from GPR.



# Experiments

## 6.1 Introduction

In the previous chapters, algorithms were proposed to estimate the time delays and interface roughness in pavement survey. They have been tested on the simulated data from PILE based on MoM. In order to strengthen the analysis of the proposed algorithms, in this chapter, they are tested on experimental data from GPR. In the narrow frequency band (less than 2 GHz), TDRP-ESPRIT algorithm (proposed in Chapter 4) is applied with the exponential model. In the large frequency band, the modified MUSIC algorithm presented in Chapter 5 is tested with a Gaussian model. In this experiment, a step-frequency GPR is used to measure the thickness and the interface roughness of an UTAS pavement.

### 6.1.1 Experimental device

An UWB step-frequency radar is used in the experiment. It is composed of Vector Network Analyser (VNA) and a bistatic antenna device whose transmitter (Tx) and receiver (Rx) are close to each other with a distance  $d$  approximately 20 cm, see Fig. 6.1. The antennas for both Tx and Rx are of the ETSA A5 antennas [5, 45]. The antennas are about 16.5 cm above the tested pavement, which allows to be in a far-field condition. The radar frequency bandwidth ranges from 1.4 GHz to 15.0 GHz, with

0.017 GHz frequency step (801 frequency samples). By the ability to select multiple frequency band, the experimental settings enable testing the algorithms in situations with resolved and overlapping echoes, respectively.

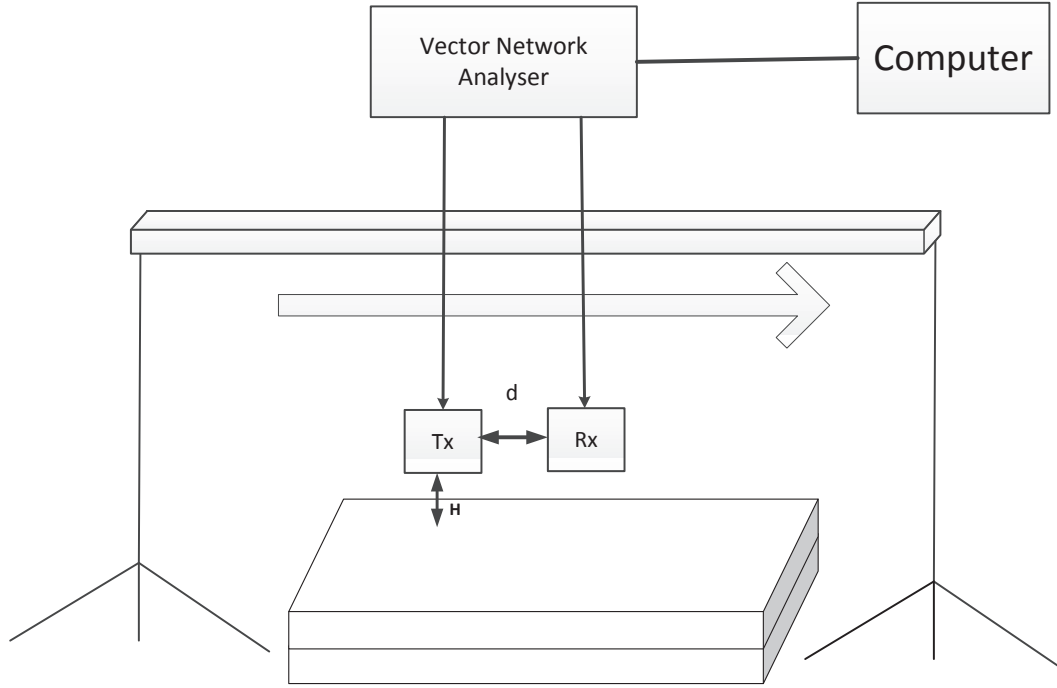


Figure 6.1: Experimental device

### 6.1.2 Studied medium

In the experiment, we study a rough pavement (see Fig. 6.2) made of two rough interfaces separating media, as shown in Fig. 6.3. The studied pavement structure (pavement thickness is about 11 cm) is made of a layer  $\Sigma_A$  overlying a base band  $\Sigma_B$ , which are set on a metallic plane  $\Sigma_C$ . The thickness of the first layer is approximately 4 cm and the second layer is about 7 cm. In order to calculate the permittivities, we have chosen to use the whole frequency bandwidth [1.4, 15] GHz. Then, by using the following equations [8], we can calculate the permittivity of each layer:

$$\varepsilon_2 \approx \left( \frac{1 - s_1}{1 + s_1} \right)^2$$

$$\varepsilon_3 \approx \left( \frac{1 - s_1^2 - s_2}{1 - s_1^2 + s_2} \right)^2$$

where  $\varepsilon_2$  and  $\varepsilon_3$  are the permittivities of the medium  $\Omega_2$  and  $\Omega_3$ , respectively.  $s_k$  is the amplitude of  $k$ th primary echo  $k = 1, 2$ . The permittivities of both materials ( $\Omega_2$  and  $\Omega_3$ ) are calculated in the whole frequency band, with  $\varepsilon_{r2} = 4.94$  and  $\varepsilon_{r2} = 3.97$ . The incident wave with incidence angle  $\theta_i = 31.2^\circ$ , then refraction angles  $\theta_{r1} = 13.5^\circ$  and  $\theta_{r2} = 15.1^\circ$ , respectively ( $\sqrt{\varepsilon_1} \sin \theta_1 = \sqrt{\varepsilon_2} \sin \theta_2$ ). The length of the tested surfaces is about 80 cm with a sample step 4 mm (200 sample points). For each sample point, 10 snapshots are carried out.



Figure 6.2: Studied Pavement

### 6.1.3 Data set

The antenna is moved slightly between various sample points in order to generate independent spatial measurements. Fig. 6.4a and 6.4b display the raw experimental data for both A-scan and B-scan, respectively. The dashed lines represent the envelope of received signals after the Hilbert transformation. The first peak represents the multiple waves as the wave comes from the test bed and the air-wave between the Tx and Rx devices, these waves can be cancelled by a time filter. The second, third and fourth peaks in Figs. 6.4a and 6.4b correspond to the first three backscattered echoes from the first three interfaces. Because of pavement material, the amplitude of second

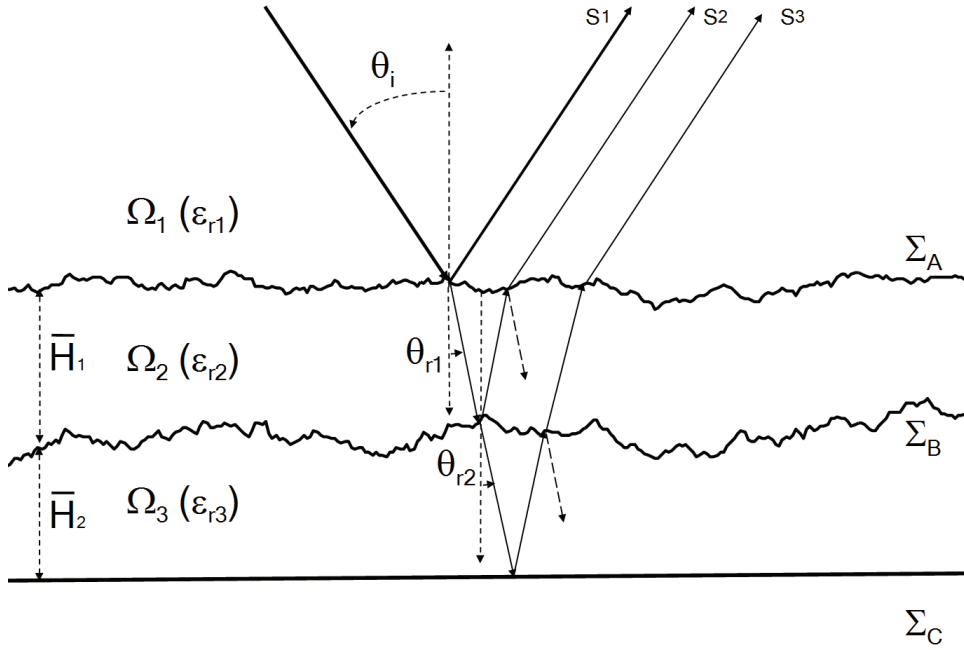


Figure 6.3: Rough Pavement Configuration

echo is much smaller than the first and the third echoes. Indeed, the first and third backscattered echoes are clearly visible in the figures, the second echo is very weak.

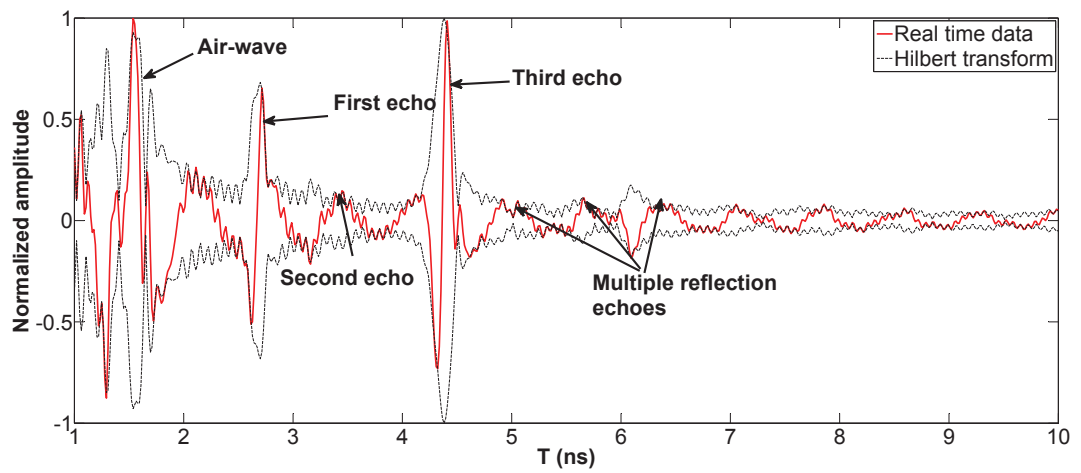
## 6.2 Experimental results

In this section, we present the experimental results of the TDRP-ESPRIT and modified MUSIC combined with MLE for time delays and interface roughness estimations. Before applying the proposed algorithms, three pre-processing techniques are performed on the data.

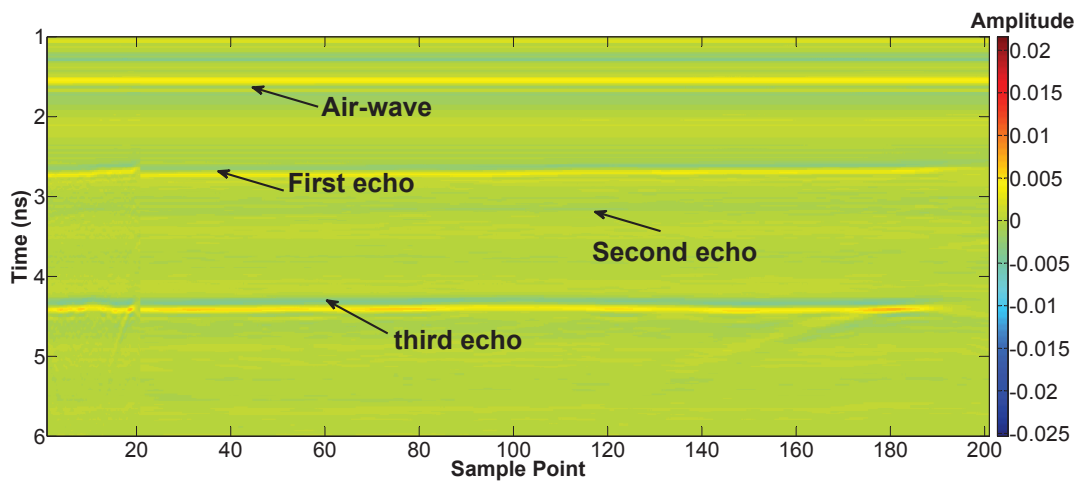
### 6.2.1 Pre-processing of the Data

Three preprocessing techniques are applied before using algorithms: time filtering, data whitening and sub-band averaging.

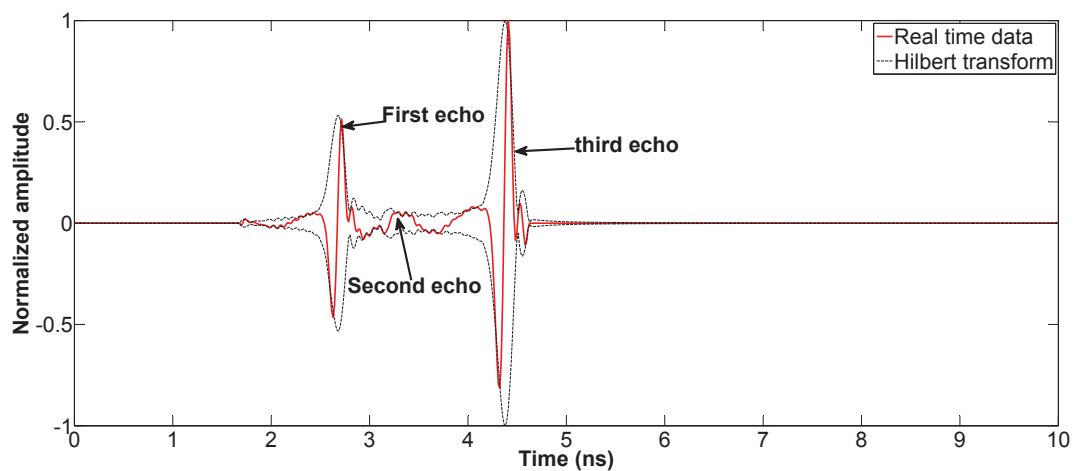
1. Time Filtering. By operating a time filter, three primary backscattered echoes corresponding to the three interfaces are retained. As shown in Fig. 6.4c, the multiple echoes and air wave can be then filtered;



(a) Raw GPR data (A-scan)



(b) Raw GPR data (B-scan)



(c) Time filtered data

Figure 6.4: Preprocessing of backscattered echoes from UTAS where the echoes are non-overlapped,  $B = [1.4, 15]$  GHz

2. Data Whitening. In order to apply the proposed algorithms, a whitening procedure by the pulse is necessary. The radar pulse is measured as the backscattered echo from a metallic plane. The Fig. 6.5 shows the radar pulse at 3 different height from the metal plane.
3. Sub-band averaging. The data covariance matrix has been estimated from a set of 10 snapshots. In our study, the echoes are highly correlated. Thus, we should use SSP to reduce the correlation effect between the backscattered echoes.

After applying these 3 preprocessing techniques, the proposed algorithms are used for the time delays and interface roughness estimation.

In the experiment, two conditions are considered: estimation in a narrow frequency band and in a large frequency band. According to Chapter 3, in a narrow band ( $B < 2$  GHz), the exponential model can be used, the TDRP-ESPRIT proposed in Chapter 4 is applied for time delays and interface roughness estimation. The TDRP-ESPRIT is tested in two different frequency bandwidths  $B = [1.4, 2.76]$  GHz (81 samples) and  $B = [3.1, 4.8]$  GHz (101 samples), the number of sub-bands equals 20. In the large band, the Gaussian model is used. We apply the modified MUSIC in Chapter 5 for estimating the time delays and interface roughness. The algorithm is also tested in two different frequency bandwidths,  $B = [1.4, 6, 5]$  GHz (301 samples) and  $B = [4.8, 8.2]$  GHz (301 samples), with the number of sub-bands equal to 151 and 101, respectively.

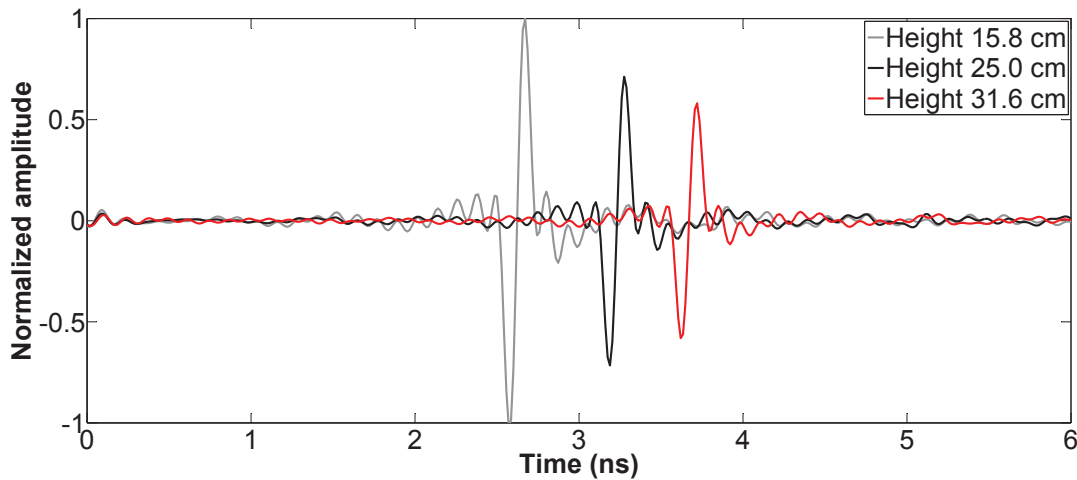


Figure 6.5: Radar pulse measurement,  $B = [1.4, 15]$  GHz

### 6.2.2 Time delay estimation

Table. 6.1 presents estimated time delays of three echoes ( $\widehat{\Delta\tau}_1$  is the time delay between the first and second echoes and  $\widehat{\Delta\tau}_2$  is the time delay between the second and third echoes) by using the TDRP-ESPRIT and modified MUSIC. The layer thickness can be then calculated by following equation:

$$\bar{H}_k = \frac{c\Delta\tau_k \cos \theta_{rk}}{2\sqrt{\varepsilon_r}}$$

where  $\bar{H}_k$  is the thickness of the  $k$ th layer with  $k = 1, 2$ ,  $c$  is the speed of light in vacuum,  $\theta_{rk}$  is the refraction angle and  $\varepsilon_r$  is the permittivity of layer. The estimated layer thickness are also shown in the Table. 6.1. For the TDRP-ESPRIT, when  $B = [1.4, 2.76]$  GHz, the relative errors on estimated layer thickness are 5.25% (first layer) and 11.1% (second layer) respectively; and when  $B = [3.1, 4.8]$  GHz, the relative errors on estimated layer thickness are 9.50% and 6.00%. For the modified MUSIC, when  $B = [1.4, 6.5]$  GHz, the relative errors on estimated layer thickness are 6.50% and 8.00%; and when  $B = [4.8, 8.2]$  GHz, the relative errors on estimated layer thickness are 3.25% and 11.1%. Both of the algorithms give a relatively good performance on thickness estimation with a small bias. The algorithms reveals a bit larger relative error for first layer, one reason is that the second backscattered echo is very weak. Nevertheless, we consider that the proposed algorithms show good performance to estimate the thickness.

### 6.2.3 Interface roughness estimation

Figs. 6.6 – 6.9 show the estimated frequency behaviour by TDRP-ESPRIT in the narrow band. Figs. 6.10 – 6.13 present the estimated frequency behaviour by MLE with modified MUSIC in the large band. From these figures, we can conclude that:

1. The amplitude of echoes decreases with the increase of frequency;
2. The echo amplitude suffers more decrease with larger interface roughness.

The result shows that for the first interface, both algorithms allow the roughness estimation. Nevertheless, the above estimations are not accurate enough especially for the second interface roughness. Indeed, the amplitude of the second echo is very small and the roughness estimation becomes more complex. The amplitude is small due to the reflection on  $\Sigma_B$  is very weak (the material of two layers is similar). Furthermore, for the second echo, the results can change with frequency band and the number of

Method \ Parameter	$\widehat{\Delta\tau}_1$	$\widehat{\Delta\tau}_2$	$\widehat{H}_1$	$\widehat{H}_2$
TDRP-ESPRIT ( $B = [1.4, 2.76]$ GHz)	0.642 ns	1.07 ns	4.21 cm	7.78 cm
TDRP-ESPRIT ( $B = [3.1, 4.8]$ GHz)	0.668 ns	1.02 ns	4.38 cm	7.42 cm
Modified MUSIC ( $B = [1.4, 6.5]$ GHz)	0.650 ns	1.04 ns	4.26 cm	7.56 cm
Modified MUSIC ( $B = [4.8, 8.2]$ GHz)	0.629 ns	1.07 ns	4.13 cm	7.78 cm

Table 6.1: Estimated time delays and thicknesses by the TDRP-ESPRIT and modified MUSIC,  $\widehat{\Delta\tau}_k$  representing the estimated time delay and  $\widehat{H}_k$  representing the estimated thickness

sub-bands that we choose.

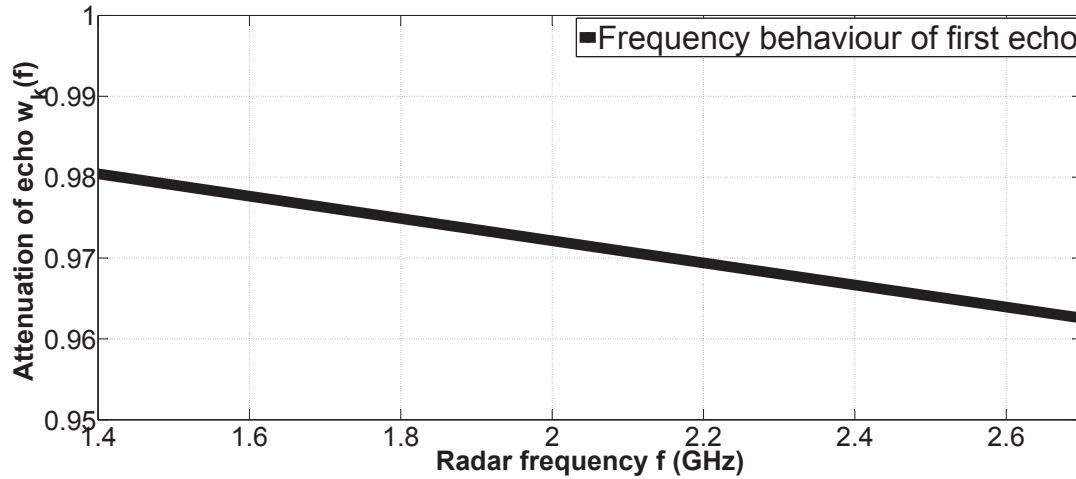


Figure 6.6: Estimated frequency behaviour of first echo by using TDRP-ESPRIT from GPR, slightly overlapped,  $B\Delta\tau = 0.87$ ,  $B = [1.4, 2.76]$  GHz

### 6.3 Conclusion

In the chapter, we present the experimental validation of proposed algorithms (TDRP-ESPRIT and modified MUSIC) by using a step-frequency GPR. By applying preprocessing techniques (time filtering and SSP), the obtained results validated the proposed algorithms. Thus, the proposed algorithms can be applied to road surface layer surveys (for the estimation of thin pavement thickness) by taking the roughness parameter of both interfaces into account. Furthermore, the proposed algorithms can estimate the interface roughness. Nevertheless, because of the small difference between the first two layers (second backscattered echo is very weak), the estimation of the interface roughness becomes complex. The experiment has shown that the proposed algorithms

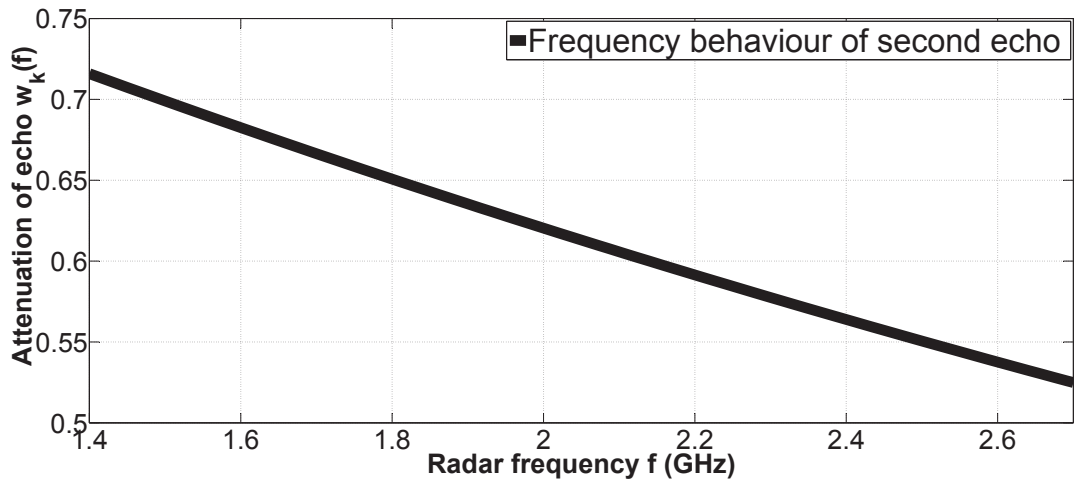


Figure 6.7: Estimated frequency behaviour of second echo by using TDRP-ESPRIT from GPR, slightly overlapped,  $B\Delta\tau = 0.87$ ,  $B = [1.4, 2.76]$  GHz

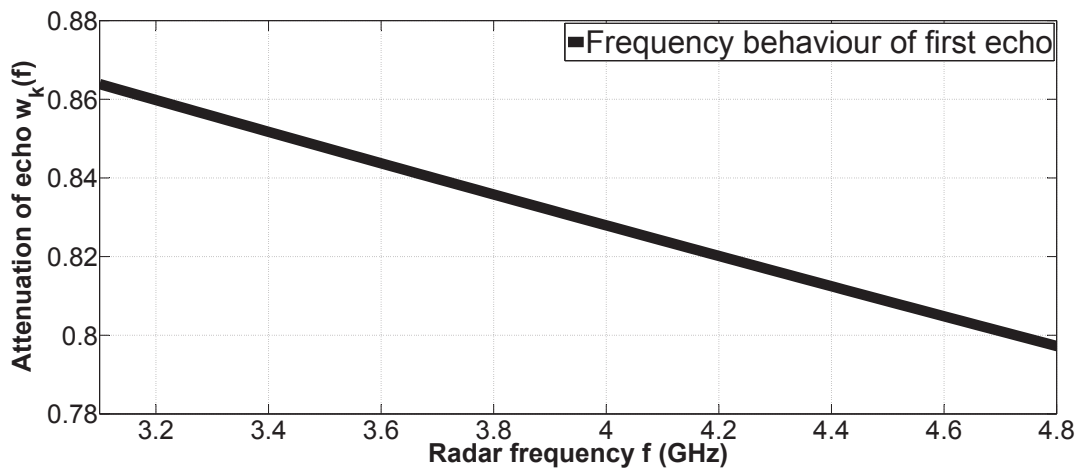


Figure 6.8: Estimated frequency behaviour of first echo by using TDRP-ESPRIT from GPR, slightly overlapped,  $B\Delta\tau = 1.14$ ,  $B = [3.1, 4.8]$  GHz

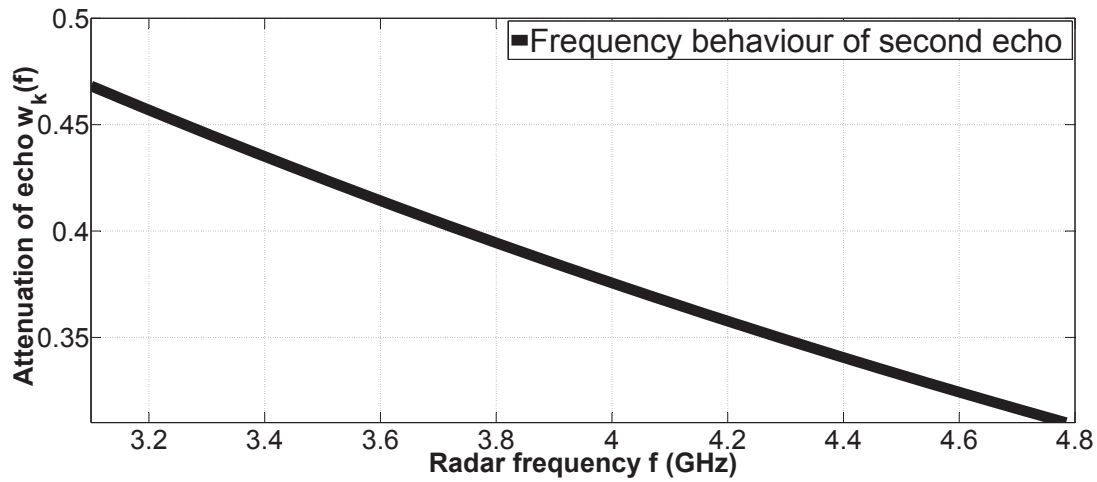


Figure 6.9: Estimated frequency behaviour of second echo by using TDRP-ESPRIT from GPR, slightly overlapped,  $B\Delta\tau = 1.14$ ,  $B = [3.1, 4.8]$  GHz

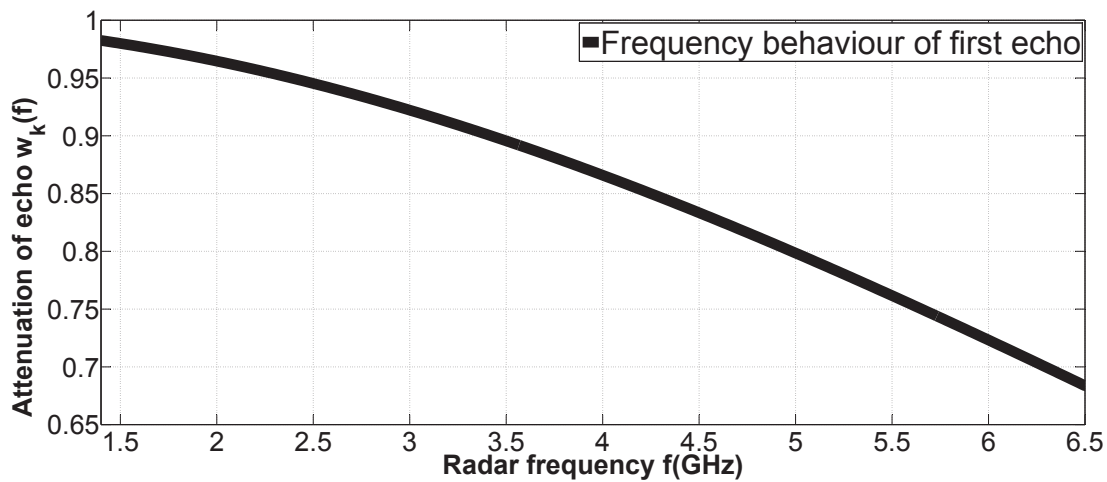


Figure 6.10: Estimated frequency behaviour of first echo by using MLE from GPR, non-overlapped,  $B\Delta\tau = 3.31$ ,  $B = [1.4, 6.5]$  GHz

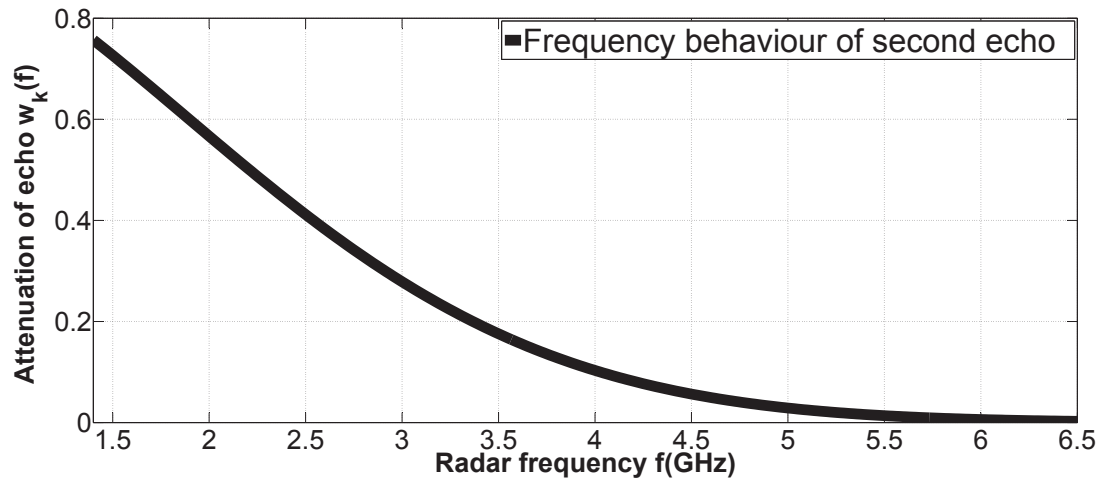


Figure 6.11: Estimated frequency behaviour of second echo by using MLE from GPR, non-overlapped,  $B\Delta\tau = 3.31$ ,  $B = [1.4, 6.5]$  GHz

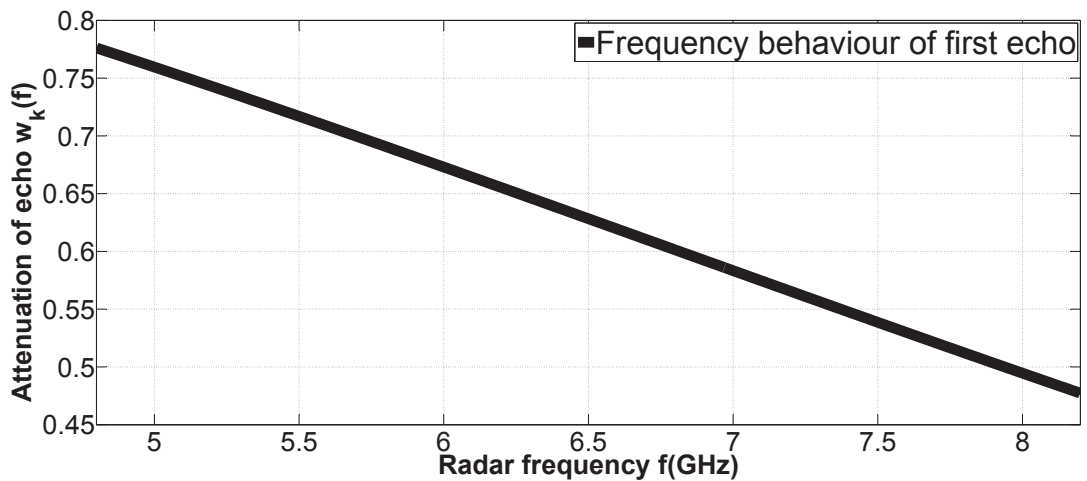


Figure 6.12: Estimated frequency behaviour of first echo by using MLE from GPR, non-overlapped,  $B\Delta\tau = 2.14$ ,  $B = [4.8, 8.2]$  GHz

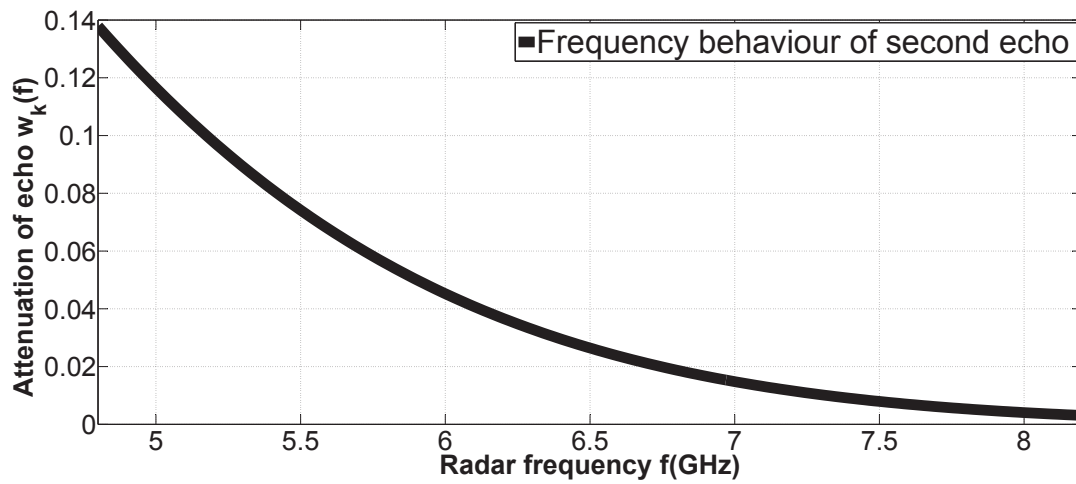


Figure 6.13: Estimated frequency behaviour of second echo by using MLE from GPR, non-overlapped,  $B\Delta\tau = 2.14$ ,  $B = [4.8, 8.2]$  GHz

give good results for TDE and interface roughness. Noting that when the echoes are very small, these algorithms should be improved. In perspective, the interface roughness estimated by proposed algorithms will be compared with the photogrammetry methods.

## Conclusion and perspectives

### 7.1 Conclusion

In the field of civil engineering, GPR is widely used as a NDT method for road pavement surveys, especially for measuring the layer thickness. By assuming the roadway to be horizontally stratified, the layer thicknesses are then deduced from the time-delay of the backscattered echoes associated with each interface and the dielectric constants of the media. In this thesis, the influence of interface roughness is addressed with the ultra-wide band capability of the step-frequency radar technology (and in particular, the upper frequency range, which is up to 8 – 10 GHz). It is proposed to carry out the sensitivity analysis to larger bandwidths (for example, [0.5; 10.5] GHz) in order to deal with existing radar systems. It is expected to bring useful information for monitoring the pavement structure. For layer thickness measurement, it is shown that the interface roughness provides a continuous frequency decay of the magnitude of the echoes. The latter variations can be modelled by some functions and are considered in the scope of the data processing of radar signals. Then, signal processing methods are proposed to estimate the time delay of backscattered echoes and the interface roughness. Finally, the different proposed methods are tested on both simulated data and experimental data from wideband (step-frequency) radar.

The thesis has been divided into 6 main chapters:

Chapter 2 has presented some methods (conventional methods and high resolution

methods) for TDE by using both impulse GPR and step-frequency GPR in order to estimate layer thickness. The conventional methods (IFT and cross-correlation method) are presented. They offer low computational cost, but are unable to detect closely spaced time delays. To solve such problem, high resolution methods are applied. We present three well-known algorithms (MUSIC, root-MUSIC and ESPRIT) combined with sub-band averaging techniques. 4 preprocessing methods have been presented, it can be seen that the proposed two adaptive ISS (with PM) methods are more powerful than the traditional SSP and MSSP. The performance of the high resolution methods with sub-band averaging techniques is tested on various pavement structures, and numerical examples are provided to show the performance of the algorithms.

Chapter 3 briefly recalls the rigorous numerical method PILE for simulating the scattering of EM waves from layered random rough interfaces. As a result, the frequency behaviour of the backscattered echoes is investigated. Magnitude variations are found to prevail on phase variations. Sensitivity of the magnitude of the echoes to interface roughness is studied. It has been shown that the impacts of the interface roughness on the frequency behaviour of backscattered echoes are as follows:

1. The echo amplitude decreases with increasing frequency;
2. The echo amplitude decrease gets stronger for larger surface roughness;
3. The magnitude of the second backscattered echo is more sensitive to the lower interface roughness than to the upper surface roughness.

A curve fitting is made to estimate the parameters of the approximate expression of the echoes. An exponential shape, a Gaussian shape and a mixed shape are proposed to model the frequency variations; Both the mixed model and Gaussian model match well with PILE data in the whole frequency range ([0.5; 10.5] GHz). The exponential model shows a poor performance, expect for a frequency band which is smaller than 2 GHz. The parameter accounting for the frequency variations (by assuming an exponential shape, a Gaussian shape or a mixed shape) called roughness parameter can be estimated by fittings. In the following, this new parameter is taken into accounted in the signal model.

Chapter 4 is devoted to the signal processing techniques which may estimate jointly the time delays and interface roughness. In this chapter, the frequency behaviour of echoes is modelled by the exponential model. A modified 2-D MUSIC, a modified root-MUSIC algorithm, TDRP-ESPRIT algorithm and a modified MPM are then proposed with the interface roughness taken into account in both the data modelling and the processing. The SSP method is used to mitigate the influence of the correlation

magnitude between the backscattered echoes. The performance of the proposed algorithms is tested on different roughness pavements. Simulation results demonstrate that the proposed algorithms give satisfactory performance for estimating the time delays and roughness parameters.

With the widening of the frequency band (for example with a step-frequency radar), the curve fitting error with the exponential model increases rapidly, which may bring errors to the interface roughness estimation. As a consequence, in Chapter 5 we propose to use more realistic but more complex signal models: the Gaussian and mixed models (which are more close to the real data with wide frequency band). When the frequency behaviour of the echoes is modelled by a Gaussian shape or a mixed shape, the complexity of the high resolution methods increases greatly. Indeed, the high resolution methods proposed in Chapter 4 cannot be used directly. Thus, in order to solve the above problems, multi-dimensional search methods (MLE and generalized MUSIC) as well as a one dimensional search method (the modified MUSIC) are proposed for the time delays and interface roughness estimation. The multi-dimensional search methods can be applied on echoes either correlated or non-correlated. However, these methods have heavy computational burdens, they are hard to use in practice. In addition, the modified MUSIC with interpolation spatial smoothing technique is also proposed, which has lower computational complexity. This method is able to handle unknown frequency behaviour. It is more adaptable for ultra-wideband GPR. The proposed algorithms are tested on simulated data from PILE with different interface roughnesses, which give good performances in the time delays and interface roughness estimation.

In Chapter 6, an experiment is made to survey a pavement structure composed of two rough layers: an UTAS and a base layer. In addition, TDRP-ESPRIT and the modified MUSIC combined with MLE are tested for the time delays and interface roughness estimation of this pavement structure.

## 7.2 Perspectives

Based on the current works, future research may be pursued in the following directions:

1. Continue working on the roughness estimation and compare the results with other methods, like the photogrammetry method. Improve the proposed methods to deal with backscattered echoes with small amplitude;

2. Extend the studied media (pavements) to multiple layers, for which both experimental and numerical validations (by GPILÉ) of the proposed algorithms could be pursued;
3. Extend research works to dispersive media (soil, hydraulic concretes). In this case, the data model must be rewritten by taking into account the roughness, time delay and dispersion parameters (Q factor, for example). As a consequence, new signal processing methods must be proposed;
4. Study more realistic signal models and take multiple reflections into account in the data model (GPR real world data include multiple reflections between the layers).



## Curve fitting results of case *a* and case *b* in chapter 3

### Case *a*

For case *a* (with  $\sigma_{hA} = 0.5$  mm,  $\sigma_{hB} = 1.0$  mm), 4 cases are studied, with frequency bands  $f \in [0.5; 1.5]$  GHz,  $f \in [0.5; 2.5]$  GHz,  $f \in [0.5; 6.5]$  GHz,  $f \in [0.5; 10.5]$  GHz. The following figures give the fitting results in different frequency bands. In addition, in order to evaluate the fitting performances, the following table gives RMSE of curve fitting:

Table A.1: Curve fittings results for case *a*

RMSE % ( $s_1/s_2$ ) \ Model	$ s(f)  = s_k \times \exp(-bf)$	$ s(f)  = s_k \times \exp(-bf^2)$	$ s(f)  = s_k \times \exp(-bf^2 - cf)$
Frequency [0.5; 1.5] GHz	$6.68 \times 10^{-3} / 0.0960$	$8.78 \times 10^{-3} / 0.0485$	$1.27 \times 10^{-3} / 6.59 \times 10^{-3}$
[0.5; 2.5] GHz	0.0220/0.286	0.0121/0.0644	$1.55 \times 10^{-3} / 9.55 \times 10^{-3}$
[0.5; 6.5] GHz	0.119/1.81	0.0433/0.103	$7.65 \times 10^{-3} / 0.0268$
[0.5; 10.5] GHz	0.262/4.25	0.0918/0.0890	0.0149 / 0.0504

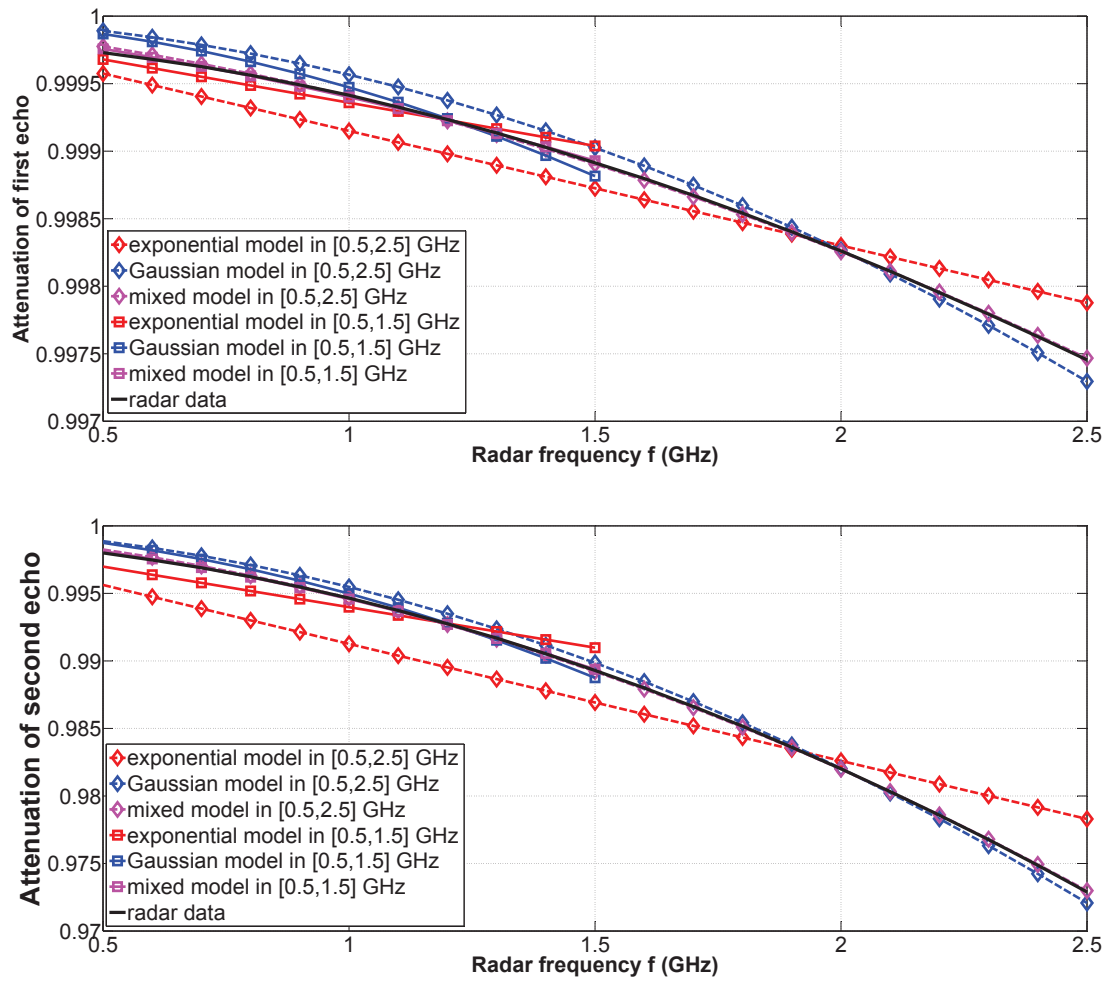


Figure A.1: Case *a*: curve fittings for  $f \in [0.5; 1.5]$  GHz and  $f \in [0.5; 2.5]$  GHz

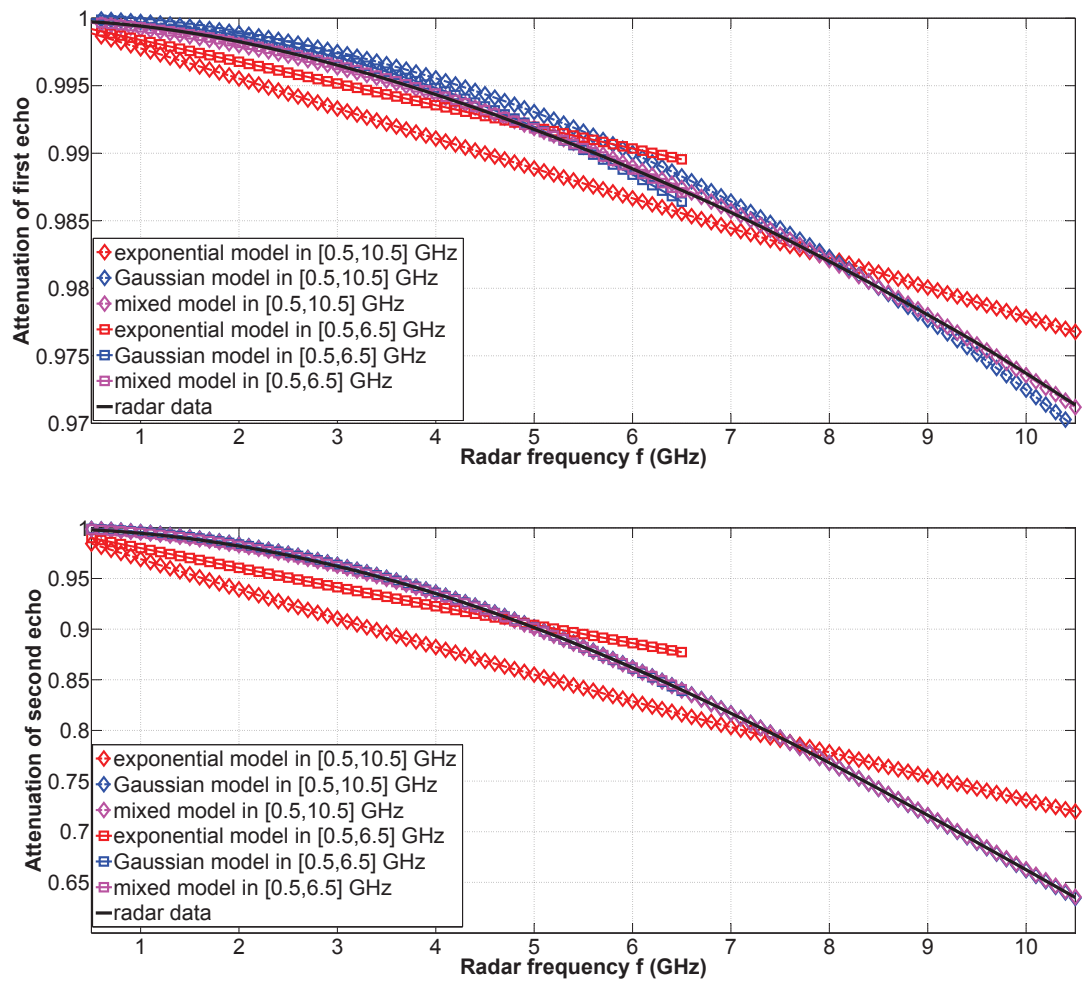


Figure A.2: Case *a*: curve fittings for  $f \in [0.5; 6.5]$  GHz and  $f \in [0.5; 10.5]$  GHz

## Case *b*

For case *b* (with  $\sigma_{hA} = 0.5$  mm,  $\sigma_{hB} = 2.0$  mm), 4 cases are studied, with frequency bands  $f \in [0.5; 1.5]$  GHz,  $f \in [0.5; 2.5]$  GHz,  $f \in [0.5; 6.5]$  GHz,  $f \in [0.5; 10.5]$  GHz. The following figures give the fitting results in different frequency bands. In addition, in order to evaluate the fitting performance, the following table gives RMSE of curve fitting:

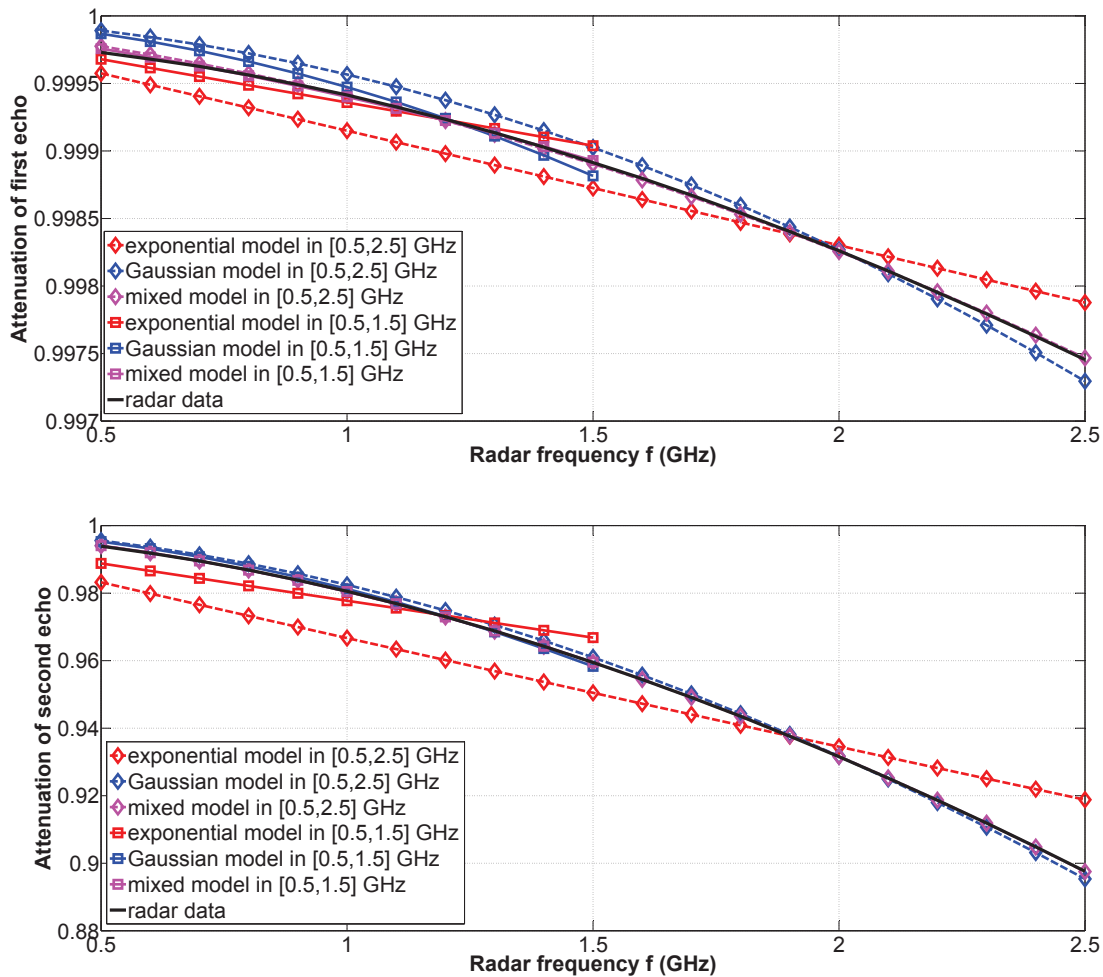


Figure A.3: Case *b*: curve fittings for  $f \in [0.5; 1.5]$  GHz and  $f \in [0.5; 2.5]$  GHz

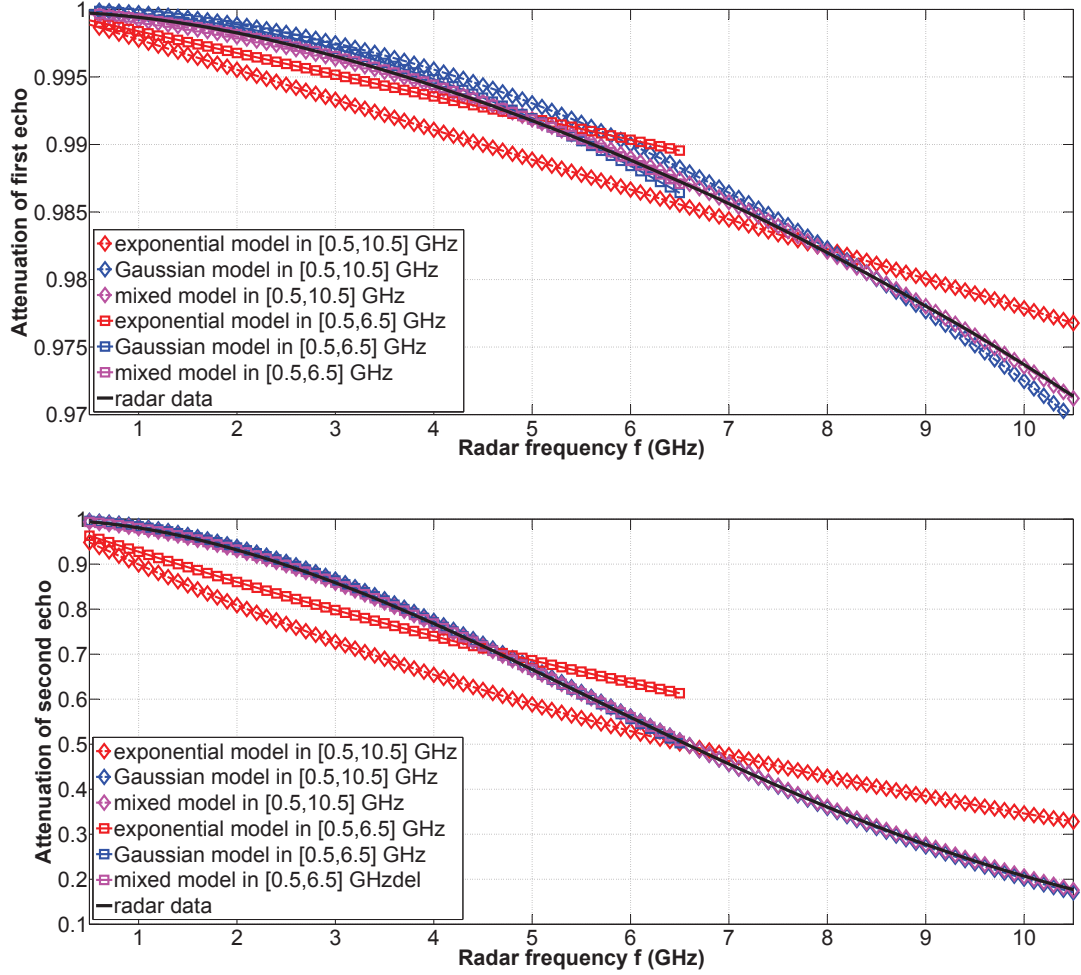


Figure A.4: Case *b*: curve fittings for  $f \in [0.5; 6.5]$  GHz and  $f \in [0.5; 10.5]$  GHz

Table A.2: Curve fittings results for case *b*

RMSE % ( $s_1/s_2$ )	Model	Model		
		$ s(f)  = s_k \times \exp(-bf)$	$ s(f)  = s_k \times \exp(-bf^2)$	$ s(f)  = s_k \times \exp(-bf^2 - cf)$
Frequency				
[0.5; 1.5] GHz		$6.68 \times 10^{-3} / 0.436$	$8.78 \times 10^{-3} / 0.0948$	$1.27 \times 10^{-3} / 7.35 \times 10^{-3}$
[0.5; 2.5] GHz		0.0220/1.16	0.0121/0.153	$1.55 \times 10^{-3} / 7.31 \times 10^{-3}$
[0.5; 6.5] GHz		0.119/5.68	0.0433/0.375	$7.65 \times 10^{-3} / 0.0206$
[0.5; 10.5] GHz		0.262/9.74	0.0918/0.459	0.0149 / 0.0423





# B

## Proof for the Modified MUSIC in chapter 5

In this appendix, we present why a false peak exists for the modified MUSIC in Chapter 5. Only the case of two echoes is presented, but the same calculation can be carried out when the number of echoes is superior to 2. We assume that  $t_1$  and  $t_2$  are the time delays of two echoes ( $t_1 < t_2$ ) and define  $t_3 = (t_1 + t_2)/2$ ,  $\Delta t = (t_2 - t_1)/2$ ,  $\Phi(t) = \hat{\mathbf{A}}^H(t)\mathbf{U}_N\mathbf{U}_N^H\hat{\mathbf{A}}(t)$ . By definition, the rank of  $\mathbf{U}_N\mathbf{U}_N^H$  is  $L - 2$ ; it has always 2 zero eigenvalues with 2 eigenvectors,  $\mathbf{a}^H(t)\mathbf{U}_N\mathbf{U}_N^H\mathbf{a}(t)$  is real valued. Following the subspace principle, we have 2 equalities, as a consequence:

- $\mathbf{a}^H(t)\mathbf{U}_N\mathbf{U}_N^H\mathbf{a}(t) = \mathbf{k}^T\hat{\mathbf{A}}^H(t)\mathbf{U}_N\mathbf{U}_N^H\hat{\mathbf{A}}(t)\mathbf{k} = \mathbf{k}^T\Phi(t)\mathbf{k} = 0$ , for  $t = t_1$  or  $t_2$ .
- $\mathbf{k}^T\Phi(t)\mathbf{k} \neq 0$ , for  $t \neq t_1$  or  $t_2$ .

Then we can have the following 3 situations:

Case 1:  $t = t_1$  and  $t_2$ . When  $t = t_1$  or  $t_2$ ,  $\mathbf{a}^H(t)\mathbf{U}_N\mathbf{U}_N^H\mathbf{a}(t) = \mathbf{k}^T\hat{\mathbf{A}}^H(t)\mathbf{U}_N\mathbf{U}_N^H\hat{\mathbf{A}}(t)\mathbf{k} = \mathbf{k}^T\Phi(t)\mathbf{k} = 0$ .  $\Phi(t)$  has 2 zero eigenvalues with 2 eigenvectors and  $\mathbf{k}$  is a real eigenvector. For  $t = t_1$ , we can see also:

$$\begin{aligned} & \mathbf{k}^T\hat{\mathbf{A}}^H(t_2 - t_1)\hat{\mathbf{A}}^H(t_1)\mathbf{U}_N\mathbf{U}_N^H\hat{\mathbf{A}}(t_1)\hat{\mathbf{A}}(t_2 - t_1)\mathbf{k} \\ & = \mathbf{k}_{10}^H\hat{\mathbf{A}}^H(t_1)\mathbf{U}_N\mathbf{U}_N^H\hat{\mathbf{A}}(t_1)\mathbf{k}_{10} = \mathbf{k}^T\hat{\mathbf{A}}^H(t_2)\mathbf{U}_N\mathbf{U}_N^H\hat{\mathbf{A}}(t_2)\mathbf{k} \end{aligned}$$

where  $\mathbf{k}_{10} = \widehat{\mathbf{A}}(t_2 - t_1)\mathbf{k}$  is another eigenvector. Similarly,  $\mathbf{k}_{20} = \widehat{\mathbf{A}}(t_1 - t_2)\mathbf{k}$  is the second eigenvector for  $t = t_2$ .  $\mathbf{k}_{10}$  and  $\mathbf{k}_{20}$  are complex valued and not collinear with  $\mathbf{k}$ , any non-zero coefficient linear combination of  $\mathbf{k}$  and  $\mathbf{k}_{10}$  or  $\mathbf{k}$  and  $\mathbf{k}_{20}$  is complex valued. Therefore,  $\Phi(t)$  has only one real eigenvector ( $\mathbf{k}$ ) corresponding to one single zero eigenvalue, and  $\Re\{\mathbf{k}^T \Phi(t)\mathbf{k}\} = \mathbf{k}^T \Re\{\Phi(t)\}\mathbf{k} = 0$ , only one solution for  $t_1$  or  $t_2$ . Thus, the number of zero eigenvalues of  $\Re\{\Phi(t_1)\}$  and  $\Re\{\Phi(t_2)\}$  is 1.

Case 2:  $t \neq t_1, t_2$  and  $t_3$ .  $\Phi(t)$  has 2 zero eigenvalues; we can find easily 2 non-linearly correlated eigenvectors  $\mathbf{k}_1$  and  $\mathbf{k}_2$  corresponding to the zero eigenvalues:

$$\begin{aligned}\mathbf{k}_1^H \Phi(t)\mathbf{k}_1 &= \mathbf{k}_1^H \widehat{\mathbf{A}}^H(t) \mathbf{U}_N \mathbf{U}_N^H \widehat{\mathbf{A}}(t)\mathbf{k}_1 = 0 \\ \mathbf{k}_2^H \Phi(t)\mathbf{k}_2 &= \mathbf{k}_2^H \widehat{\mathbf{A}}^H(t) \mathbf{U}_N \mathbf{U}_N^H \widehat{\mathbf{A}}(t)\mathbf{k}_2 = 0\end{aligned}$$

where  $\mathbf{k}_1 = \widehat{\mathbf{A}}(t_1 - t)\mathbf{k}$  and  $\mathbf{k}_2 = \widehat{\mathbf{A}}(t_2 - t)\mathbf{k}$ . Due to  $t \neq t_1, t_2$  and  $t_3$ ,  $\mathbf{k}_1$  and  $\mathbf{k}_2$  are complex and non-linearly correlated. For these values of  $t$ , we can show that any linear combination of  $\mathbf{k}_1$  and  $\mathbf{k}_2$  will always be complex valued.  $\Phi(t)$  has no real eigenvector corresponding to zero eigenvalue. Then,  $\mathbf{k}^T \Phi(t)\mathbf{k} \neq 0$ ,  $\Re\{\mathbf{k}^T \Phi(t)\mathbf{k}\} = \mathbf{k}^T \Re\{\Phi(t)\}\mathbf{k} \neq 0$ , which means that  $\Re\{\Phi(t)\}$  is full rank and that there is no zero eigenvalue.

Case 3:  $t = t_3$ . When  $t = t_1$  and  $t_2$ , we have:

$$\begin{aligned}\mathbf{k}^T \Phi(t_1)\mathbf{k} &= \mathbf{k}^T \widehat{\mathbf{A}}^H(t_1) \mathbf{U}_N \mathbf{U}_N^H \widehat{\mathbf{A}}(t_1)\mathbf{k} = 0 \\ \mathbf{k}^T \Phi(t_2)\mathbf{k} &= \mathbf{k}^T \widehat{\mathbf{A}}^H(t_2) \mathbf{U}_N \mathbf{U}_N^H \widehat{\mathbf{A}}(t_2)\mathbf{k} = 0\end{aligned}$$

which are equivalent to

$$\begin{aligned}\mathbf{U}_N^H \widehat{\mathbf{A}}(t_1)\mathbf{k} &= 0 \\ \mathbf{U}_N^H \widehat{\mathbf{A}}(t_2)\mathbf{k} &= 0\end{aligned}$$

For  $t = t_3$ , any linear combination of above equations leads  $\mathbf{U}_N^H \widehat{\mathbf{A}}(t_1)\mathbf{k} + \alpha \mathbf{U}_N^H \widehat{\mathbf{A}}(t_2)\mathbf{k} = \mathbf{U}_N^H \widehat{\mathbf{A}}(t_3)\{\widehat{\mathbf{A}}^H(\Delta t) + \alpha \widehat{\mathbf{A}}(\Delta t)\}\mathbf{k} = 0$ . Only when  $\alpha$  is equal to 1 or  $-1$ ,  $\widehat{\mathbf{A}}^H(\Delta t) + \alpha \widehat{\mathbf{A}}(\Delta t)$  is a pure real or imaginary matrix.

For  $\alpha = 1$ ,  $\mathbf{U}_N^H \widehat{\mathbf{A}}(t_3)\{\widehat{\mathbf{A}}^H(\Delta t) + \widehat{\mathbf{A}}(\Delta t)\}\mathbf{k} = 2\mathbf{U}_N^H \widehat{\mathbf{A}}(t_3)\Re\{\widehat{\mathbf{A}}(\Delta t)\}\mathbf{k} = 2\mathbf{U}_N^H \widehat{\mathbf{A}}(t_3)\mathbf{k}_3$ .

For  $\alpha = -1$ ,  $\mathbf{U}_N^H \widehat{\mathbf{A}}(t_3)\{\widehat{\mathbf{A}}^H(\Delta t) - \widehat{\mathbf{A}}(\Delta t)\}\mathbf{k} = 2j\mathbf{U}_N^H \widehat{\mathbf{A}}(t_3)\Im\{\widehat{\mathbf{A}}(\Delta t)\}\mathbf{k} = 2j\mathbf{U}_N^H \widehat{\mathbf{A}}(t_3)\mathbf{k}_4$ .

Therefore,  $\mathbf{k}_3^T \Phi(t_3)\mathbf{k}_3 = \mathbf{k}_4^T \Phi(t_3)\mathbf{k}_4 = 0$  with  $\mathbf{k}_3 = \Re\{\widehat{\mathbf{A}}(\Delta t)\}\mathbf{k}$  and  $\mathbf{k}_4 = \Im\{\widehat{\mathbf{A}}(\Delta t)\}\mathbf{k}$ .

In addition,  $\mathbf{a}^H(t) \mathbf{U}_N \mathbf{U}_N^H \mathbf{a}(t)$  is always real valued, thus,  $t_3$  is a solution of  $\lambda_{min}(t) = 0$  and  $\Re\{\Phi(t_3)\}$  has only 2 zero eigenvalues with corresponding eigenvectors  $\mathbf{k}_3$  and  $\mathbf{k}_4$ .

There is a situation when the number of echoes is superior to 2 with  $t_1$ ,  $t_2$  and  $t_3$  the time delays ( $t_1 < t_2$ ) and  $t_3 = (t_1 + t_2)/2$ . Similar to case 1 and case 3, we can prove that  $\Re\{\Phi(t_3)\}$  has 3 zero eigenvalues with corresponding eigenvectors  $\mathbf{k}$ ,  $\mathbf{k}_3$  and  $\mathbf{k}_4$ . When the number of echoes is superior to 2, the number of zero eigenvalues of  $\Re\{\Phi(t)\}$  corresponding to true time delays is odd. For false time delays, this number is even.





## Research and Published Papers

### Journal Papers

1. **M. Sun**, C. Le Bastard, N. Pinel, Y. Wang, J. Li, J. Pan, Z. Wen. Estimation of time delay and interface roughness by GPR using modified MUSIC. *Signal Processing*, doi:10.1016/j.sigpro.2016.05.029.
2. J. Li, C. Le Bastard, Y. Wang, G. Wei, B. Ma, **M. Sun**. Enhanced GPR signal for time-delay estimation in low SNR scenario. *IEEE Geoscience and Remote Sensing Letters* 13:299-303, March 2016.
3. **M. Sun**, C. Le Bastard, N. Pinel, Y. Wang, J. Li. Road surface layers geometric parameters estimation by ground penetrating radar using Estimation of Signal Parameters via Rotational Invariance Techniques method. *IET Radar, Sonar & Navigation* 10:603-609, March 2016.
4. **M. Sun**, C. Le Bastard, Y. Wang, N. Pinel, Time delay estimation using ESPRIT with extended improved spatial smoothing techniques for radar signals. *IEEE Geoscience and Remote Sensing Letters* 13:73-77, January 2016.
5. **M. Sun**, N. Pinel, C. Le Bastard, V. Baltazart, A. Ihamouten, Y. Wang. Time delay and interface roughness estimation by subspace algorithms for pavement survey by radar. *Near Surface Geophysics* 13:279-287, June 2015.

**Conference Papers**

1. J. Li, Y. Wang, **M. Sun**, C. Le Bastard, G. Wei, B. Ma. High-order Cumulant-based MUSIC for Near-field Source Localization. The third Sino-French Workshop on Information and Communication Technologies (SIFWICT 2015), 12 June 2015, Nantes, France.
2. **M. Sun**, Y. Wang, J. Li, C. Le Bastard, N. Pinel. Road parameters estimation By GPR using ESPRIT method. The third Sino-French Workshop on Information and Communication Technologies (SIFWICT 2015), 12 June 2015, Nantes, France.
3. **M. Sun**, C. Le Bastard, N. Pinel, Y. Wang. Estimation of time delay and roughness parameters by GPR using ESPRIT method. International Geoscience and Remote Sensing Symposium/Canadian Symposium on Remote Sensing (IGARSS 2014), 13-18 July 2014, Québec, Canada.
4. **M. Sun**, N. Pinel, C. Le Bastard, V. Baltazart, A. Ihamouten, Y. Wang. Time delay and surface roughness estimation by subspace algorithms for pavement survey by radar. 7th International Workshop on Advanced Ground Penetrating Radar (IWAGPR13), 2-5 July 2013, Nantes, France.



## Résumé étendu (French extended abstract)

### Introduction

L'auscultation mobilise un grand nombre de recherches dans divers domaines (géophysique, géologie, génie civil, militaire, etc). Les besoins peuvent être de nature humanitaire (localisation de mines antipersonnelles par exemple), préventive (détection de canalisations de gaz) ou commerciale (localisation de gisements pétroliers). Dans le domaine du génie civil, les méthodes d'auscultation sont couramment utilisées pour répondre à des besoins de détection, de contrôle, de maintenance des ouvrages en service, et de réception des ouvrages neufs. Les méthodes de contrôle et d'évaluation non destructifs (*C&END*) sont privilégiées pour des raisons de simplicité de mise en oeuvre et de coût réduit. Elles permettent de réaliser de l'imagerie du milieu sans destruction de ce dernier. Parmi ces méthodes (*C&END*), la technique RADAR, et plus particulièrement le radar géophysique ou radar géotechnique appelé aussi "GPR" (pour **Ground Penetrating Radar**) utilise les propriétés de propagation des ondes électromagnétiques (EM) pour déterminer la géométrie, la structure d'un milieu diélectrique. Elle permet ainsi de détecter, localiser, caractériser et identifier des objets ou couches à l'intérieur de ce milieu. Cette technique présente l'avantage d'être à grand rendement et sans contact. A ce jour, de nombreux progrès sont encore attendus avec cette

technologie GPR pour la caractérisation de structures. Les enjeux économiques et environnementaux font du GPR un outil prometteur.

Dans cette thèse, on s'intéresse au développement de méthodes d'auscultation GPR pour déterminer la géométrie, la structure de milieux stratifiés. On se focalise ici plus particulièrement sur l'auscultation des chaussées par GPR. Cette thèse a deux objectifs principaux. Tout d'abord, elle a pour but d'améliorer la compréhension des mécanismes de diffusion à large bande et à très large bande dans un milieu stratifié d'interfaces rugueuses. En effet, avec l'augmentation constante des fréquences d'utilisation de différents systèmes (radars ultra large bande notamment), les interfaces de ces milieux ne peuvent plus être considérées comme planes pour les fréquences les plus élevées. Ainsi, la rugosité des interfaces doit être prise en compte dans la modélisation de la propagation. Une analyse de l'influence de cette rugosité doit alors être réalisée. Ensuite, avec cette approche "large bande" ou "ultra large bande", de nouvelles informations sont contenues dans le signal mesuré. Ainsi, le deuxième objectif de cette thèse est de proposer des méthodes d'estimation conjointe des paramètres de rugosité et d'épaisseur (et donc des estimations des temps de retard et des permittivités). Ainsi, cette thèse propose d'étendre des méthodes à sous-espace à des gammes de fréquences larges bandes et ultra larges bandes afin de pouvoir estimer les différents paramètres du milieu ausculté.

### **Estimation des temps de retard**

Dans cette thèse, on propose premièrement d'estimer les épaisseurs de couches de chaussées par GPR. Pour un milieu non dispersif (à faible perte ou sans perte), milieu étudié dans cette thèse, les épaisseurs des couches dépendent uniquement de deux types de paramètres : la permittivité des couches et les temps de retard provenant des deux interfaces des couches. Pour un milieu dispersif, un paramètre supplémentaire est à prendre en compte : le facteur de qualité (facteur Q) par exemple [25]. Ainsi, l'estimation des temps de retard est un paramètre très important pour l'interprétation des données GPR [10].

Dans cette thèse, on se focalise, comme dans [12], sur l'estimation des épaisseurs des 2 ou 3 premières couches supérieures de la chaussée. Ces couches peuvent avoir des épaisseurs inférieures à 3 cm (comme les BBUM pour Bétons Bitumineux Ultra-Minces de 1 à 2 cm d'épaisseur et les BBTM pour Bétons Bitumineux Très Minces de 2 à 3 cm d'épaisseur). En première approximation, la structure de la chaussée est con-

sidérée comme un milieu stratifié, composé de  $d$  couches homogènes horizontalement et verticalement, et de faible contraste diélectrique. Dans le chapitre 2, on néglige la rugosité des interfaces aux fréquences usuelles (1 à 2 GHz). Ainsi, le milieu est considéré comme un milieu composé d'interfaces lisses. La conductivité pour les deux ou trois couches supérieures de chaussée varie généralement entre  $[10^{-3}; 10^{-2}]$  S/m, selon les données fournies dans [4]. Ainsi, ces milieux sont considérés comme des milieux à faibles pertes, ce qui permet de négliger la dispersivité du milieu [29]. Sous l'hypothèse que les mesures GPR sont effectuées en champ lointain, i.e. les antennes se situent au delà de la limite de Fraunhofer, le modèle de signal reçu se simplifie à un modèle à une dimension et une expression analytique du signal peut être déduite des solutions des équations de Maxwell. En configuration de mesures monostatiques en champ lointain à incidence normale, chaque interface du milieu donne lieu à une onde réfléchi. Si le milieu est à faibles pertes, les différents échos sont simplement des copies retardées de l'impulsion radar  $e(t)$ . Les amplitudes des échos dépendent du contraste diélectrique entre les couches du milieu par l'intermédiaire des coefficients de réflexion de Fresnel [6, 10, 13, 30]. En négligeant les échos multiples (faible contraste diélectrique entre les couches), le signal reçu peut s'écrire sous la forme (2.2). Pour les milieux horizontalement stratifiés non dispersifs, comme les premières couches de chaussée [6], la structure verticale du milieu (l'épaisseur des couches) peut être déduite à partir de la détection des échos et de l'estimation des amplitudes. La détection des échos permet de déterminer les temps de retards alors que l'amplitude des échos permet de déterminer la vitesse des ondes dans chaque couche [6]. L'estimation des temps de retard est généralement réalisée par des méthodes "conventionnelles", comme le filtrage adapté (pour des signaux provenant de GPR impulsif) ou la transformée de Fourier inverse (pour des signaux provenant de radar à sauts de fréquence). Ces méthodes ont l'inconvénient de présenter une limite en résolution. Cette limite en résolution temporelle est donnée par le produit  $B\Delta\tau \geq 1$ , avec  $B$  la bande de fréquences en Hz et  $\Delta\tau$  le retard de propagation entre les deux échos en secondes. Lorsque les échos se chevauchent (cas de mesure des couches de BBTM et BBUM avec un GPR conventionnel de fréquence centrale 1,5 GHz), la détermination des épaisseurs n'est plus possible (par manque de résolution); ainsi, des méthodes haute résolution deviennent nécessaires.

Comme dans [5], on propose dans cette thèse de mettre en oeuvre des méthodes à sous-espace (MUSIC, root-MUSIC, ESPRIT, etc) pour estimer les épaisseurs fines de chaussées. En pratique, les échos rétrodiffusés provenant du GPR sont corrélés (car les signaux sont émis par la même source, l'antenne émettrice du GPR) et les méthodes

HR à sous-espace ne sont pas applicables directement. En effet, pour appliquer ces méthodes dans notre contexte, il faut utiliser des méthodes de prétraitement. Dans ce chapitre, quatre méthodes de prétraitement sont analysées avec les méthodes MUSIC, root-MUSIC et ESPRIT. Ensuite, nous avons proposé d'utiliser deux méthodes de prétraitement avec une méthode à sous-espace linéaire. Contrairement à la littérature, la solution que nous avons proposée n'utilise aucune approximation théorique (section 2.4.1) et améliore donc les résultats dans l'estimation des épaisseurs.

### **Modèle direct : approche électromagnétique des couches de chaussées minces et rugueuses**

Dans le domaine du génie civil, les méthodes utilisées pour estimer les épaisseurs des couches supposent que les interfaces sont lisses (comme présenté dans le chapitre 2). Contrairement à la littérature, dans ce chapitre, la rugosité des interfaces est prise en compte. On propose alors d'analyser les signaux EM avec la prise en compte de la rugosité des interfaces. Le comportement fréquentiel des échos rétrodiffusés dans différentes bandes de fréquences est étudié et analysé (section 3.2). Pour mieux apprécier la mise en œuvre et la robustesse des méthodes haute résolution qui utilisent un modèle de signal a priori sur le terrain, nous avons analysé l'influence de la rugosité des interfaces de chaussée sur les signaux électromagnétiques et introduit un modèle de signal plus réaliste prenant en compte la rugosité. Le but de ces travaux est d'améliorer la compréhension des mécanismes de diffusion à très large bande dans un milieu stratifié d'interfaces rugueuses. Pour réaliser cette analyse, nous avons utilisé la méthode rigoureuse PILE [24, 44]. Cette méthode permet de calculer les échos rétrodiffusés d'un milieu stratifié avec des interfaces rugueuses aléatoires. L'intérêt majeur de la méthode PILE repose sur sa capacité à calculer le champ rétrodiffusé associé à chacun des échos. Cette analyse a montré que la rugosité des interfaces induisait une décroissance fréquentielle continue de l'amplitude des échos (voir section 3.2). Cette décroissance a été modélisée par trois modèles, comme suit :

1. le modèle exponentiel  $|s(f)| = s_k \times \exp(-bf)$  avec  $b$  le paramètre inconnu;
2. le modèle gaussien  $|s(f)| = s_k \times \exp(-bf^2)$  avec  $b$  le paramètre inconnu;
3. le modèle mixte  $|s(f)| = s_k \times \exp(-bf^2 - cf)$  avec  $b$  et  $c$  les paramètres inconnus.

Dans ces modèles,  $s_k$  représente l'amplitude de l'écho pour le cas d'interfaces lisses. Nous avons montré que le modèle exponentiel ne convenait que pour des bandes fréquentielles de largeur inférieure à 2 GHz. De plus, les modèles gaussien et mixte

(après avoir réalisé des ajustements de courbes) sont très proches des données obtenues par la méthode PILE et peuvent être utilisés pour des bandes de fréquences larges.

### **Estimation des paramètres pour le modèle exponentiel**

Suite à ces travaux, nous nous sommes focalisés sur une nouvelle application possible avec le GPR : l'estimation de la rugosité des interfaces de chaussée (en utilisant les travaux du chapitre précédent). Dans ce chapitre, nous proposons d'étendre des méthodes à sous-espace au modèle exponentiel (et donc à des GPR ayant une bande fréquentielle inférieure à 2 GHz) afin d'estimer les différents paramètres du milieu ausculté : temps de propagation, rugosité, permittivité (4.1). Une première modélisation a permis de reformuler le modèle du signal. Ainsi, dans ce chapitre, de nouvelles méthodes de traitement du signal sont proposées pour estimer conjointement les temps de propagation et le nouveau paramètre "rugosité des interfaces". De manière générale, cette étude a pour objectif de proposer des méthodes d'inversion (par estimation) multi-paramètres (rugosité, épaisseur).

Pour estimer conjointement les temps de retard et les paramètres de rugosité, quatre méthodes à sous-espace sont proposées : modified-2-D MUSIC (section 4.2.1), modified root-MUSIC (section 4.2.2), modified MPM (4.2.3) et TDRP-ESPRIT (section 4.2.4). Modified-2-D MUSIC réalise une recherche à deux dimensions pour estimer les temps de retard et le paramètre de rugosité (4.2.1). Afin de réduire la charge de calcul, les méthodes modified root-MUSIC, modified-MPM et TDRP-ESPRIT sont proposées. De plus, des méthodes de prétraitement (moyennage en sous-bandes et des méthodes de réduction du bruit) sont aussi appliquées aux méthodes "modified root-MUSIC" et "TDRP-ESPRIT" afin d'améliorer leurs performances (section 4.1.2). Le comportement des algorithmes proposés est analysé sur des données simulées. Les méthodes proposées montrent de bonnes performances dans l'estimation des paramètres (section 4.4).

### **Estimation des paramètres pour le modèle gaussien et mixte**

Dans le chapitre précédent, l'estimation des temps de retard et des paramètres de rugosité a été réalisée en utilisant un modèle exponentiel. Dans ce cas, les algorithmes à sous-espace peuvent être appliqués assez simplement pour estimer les paramètres du milieu (temps de retard, rugosité et permittivité). Cependant, le modèle exponentiel ne convient que pour des bandes fréquentielles inférieures à 2 GHz. Pour des GPR ayant des bandes fréquentielles supérieures à 2 GHz (Radar à ultra large bande par

exemple), il a été montré dans le chapitre 3 que le comportement en fréquence  $w(f)$  peut être approché par un modèle gaussien ou un modèle mixte (section 3.3). Afin d'estimer les temps de retard et les paramètres de rugosité pour ces deux types de modèles (gaussien et mixte), nous avons tout d'abord proposé deux méthodes multidimensionnelles : le maximum de vraisemblance (section 5.2.1) et l'algorithme Generalized MUSIC (section 5.2.2). Ces deux méthodes estiment les paramètres avec une recherche multidimensionnelle. Ainsi, les charges de calcul de ces deux méthodes sont très grandes. Ensuite, afin de réduire la complexité de calcul, nous avons proposé un algorithme "modified MUSIC" (section 5.3) qui permet de réaliser une recherche monodimensionnelle, c'est-à-dire d'estimer seulement les temps de retards. Cette méthode peut prendre en compte plusieurs modèles fréquentiels (mieux adaptés aux GPR ultra large bande). Dans un second temps, après l'estimation des temps de retard, le comportement fréquentiel des échos rétrodiffusés peut aussi être estimé (section 5.3.3). L'algorithme modified MUSIC a montré de bonnes performances pour l'estimation des temps de retard et des paramètres de rugosité d'interface (section 5.4).

## Expérimentations

Les méthodes proposées dans les chapitres précédents sont testées sur une structure de chaussée composée de deux couches avec des interfaces rugueuses (section 6.1.2). La première couche est un béton bitumineux de 4 cm environ et la deuxième couche une couche de base de 7 cm environ. Pour ces expérimentations, on utilise un radar à sauts de fréquence composé d'un analyseur de réseau vectoriel et de deux antennes ETSA (section 6.1.1). Les algorithmes modified-MUSIC et TDRP-ESPRIT sont testés pour estimer les temps de retard (et donc l'épaisseur) et les rugosités des interfaces de la structure étudiée (section 6.2). Les algorithmes proposés donnent de bonnes performances pour l'estimation des temps de retards. L'estimation de la rugosité de la première interface est acceptable. En revanche, celle de la deuxième interface reste à améliorer (une raison à cette difficulté est le faible contraste diélectrique entre les deux couches qui produit un deuxième écho de très faible amplitude).

## Conclusion et perspectives

Dans le domaine du génie civil, le radar géophysique est largement utilisé comme méthode non-destructive pour ausculter les chaussées (et particulièrement pour estimer les épaisseurs de chaussée). Dans cette thèse, on se focalise sur la prise en compte des rugosités des interfaces. Ainsi, suivant les bandes de fréquences utilisées

par le radar, trois nouveaux modèles de signal sont proposés. Ensuite, des méthodes à sous-espace sont étendues à ces nouveaux modèles. Les résultats de simulation et d'expérimentation montrent globalement de bonnes performances. Enfin, nous pensons que ces travaux de recherche permettront de prendre en compte, très en amont dans le processus de conception d'un produit, la grande diversité des paramètres du milieu observé et facilitera ainsi la mise au point de nouveaux capteurs et de systèmes d'ECND hyperfréquence appropriés et performants pour les applications envisagées. En perspective à ces travaux, d'autres validations expérimentales plus approfondies devraient être réalisées. De plus, les méthodes proposées pourront aussi être étendues aux milieux dispersifs.



## Bibliography

- [1] JOSEF KRAUTKRÄMER AND HERBERT KRAUTKRÄMER. *Ultrasonic testing of materials*. Springer Science & Business Media, 2013. 14
- [2] LABORATOIRE CENTRAL DES PONTS ET CHAUSSÉES, FRANÇA, AND JEAN-FRANÇOIS CORTÉ. *Conception et dimensionnement des structures de chaussée: guide technique*. 1994. 15
- [3] X. DÉROBERT, C. FAUCHARD, P. CÔTE, E. LE BRUSQ, E. GUILLANTON, J. Y. DAUVIGNAC, AND PICHOT. **Step-Frequency Radar Applied on Thin Road Layers**. *Journal of applied geophysics*, **47**:317–325, 2001. 15, 16
- [4] CYRILLE FAUCHARD. *Utilisation de radars tres hautes frequences: application a l'auscultation non destructive des chaussees*. PhD thesis, 2001. 15, 24, 66, 145
- [5] CÉDRIC LE BASTARD. *Apport de techniques de traitement du signal super et haute résolution à l'amélioration des performances du radar-chaussée*. PhD thesis, UNIVERSITE DE NANTES, 2007. 16, 17, 115, 145
- [6] UMBERTO SPAGNOLINI AND VITTORIO RAMPA. **Multitarget detection/tracking for monostatic ground penetrating radar: application to pavement profiling**. *Geoscience and Remote Sensing, IEEE Transactions on*, **37**(1):383–394, 1999. 16, 23, 24, 47, 66, 145
- [7] ANDREA BENEDETTO, FRANCESCO BENEDETTO, MARIA ROSARIA DE BLASII, AND GAETANO GIUNTA. **Reliability of signal processing technique for pavement damages detection and classification using ground penetrating radar**. *Sensors Journal, IEEE*, **5**(3):471–480, 2005. 16, 47
- [8] IL AL-QADI AND S LAHOUAR. **Measuring layer thicknesses with GPR—Theory to practice**. *Construction and building materials*, **19**(10):763–772, 2005. 16, 78, 116
- [9] SAMER LAHOUAR AND IMAD L AL-QADI. **Automatic detection of multiple pavement layers from GPR data**. *NDT & E International*, **41**(2):69–81, 2008. 16

- [10] UMBERTO SPAGNOLINI. **Permittivity measurements of multilayered media with monostatic pulse radar.** *Geoscience and Remote Sensing, IEEE Transactions on*, **35**(2):454–463, 1997. [16](#), [23](#), [24](#), [66](#), [144](#), [145](#)
- [11] TIMO SAARENKETO AND TOM SCULLION. **Road evaluation with ground penetrating radar.** *Journal of applied geophysics*, **43**(2):119–138, 2000. [16](#)
- [12] CÉDRIC LE BASTARD, VINCENT BALTAZART, YIDE WANG, AND JOSEPH SAILLARD. **Thin-pavement thickness estimation using GPR with high-resolution and superresolution methods.** *Geoscience and Remote Sensing, IEEE Transactions on*, **45**(8):2511–2519, 2007. [16](#), [18](#), [19](#), [24](#), [34](#), [40](#), [66](#), [144](#)
- [13] R WU, X LI, AND J LI. **Continuous pavement profiling with ground-penetrating radar.** In *Radar, Sonar and Navigation, IEE Proceedings-*, **149**, pages 183–193. IET, 2002. [16](#), [24](#), [66](#), [145](#)
- [14] IGNACIO SANTAMARIA, CARLOS PANTALEON, AND JESUS IBANEZ. **A comparative study of high-accuracy frequency estimation methods.** *Mechanical Systems and Signal Processing*, **14**(5):819–834, 2000. [16](#), [26](#)
- [15] NICOLAS PINEL, CÉDRIC LE BASTARD, VINCENT BALTAZART, CHRISTOPHE BOURLIER, AND YIDE WANG. **Influence of layer roughness for road survey by ground penetrating radar at nadir: theoretical study.** *Radar, Sonar & Navigation, IET*, **5**(6):650–656, 2011. [18](#), [19](#), [21](#), [34](#), [47](#), [48](#), [51](#), [52](#), [53](#), [65](#), [66](#), [79](#)
- [16] J VAN DER KRUK, N DIAMANTI, A GIANNOPOULOS, AND H VEREECKEN. **Inversion of dispersive GPR pulse propagation in waveguides with heterogeneities and rough and dipping interfaces.** *Journal of applied Geophysics*, **81**:88–96, 2012. [18](#), [65](#)
- [17] ANTONIOS GIANNOPOULOS AND NECTARIA DIAMANTI. **Numerical modelling of ground-penetrating radar response from rough subsurface interfaces.** *Near Surface Geophysics*, **6**(6):357–369, 2008. [18](#), [19](#)
- [18] FRANÇOIS JONARD, LUTZ WEIHERMÜLLER, HARRY VEREECKEN, AND SÉBASTIEN LAMBOT. **Accounting for soil surface roughness in the inversion of ultrawideband off-ground GPR signal for soil moisture retrieval.** *Geophysics*, **77**(1):H1–H7, 2012. [18](#), [19](#)
- [19] SANG-EUN PARK, WOOL M MOON, AND DUK-JIN KIM. **Estimation of surface roughness parameter in intertidal mudflat using airborne polarimetric SAR data.** *Geoscience and Remote Sensing, IEEE Transactions on*, **47**(4):1022–1031, 2009. [18](#)

- [20] FRANCESCO MATTIA, THUY LE TOAN, JEAN-CLAUDE SOUYRIS, GIACOMO DE CAROLIS, NICOLAS FLOURY, FRANCO POSA, AND GUIDO PASQUARIELLO. **The effect of surface roughness on multifrequency polarimetric SAR data.** *Geoscience and Remote Sensing, IEEE Transactions on*, **35**(4):954–966, 1997. [18](#)
- [21] XAVIER BLAES AND PIERRE DEFOURNY. **Characterizing bidimensional roughness of agricultural soil surfaces for SAR modeling.** *Geoscience and Remote Sensing, IEEE Transactions on*, **46**(12):4050–4061, 2008. [18](#)
- [22] Y. OGAWA A. MOGHADDAR AND E.K. WALTON. **Estimating the Time-Delay and Frequency Decay Parameter of Scattering Component Using a Modified MUSIC Algorithm.** *IEEE Transactions on Antennas and Propagation*, **42**(10):1412–1418, 1994. [19](#), [70](#), [72](#)
- [23] LELE QU, QIANG SUN, TIANHONG YANG, LILI ZHANG, AND YANPENG SUN. **Time-Delay Estimation for Ground Penetrating Radar Using ESPRIT With Improved Spatial Smoothing Technique.** *Geoscience and Remote Sensing Letters, IEEE*, **11**(8):1315–1319, 2014. [19](#), [24](#), [29](#), [30](#), [31](#), [34](#), [39](#), [66](#)
- [24] CHRISTOPHE BOURLIER, CÉDRIC LE BASTARD, AND VINCENT BALTAZART. **Generalization of PILE method to the EM scattering from stratified subsurface with rough interlayers: Application to the detection of debondings within pavement structure.** *Geoscience and Remote Sensing, IEEE Transactions on*, **53**(7):4104–4115, 2015. [19](#), [21](#), [48](#), [146](#)
- [25] KHALED CHAHINE. *Méthodes d'estimation paramétriques appliquées à la caractérisation de milieux dispersifs du génie civil.* PhD thesis, 2010. [23](#), [144](#)
- [26] PAVEL PROTIVA, JAN MRKVICA, AND JAN MACHÁČ. **Estimation of wall parameters from time-delay-only through-wall radar measurements.** *Antennas and Propagation, IEEE Transactions on*, **59**(11):4268–4278, 2011. [23](#)
- [27] SYLVIE MARCOS AND JAVIER SANCHEZ-ARAUJO. **Méthodes linéaires haute résolution pour l'estimation de directions d'arrivée de sources. performances asymptotiques et complexité.** *Traitement du signal*, **14**(2):99–116, 1997. [24](#), [32](#), [33](#)
- [28] PETRE STOICA, TORSTEN SÖDERSTRÖM, AND VIRGINIJA ŠIMONYT. **On estimating the noise power in array processing.** *Signal Processing*, **26**(2):205–220, 1992. [24](#), [32](#)
- [29] DAVID J DANIELS. *Ground penetrating radar, 1st edition.* Iet, 2004. [24](#), [52](#), [66](#), [145](#)

- [30] JIAN LI AND RENBIAO WU. **An efficient algorithm for time delay estimation.** *Signal Processing, IEEE Transactions on*, **46**(8):2231–2235, 1998. [24](#), [66](#), [145](#)
- [31] CÉDRIC LE BASTARD, YIDE WANG, VINCENT BALTAZART, AND XAVIER DEROBERT. **Time delay and permittivity estimation by ground-penetrating radar with support vector regression.** *Geoscience and Remote Sensing Letters, IEEE*, **11**(4):873–877, 2014. [24](#)
- [32] HIROYOSHI YAMADA, MANABU OHMIYA, YASUTAKA OGAWA, AND KIYOHICO ITOH. **Superresolution techniques for time-domain measurements with a network analyzer.** *Antennas and Propagation, IEEE Transactions on*, **39**(2):177–183, 1991. [24](#), [29](#), [30](#), [34](#), [68](#)
- [33] WEIXIU DU AND RODNEY LYNN KIRLIN. **Improved spatial smoothing techniques for DOA estimation of coherent signals.** *Signal Processing, IEEE Transactions on*, **39**(5):1208–1210, 1991. [29](#), [31](#)
- [34] RALPH O SCHMIDT. **Multiple emitter location and signal parameter estimation.** *Antennas and Propagation, IEEE Transactions on*, **34**(3):276–280, 1986. [34](#)
- [35] ARTHUR J BARABELL. **Improving the resolution performance of eigenstructure-based direction-finding algorithms.** In *Acoustics, Speech, and Signal Processing, IEEE International Conference on ICASSP'83.*, **8**, pages 336–339. IEEE, 1983. [34](#)
- [36] RICHARD ROY AND THOMAS KAILATH. **ESPRIT-estimation of signal parameters via rotational invariance techniques.** *Acoustics, Speech and Signal Processing, IEEE Transactions on*, **37**(7):984–995, 1989. [34](#), [75](#)
- [37] ALFRED M BRUCKSTEIN, TIE-JUN SHAN, AND THOMAS KAILATH. **The resolution of overlapping echos.** *Acoustics, Speech and Signal Processing, IEEE Transactions on*, **33**(6):1357–1367, 1985. [34](#)
- [38] CÉDRIC LE BASTARD, VINCENT BALTAZART, AND YIDE WANG. **Modified ESPRIT (M-ESPRIT) algorithm for time delay estimation in both any noise and any radar pulse context by a GPR radar.** *Signal Processing*, **90**(1):173–179, 2010. [34](#), [36](#), [75](#), [76](#)
- [39] MENG SUN, CÉDRIC LE BASTARD, YIDE WANG, AND NICOLAS PINEL. **Time-Delay Estimation Using ESPRIT With Extended Improved Spatial Smoothing Techniques for Radar Signals.** *Geoscience and Remote Sensing Letters, IEEE*, **13**:73–77, 2016. [34](#), [97](#)

- [40] PETRE STOICA AND RANDOLPH L MOSES. *Introduction to spectral analysis, 1st edition*. Prentice hall Upper Saddle River, 1997. 34
- [41] NECTARIA DIAMANTI AND DAVID REDMAN. **Field observations and numerical models of GPR response from vertical pavement cracks**. *Journal of Applied Geophysics*, **81**:106–116, 2012. 47
- [42] SÉBASTIEN LAMBOT, MICHAËL ANTOINE, MARNIK VANCLOOSTER, AND EVERT C SLOB. **Effect of soil roughness on the inversion of off-ground monostatic GPR signal for noninvasive quantification of soil properties**. *Water Resources Research*, **42**(3), 2006. 47
- [43] UĞUR OĞUZ AND LEVENT GÜREL. **Frequency responses of ground-penetrating radars operating over highly lossy grounds**. *Geoscience and Remote Sensing, IEEE Transactions on*, **40**(6):1385–1394, 2002. 47
- [44] NICOLAS DÉCHAMPS, NICOLE DE BEAUCOUDREY, CHRISTOPHE BOURLIER, AND SERGE TOUTAIN. **Fast numerical method for electromagnetic scattering by rough layered interfaces: Propagation-inside-layer expansion method**. *JOSA A*, **23**(2):359–369, 2006. 48, 49, 50, 66, 79, 146
- [45] F LIU. *Modelisation et experimentation radar impulsional et a sauts de frequence pour l'auscultation de milieux stratifies du genie civil*. PhD thesis, UNIVERSITE DE NANTES, 2007. 49, 115
- [46] NICOLAS PINEL, CÉDRIC LE BASTARD, CHRISTOPHE BOURLIER, AND MENG SUN. **Asymptotic modeling of coherent scattering from random rough layers: Application to road survey by GPR at nadir**. *International Journal of Antennas and Propagation*, **2012**, 2012. 51, 52, 53, 61
- [47] MENG SUN, NICOLAS PINEL, CÉDRIC LE BASTARD, VINCENT BALTAZART, AMINE IHAMOUTEN, AND YIDE WANG. **Time delay and interface roughness estimations by GPR for pavement survey**. *Near Surface Geophysics*, **13**(3):279–287, 2015. 52, 66, 67
- [48] ERIC I THORSOS AND DARRELL R JACKSON. **Studies of scattering theory using numerical methods**. *Waves in Random Media*, **1**(3):S165–S190, 1991. 52
- [49] CHRISTOPHE BOURLIER, GILDAS KUBICKÉ, AND NICOLAS DÉCHAMPS. **Fast method to compute scattering by a buried object under a randomly rough surface: PILE combined with FB-SA**. *JOSA A*, **25**(4):891–902, 2008. 66

- [50] RENBIAO WU, JIAN LI, AND ZHENG-SHE LIU. **Super resolution time delay estimation via MODE-WRELAX.** *Aerospace and Electronic Systems, IEEE Transactions on*, **35**(1):294–307, 1999. 66
- [51] Y HUA AND TK SARKAR. **Matrix pencil method and its performance.** In *Acoustics, Speech, and Signal Processing, 1988. ICASSP-88., 1988 International Conference on*, pages 2476–2479. IEEE, 1988. 72
- [52] YINGBO HUA AND TAPAN K SARKAR. **Matrix pencil method for estimating parameters of exponentially damped/undamped sinusoids in noise.** *Acoustics, Speech and Signal Processing, IEEE Transactions on*, **38**(5):814–824, 1990. 73, 74
- [53] YINGBO HUA AND TAPAN K SARKAR. **On SVD for estimating generalized eigenvalues of singular matrix pencil in noise.** In *Circuits and Systems, 1991., IEEE International Symposium on*, pages 2780–2783. IEEE, 1991. 73
- [54] TAPAN K SARKAR AND ODILON PEREIRA. **Using the matrix pencil method to estimate the parameters of a sum of complex exponentials.** *Antennas and Propagation Magazine, IEEE*, **37**(1):48–55, 1995. 74
- [55] MICHAEL ZOLTOWSKI AND FRED HABER. **A vector space approach to direction finding in a coherent multipath environment.** *Antennas and Propagation, IEEE Transactions on*, **34**(9):1069–1079, 1986. 94, 95
- [56] BENJAMIN FRIEDLANDER AND ANTHONY J WEISS. **Direction finding using spatial smoothing with interpolated arrays.** *Aerospace and Electronic Systems, IEEE Transactions on*, **28**(2):574–587, 1992. 98
- [57] ANTHONY J WEISS AND BENJAMIN FRIEDLANDER. **Performance analysis of spatial smoothing with interpolated arrays.** *Signal Processing, IEEE Transactions on*, **41**(5):1881–1892, 1993. 98
- [58] MENG SUN, CÉDRIC LE BASTARD, NICOLAS PINEL, YIDE WANG, AND JIANZHONG LI. **Road surface layers geometric parameters estimation by ground penetrating radar using Estimation of Signal Parameters via Rotational Invariance Techniques method.** *IET Radar, Sonar & Navigation*, **10**:603–609, 2016. 99
- [59] FENG-XIANG GE, DONGXU SHEN, YINGNING PENG, AND VICTOR OK LI. **Super-resolution time delay estimation in multipath environments.** *Circuits and Systems I: Regular Papers, IEEE Transactions on*, **54**(9):1977–1986, 2007. 100

- [60] FENGXIANG GE, QUN WAN, XIUTAN WANG, AND YINGNING PENG. **Frequency estimation of the sinusoidal signals with unknown lowpass envelopes based on the eigenanalysis.** In *Radar Conference, 2002. Proceedings of the IEEE*, pages 453–458. IEEE, 2002. 100
- [61] FIFAME KOUDOGBO, PAUL FRANCOIS COMBES, AND HENRI-JOSE MAMETSA. **Numerical and experimental validations of IEM for bistatic scattering from natural and manmade rough surfaces.** *Progress In Electromagnetics Research*, **46**:203–244, 2004. 103
- [62] ERIC S LI AND KAMAL SARABANDI. **Low grazing incidence millimeter-wave scattering models and measurements for various road surfaces.** *Antennas and Propagation, IEEE Transactions on*, **47**(5):851–861, 1999. 103





# Thèse de Doctorat

Meng SUN

Techniques avancées de traitement du signal pour applications GPR en tenant compte des rugosités d'interfaces des milieux stratifiés

Advanced signal processing techniques for GPR by taking into account the interface roughness of a stratified medium

## Résumé

Dans cette thèse, on s'intéresse au développement de nouvelles méthodes d'auscultation GPR pour déterminer la géométrie et la structure des chaussées. Cette thèse a deux objectifs principaux. Tout d'abord, elle a pour but d'améliorer la compréhension des mécanismes de diffusion à très large bande dans un milieu stratifié composé d'interfaces rugueuses. Avec l'augmentation des fréquences d'utilisation de différents systèmes, les interfaces de chaussée ne peuvent plus être considérées comme planes. Ainsi, la rugosité des interfaces doit être prise en compte dans la modélisation de la propagation. Donc, une analyse de l'influence de cette rugosité sur l'onde rétrodiffusée a été réalisée. Elle a permis de montrer que la rugosité induit une décroissance en fréquence de l'amplitude des échos. Cette décroissance a ensuite été introduite dans le modèle du signal.

Dans un second temps, plusieurs méthodes de traitement de signal ont été proposées pour estimer conjointement les paramètres de rugosité et d'épaisseur. D'abord, des méthodes multidimensionnelles ont été proposées en prenant en compte l'influence de la rugosité. Ensuite, afin de réduire la charge de calcul, des méthodes monodimensionnelles ont été proposées. Ces méthodes ont été évaluées à partir de signaux simulés. Les résultats ont montré de bonnes performances pour l'estimation des temps de retard et des paramètres de rugosité des interfaces.

Enfin, les méthodes de traitement proposées dans ce manuscrit ont été testées sur des données expérimentales, qui permettent de valider les résultats théoriques et de montrer la faisabilité de la mesure de couches minces de chaussée et du paramètre de rugosité.

## Mots clés

Radar géophysique, estimation de retard, rugosité de interface, l'épaisseur

## Abstract

In this thesis, we focus on the development of new GPR methods to estimate the pavement structure. This thesis has two main objectives. First, it aims to improve the understanding of the scattering mechanisms for large-band radars in a stratified medium composed of rough interfaces. With increasing frequencies, pavement interfaces can no longer be considered as flat. The interface roughness must be taken into account in the propagation modelling. Thus, the influence of the roughness has been analysed. It has been shown that the interface roughness provides a continuous frequency decay of the magnitude of the echoes. This continuous frequency decay has then been introduced into the signal model. Secondly, several signal processing methods have been proposed to jointly estimate the roughness and thickness of pavement. Thus, multidimensional methods have been proposed by taking into account the roughness. Then, in order to reduce the computational burden, one-dimensional methods have also been proposed. From simulations, it can be seen that the proposed algorithms provide a good performance in parameter estimations (time delay, permittivity, roughness and thickness). Finally, the proposed signal processing methods are tested on experimental data. The results confirm the theoretical prediction. They show the feasibility to estimate both the thickness of thin pavements and roughness parameter.

## Key Words

Ground Penetrating Radar (GPR), Time Delay Estimation (TDE), interface roughness, thickness